Coronal and Transition Region Observations of the Sun and Cool Stars.

A thesis submitted for the degree of
Doctor of Philosophy

by

David Ronan Williams, B.Sc. (Q.U.B. 1998)

Faculty of Science

Department of Pure and Applied Physics
The Queen's University of Belfast
Belfast, Northern Ireland

22nd February 2002

"I love this place at night. The stars …
there's no right or wrong in them.
They're just there."

– Sgt. Elias*, Platoon*.

For Mum, Dad, Christina and Anna.
(And Ben)

Acknowledgements

Firstly, I would like to thank my supervisors, the Three Wise Men. Firstly, Professor Francis Keenan deserves sincere thanks for his support (both professional and financial), loyalty, advice, humour, organisational skills . . . and even science. Secondly, Professor Ken Phillips, at Rutherford Appleton Laboratory, whose knowledge of Solar Physics has been of enormous help in the work presented in this thesis. He has been a good guide in his capacities as both co-supervisor and collaborator, and his bible *Guide to the Sun* is indispensable. Thirdly, but in particular, I would like to my immediate supervisor, Dr. Mihalis Mathioudakis, who took me on as his first Ph.D. student despite the fact that he should have known better. Until the very end, he has suffered the whole experience with a degree of patience normally attributed to saints. He has also done a remarkable job of keeping my work in the right direction. His attitude to research and his understanding of physics in this area have been invaluable. And then there's the Fourth Man, Dr Peter Gallagher, a good friend and collaborator – his infectious enthusiasm for solar physics, and his scientific and career advice have been a source of encouragement throughout my graduate studies. Any future I have in astronomy is due, in no small part, to each of these men.

Rutherford Appleton Labs and DENI/DHFETE/DEL both deserve thanks, too, for financial support, without which my studies – let alone a field trip to Zambia – would not have been possible. Thanks, too, to both Dr Thanassis Katsiyannis and Dr Robert Ryans for putting up with stupid UNIX questions, fixing things I broke, and giving me the best machines and monitors that equipment grant money could buy. It's a thankless job, and they both did it well.

With the possible exception of the last few days, life in the APS Division has been a very enjoyable one for the last three-and-a-half years. Postdocs and fellow research students and have been and gone, but Hilary Magee and Dave Pinfield deserve a particular mention, because it's all their fault. If they hadn't come out to the Common Room with us undergraduates and persuaded me that I was right in considering an astronomy Ph.D., none of this would ever have happened. I rest my case.

At the end of the day, though, the APS is nothing without the Common Room Experience, and the following people all deserve thanks for good company, foul language, abundant craic, bad taste and general banter on random nights of the week (but especially Fridays): Nicolas (Arguments), Dave (Drinking), Peter (Brute Ignorance and Good Slags), Jonathan (Wisdom and Deadpan), Martin (Hyperactive Good Nature), Hilary and Edel (Moral Support), Thanassis (Greek 'History'), Sophia (Abundant Good Cheer and Concerts), Darko (Sneakiness and Poker), Carrie (Social Life and Sympathy), Shaun (Smartest Person Ever), Simon (Co-observer & Encyclopaedia Collander-Brownica), Cathy (my Independent Salsa Woman), Colin (Feminine Side), Gerry (Bad Influence) and last but never least, Fergal (Rugby, Sofa and generally being a top mate).

Thanks, too, to the Common Room staff, who've put up with the dregs of astronomy and made the CR a second living room – in particular Paddy, John and Cathy.

For reminding me that the real world still exists – and making life in it the more enjoyable – I owe a lot of my sanity to Paddy, Niall, Eoin (wherever he may be), Martin, and showbiz Neil. Every one a star. Plus thanks to Claire, Jillian, Ciaran, Seán and Ed for being good housemates to a moody student. *Diolch yn fawr.*

Honorable mentions need to go to Mark and James, who've been good mates of mine over the last few years. You couldn't ask to share an office with two more likeable people. From being my first-year lab partner through to being at the desk next-door, Mark has always kept my spirits up when things weren't going well. Likewise, James has helped me remain sane, understand physics, and has put up with a lot more stupid questions than he ever asked while he's shared my office. Holidays and field trips, like the eclipse expedition to Zambia, were all the better for his company. It's been great fun working, drinking and generally just hanging around with both of these guys. You'll be missed, lads.

But most of all, thanks to my family, who've got me through everything during my time at university. I can't ever do their support and encouragment justice, but this thesis is dedicated to them in partial repayment. Thanks, Mum & Dad, more than I can say.

Abstract

This thesis presents observations of dynamic events in the outer atmosphere of the Sun and other cool stars. The effect of opacity on ratios of strong transition region lines is investigated for the flare dMe star YZ CMi, and the RS CVn binary Capella. Opacity is shown to be both an important effect in these stars' atmospheres and an important diagnostic tool for scale distances. Also presented are observations of a class C5.2 flare on the Sun. The flare's energy release is shown to be largely in the form of mass motions of ejected plasma, and is compared to the energy of particles injected into the lower atmosphere.

The largest part of the thesis deals with the investigation of short-period oscillations in the solar corona. Theoretical considerations suggest that short period MHD waves make a significant contribution to coronal heating. We have identified a strong 6 sec oscillations in an active region coronal loop. We use near-simultaneous *SoHO* observations to determine the physical parameters of the loop. The oscillation is associated with a fast-mode wave travelling with a velocity of 2000 km s^{-1}. Although the wave travels a distance greater than $\lambda/4\pi$ and therefore meets a necessary criterion for slow dissipation, the dissipation length is well in excess of the loop length. The temporal evolution of the intensity is in agreement with the model of an impulsively generated, fast-mode wave.

Contents

List of Tables

List of Figures

Publications

A list of publications resulting from work presented in this thesis is given below.

Refereed Publications

1. D. R. Williams, M. Mathioudakis, P. T. Gallagher, K. J. H. Phillips, R. T. J. M^{c}Ateer, F. P. Keenan, A. C. Katsiyannis:
   Observations and assessment of a fast-mode wave in the solar corona
   Monthly Notices of the Royal Astronomical Society, *in press*, (2002).

2. D. R. Williams, K. J. H. Phillips, Rudawy P., M. Mathioudakis, P. T. Gallagher, E. O'Shea, F. P. Keenan, P. Read, B. Rompolt:
   High Frequency Oscillations in a Solar Active Region Coronal Loop.
   Monthly Notices of the Royal Astronomical Society, **326**, 428 (2001).

3. P. T. Gallagher, D. R. Williams, K. J. H. Phillips, M. Mathioudakis, R. N. Smartt, F. P. Keenan :
   Multi-Wavelength Observations of the 1998 September 27 Flare Spray
   Solar Physics, **195**, 367 (2000).

4. M. Mathioudakis, J. M^{c}Kenny, F. P. Keenan, D. R. Williams, K. J. H. Phillips:
   The effects of opacity in the transition region of YZ CMi
   Astronomy and Astrophysics, **351**, L23 (1999).

Non-refereed Publications

1. D. R. Williams, M. Mathioudakis, J. M^{c}Kenny, and F. P. Keenan:
   Opacity Effects in the Transition Region of Active Stars
   Astronomical Society of the Pacific Conference Series, vol. **223**, CD-889, (2001).

Chapter 1

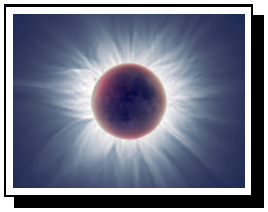

Introduction

1.1 Background

It is rare in Astronomy that the object of a thesis author's research is immediately familiar to every person on Earth. Knowledge of the existence of the solar corona (*"The bit you see during an eclipse"*) is less common, and familiarity with the 'coronal heating problem', less still – the latter is limited almost exclusively to students and researchers (both professional and amateur) in astronomy.

To a fair approximation, this thesis is concerned with the counter-intuitive Sun. By this, the author means the region of the solar atmosphere where the kinetic temperature ascends monotonically with *increasing* distance from the source of the Sun's nuclear power. The solar corona extends out to $\sim 10\ R_{\odot}$, although this is somewhat difficult to quantify since it becomes ever more tenuous as it reaches out into interplanetary space, from which it is eventually indistinguishable. It also spans a temperature range of 10^6 – $\sim 4 \times 10^6$ K, which is remarkable considering that the visible photosphere of the Sun has a black-body temperature of only 5600 K. The discovery of the anomalous high-temperature corona was made in a laboratory on Earth. Lines of a phantom element, christened *coronium*, were discovered in 1869, in the spectrum of the Sun during a total solar eclipse – when the yellow photosphere and red chromosphere are occulted by the Moon's disc. After 60 years of investigation, however, the prominent emission lines at 5303 Å and 6374 Å were shown by Edlén (1942) to be due to two, highly ionised species of iron: Fe XIV and Fe X, respectively, revealing that the corona must in fact be substantially hotter than the surface of the Sun. So began the investigation into the *coronal heating problem*.

1.2 The solar magnetic field

The solar magnetic field brings a remarkable degree of structure to the surface and atmosphere of our star, on both small and large scales. This structure dictates the con-

ditions for the complex activity we see, such as solar flares and coronal mass ejections, the less energetic activity and formation in quiescent regions, and the transport of energy. It is therefore worth dwelling on nature of the solar magnetic field.

1.2.1 Sub-surface interactions and emergence

Magnetic field lines are an invaluable concept in discussing the interaction of a field with the plasma in which it is embedded. In a high-conductivity (*i.e.* highly ionised) plasma, field lines are effectively frozen into the surrounding ionised gas by the Lorentz force. This field is initially assumed to be a simple dipole (*poloidal* field) at the start of each sunspot cycle. Parker's (1966) solar dynamo model proposes that plasma-tied bundles of meridian-parallel field lines (magnetic flux tubes) are pared off from the underlying field at the base of the convection zone, brought upward by convective motions, and twisted by interaction of the convective cells with the Coriolis force. This gives the field a radial component (Figure 1.1). He also showed that due to pressure equilibrium between the magnetic flux tube (which includes both gas pressure and magnetic pressure, $p_B = \frac{B^2}{2\mu}$, with $\mu = 4\pi$) and the surrounding atmosphere (gas pressure only), the density of such a flux bundle is reduced with respect to its surroundings. The flux tube therefore naturally rises to the surface under its own buoyancy (Parker 1975).

In addition, meridional flows – large-scale flows from the poles to the solar equator (Choudhuri, Schussler & Dikpati 1995) – are thought to play a vital role in the distortion of the solar magnetic field. The interaction of meridional flows with the convective motions in the region below the photosphere drives the inverse dependence of the rotation rate with increased solar latitude – the solar equator has a rotation period of 25 days, as against the polar regions' 27 days. As a consequence of this *differential rotation*, the sub-surface field lines are continually wound around the solar rotation axis, over the eleven-year sunspot cycle, increasing the magnetic field strength and thereby the buoyancy of the flux tubes. The leading pole of each emerging dipole field is al-

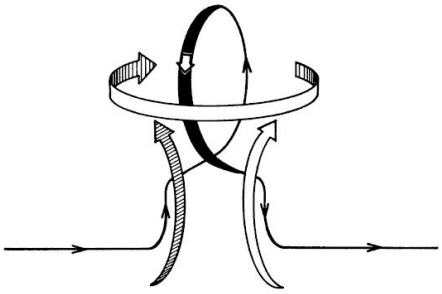

Figure 1.1: Cyclonic twisting of field lines convection zone, caused by convective motions interacting with the Coriolis force. From Parker (1970).

ways the same polarity in the northern hemisphere, too, as well as closer to the equator (Hale *et al.* 1919), with the leading poles in the southern hemisphere being of opposite polarity (*i.e.* positive leaders in the northern hemisphere means negative leaders in the southern hemisphere). Eventually, after sunspot maximum, the sub-surface field becomes so stressed that it reconfigures itself to a poloidal field once more, but of the opposite polarity, and the cycle starts again.

Since 1998, observations with the *Transition Region And Coronal Explorer* (*TRACE*) spacecraft have shown that magnetic structures in the corona are composed of very fine ($\sim$100 km diameter) threads (Schrijver *et al.* 1999). Spruit and Roberts (1983) describe sub-photospheric flux tubes as bundles of magnetic threads, and this picture appears to extend, then, into the corona. Loops are no longer seen to be the apparently homogeneous, cylindrical structures found in earlier observations by the *Solar and Heliospheric Observatory* (EUV, UV and visible), Yohkoh (X-rays) and their predecessor missions.

At the upper limit of the convection zone, convection cells are visible in the photosphere as *granular* elements of upward-flowing gas at their centre, with dark lanes of cooler down-flow delineating these cells. At the photospheric level, the magnetic field strength is of the order of $\sim$1000 G (0.1 tesla), but is visibly structured with wide variations in field strength (Lin & Rimmele 1999) of 200 – 1000 G. The variations in field are most likely due to the horizontal dragging of field lines to the down-flowing boundaries. These boundaries therefore exhibit concentrations of magnetic flux, visible in the photosphere and overlying chromosphere as the quiet Sun *network*. At network

junctions, where these lanes converge, the field bundles are either oppositely-directed, in which case they cancel magnetically (to a first approximation), or have the same radial field vector, in which case they combine to form strong field points, visible in optical and ultraviolet bands as *network bright points* (*e.g.* M^{c}Ateer *et al.* 2002). Likewise, as new cells are born and die, these bright points can drift together and mutually reinforce or annihilate (Schrijver *et al.* 1997).

1.2.2 Active regions

The distinction between regions of small-scale magnetic structure, and large-scale structure in the atmosphere is the distinction between the *quiet Sun* and *active regions*. While coronal structures can be seen with satellite observations in the quiet Sun (*e.g.* Handy & Schrijver 2000), active regions are much larger, more complex arrangements of the magnetic field (Aschwanden *et al.* 1999b), extending out to $> 10^5$ km from the surface of the Sun. Large flux-tubes again rise under buoyancy, but locally depress the photosphere much more than the network fields. These dark depressions are the sunspots. The flux tube's diameter is greater at the top of the atmosphere than further down, and so the bound plasma expands with the field lines as it rises, cooling adiabatically. These dark spots form either alone or in groups and are normally at the core of active regions. The cyclonic braiding of the magnetic threads means that the flux tube extends for hundreds of arcseconds ($1'' \equiv 725$ km) around the main sunspot penumbra. In the photosphere and chromosphere, this appears as an enhanced network around the supergranular cells, whereas in the transition region and corona, the familiar entangled magnetic loops are seen.

These complex aggregations of closed magnetic loops are almost exclusively the site of flares, events where the magnetic field is re-organised, and vast amounts of energy released across the electromagnetic spectrum. Flares frequently eject large amounts of material through the outer corona into interstellar space. As *TRACE* ob-

servations have shown (Figure 1.2; Aschwanden 2001) these loops can be seen at all heights: from their apexes (well into the million-degree corona) down to their footpoints in the chromosphere and photosphere (5×10^3 K). Since *TRACE* observations are all made in narrow emission line passbands, this implies that these loops radiate in a given emission line along their entire length, and so are effectively isothermal. Additionally, since these loops can be seen in the emission of ions with widely varying peak formation temperatures, then magnetic threads with different temperatures must co-exist in close proximity. The isothermality can be understood in terms of high thermal conductivity, which is often the case in a highly ionised plasma, but the degree of inhomogeneity between threads is perhaps surprising.

1.3 Cool stars

As a G2V-type main sequence star, the Sun is categorised as a *cool star*. This category encompasses a broad range of stellar temperatures, from spectral type F ($T = 7400$ K), through the cooler G and K, to M ($T = 2400$ K). For this reason, such stars are often classified as *late-type*. A characteristic of cool stars is that they have a detectable chromosphere and corona, with a solar-like transition region at their interface. Recently, though, there has been evidence that late A-type stars also exhibit spectral signatures of a transition region and chromosphere (Simon & Landsman 1997).

Chromospheric activity is the term normally given to the presence (or degree) of emission in any or all of the Hα, Ca II H & K and Mg II *h* & *k* lines. Indeed, the flux of the Ca II K line shows a good correlation with the eleven-year solar activity cycle. Because these lines are particularly strong in the solar spectrum, opacity at the centre of each line is particularly high. Different parts of each line profile are thus associated with different heights in the chromosphere: photons with wavelengths in the wings of a strong line are less likely to be absorbed or resonantly scattered, and so can escape from lower in the atmosphere than photons in the corresponding line core. These lines

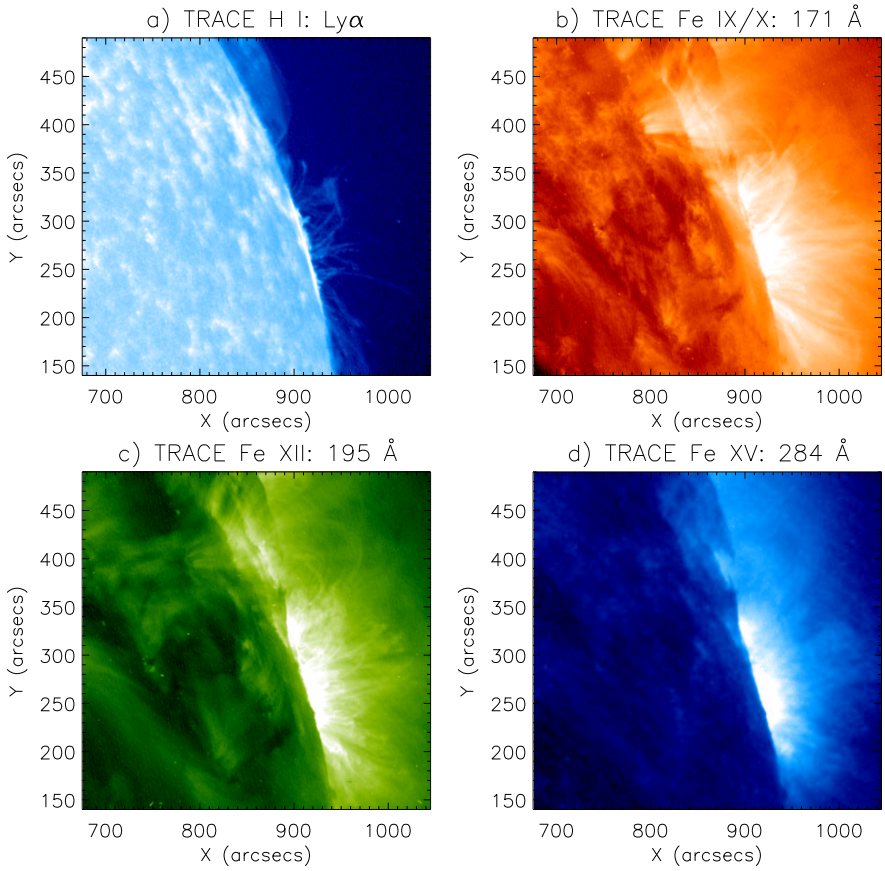

Figure 1.2: Four images of an active region in the corona, with absolute heliographic co-ordinates, taken on 1999 August 11 (day of the total solar eclipse) at ∼09:45 U.T.: a) the upper chromosphere in Lyα; b) upper transition region (Fe IX $= 6.3 \times 10^5$ K) and lower corona (Fe X $= 10^6$ K); c) mid corona in Fe XII at 1.3×10^6 K; d) upper corona in Fe XII at 2.0×10^6 K. Note: I) concentrations of diffuse transition region moss in b), which correspond closely in position to the positions of the bright chromospheric network in a); II the cospatiality of the loops at different temperatures, particularly those in b) and c); and III) the prominence at the top of this field of view, bright in the chromospheric line of Lyα, but entirely in absorption in coronal emission lines.

are in absorption (albeit with often complex, non-Gaussian profiles) in the Sun, but in many, highly active late-type stars, the lines are wholly in emission. Mathioudakis *et al.* (1995) explored the already-suspected link (Wilson 1966) between the rate of stellar rotation and strong coronal emission. Theoretical work (*e.g.* Kleeorin, Rogachevskii & Ruzmaikin 1995) also supports the idea that the magnetic field strength is linked to rotation rates.

A major challenge in solar and stellar astrophysics is that we do not at the moment have a realistic model for the complex, heterogeneous Sun, let alone a model extensible

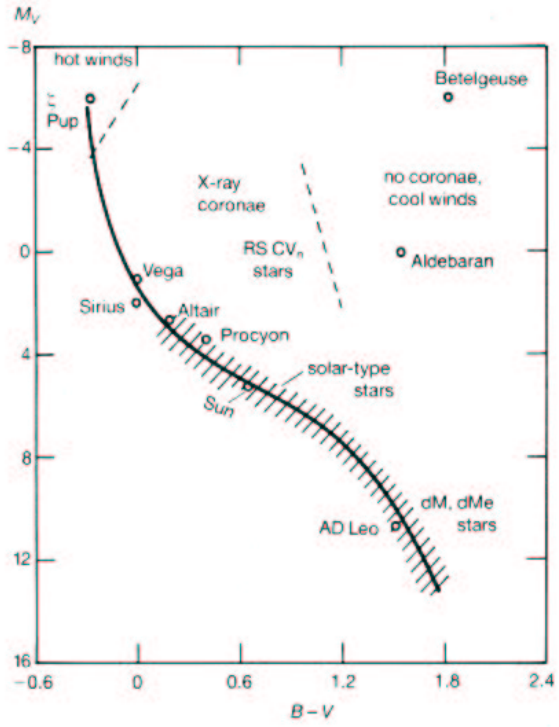

Figure 1.3: Hertzsprung-Russell (colour-magnitude) diagram indicating the positions occupied by main sequence, cool stars. From Phillips (1992).

to all cool stars. Furthermore, whilst a good deal of the physics of cool stars can be deduced from their spectra, the largest problem in analysing their behaviour is that they are spatially unresolved point sources. Nevertheless, since the Sun is a fairly typical cool star (Figure 1.3), we infer much of the structure of other cool stars from what we deduce about our own (frequently in terms of differences between solar parameters and those we see elsewhere).

1.3.1 The solar atmosphere

By the equation of hydrostatic equilibrium,

$$\frac{dP(r)}{dr} = -\frac{GM_\odot}{r^2}\rho(r) \tag{1.1}$$

the kinetic pressure $P(r)$ decreases with increasing distance r from the centre of the Sun, as gravitational potential $-\frac{GM(r)}{r^2}$ increases, where $\rho(r)$ is the mass density at

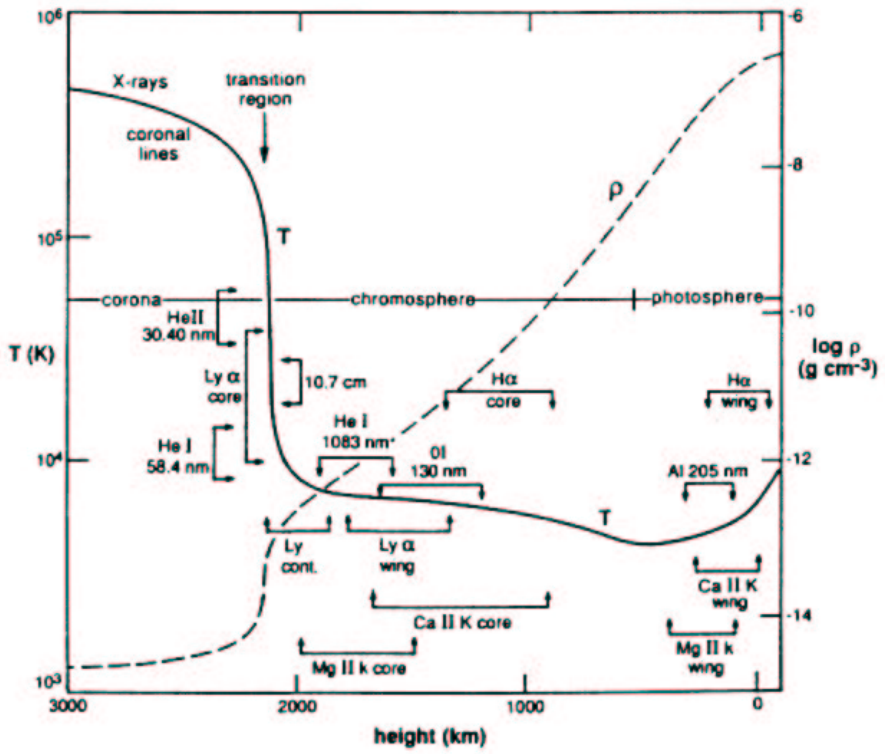

Figure 1.4: The semi-empirical solar atmosphere model of Vernazza, Avrett & Loeser (1981). Regions (in height) of the formation of prominent spectral lines are indicated. Figure taken from Avrett & Loeser (1992).

height r. It is also known, from observational evidence, that the temperature of the Sun decreases above the surface, until it reaches the *temperature minimum*. The temperature then increases from this level upward. Vernazza, Avrett & Loeser (1981) constructed a semi-empirical temperature and density model of the Sun from the photosphere to the corona, based on observations of emission and absorption from lines formed at different temperatures. Their model, known as the VAL model, is shown schematically in Figure 1.4. This figure graphically demonstrates the surprising nature of the solar radial temperature gradient. Since the Sun is a gaseous body, the 0 km level (bottom-right) follows a solar physics convention, and is equivalent to the depth in the photosphere at which $1/e$ of all photons emitted at $\lambda 5000$ Å are absorbed in the line of sight. In order that calculations for the model be tractable, however, the simplifying assumption of a uniform Sun was made. The model does not treat either active regions or magnetically 'open' coronal holes.

The outer solar atmosphere is described here in terms of its three levels: the chromosphere, the transition region, and the corona.

1.3.2 The chromosphere

The chromosphere is effectively the highest part of the atmosphere of which it is possible to make observations in visible light. The prominent lines of H I, Ca II and Mg I & II in the spectrum are the most commonly used in analysing this region of the atmosphere. The temperature span of the chromosphere is appreciable, but sufficiently small that these emission lines can be formed over a large range of heights (Figure 1.4). Emission in the wings of Hα, near the temperature minimum, reveals highly dynamic motions in all directions. Prominent upward overshoots from convection were also discovered, however, in the blue-shifted Hα emission at the centre of *supergranules* (the chromospheric *internetwork*), as were corresponding down-draughts at the cell boundaries (the network).

Network bright points have briefly been discussed (§1.2.1), but another aspect of these field concentrations are the *spicules* seen protruding from the chromosphere in limb observations. Doppler-shift measurements on the solar disc show these to be upward jets of material, with velocities of the order of 10 km s^{-1}, overlying the photospheric and chromospheric network. The *plages*, found around active regions, are enhancements of emission corresponding to higher magnetic field concentrations. Suspended in twisted magnetic field tubes above the chromosphere, *prominences* are channels of elevated material which absorb strongly in the dominant spectral lines, and are thus seen in Hα as dark *filaments* against the underlying solar disc. They, too, are associated with active regions, but can extend much further than the enhanced network. The first indication of a heating problem is in fact in the chromosphere, where the temperature gradient first reverses. Clues to this are provided in the emission of the upper chromosphere from the Lyα line of H I, as well as from He I: both lines are excited by higher

energy electrons than those found at temperatures at the photosphere/chromosphere interface.

1.3.3 The transition region

The structure of the transition region is appreciably different from that of the more historically familiar chromosphere. It is also less a horizontal layer than it is a highly inhomogeneous and irregular interface region between the chromosphere and the corona (Peter 2001). Until spectrographic images were obtainable from above Earth's atmosphere, little was known about this region of the solar atmosphere. Its temperature range of 10^4 – 10^6 K means that the majority of its emission is in the UV and EUV. Table 1.1 lists the most prominent lines visible in the transition region.

Structure around active regions is visibly dominated by the enhanced magnetic network (Figure 1.5); where the density is sufficiently high, loops can also be seen. At the base of active region loops, diffuse *moss* has also recently been detected, and is thought to be enhanced UV emission caused by thermal conduction from the million-degree corona (Fletcher & de Pontieu 1999). Dynamic events in the transition region are dominated by solar flares and nanoflares, and by the so-called network blinkers which are transient brightenings in the EUV. Additionally, overshoots of upward motions in the convective cells leads to the generation of waves in the photosphere, which can propagate into the chromosphere and transition region, leading to further non-thermal motions and inhomogeneity. Whereas emission from the chromosphere must be carefully treated – in that strong lines exhibit absorption at their core – emission in the transition region is a much simpler affair and is largely treated as being *optically thin*.

Opacity is therefore much lower in the transition region than in the chromosphere, and the radiation field can no longer be considered isotropic. Because of the low level of emission compared to the photosphere, and even chromosphere, the radiation field is dominated by photospheric light, and so the radiation temperature (5600 K) is vastly

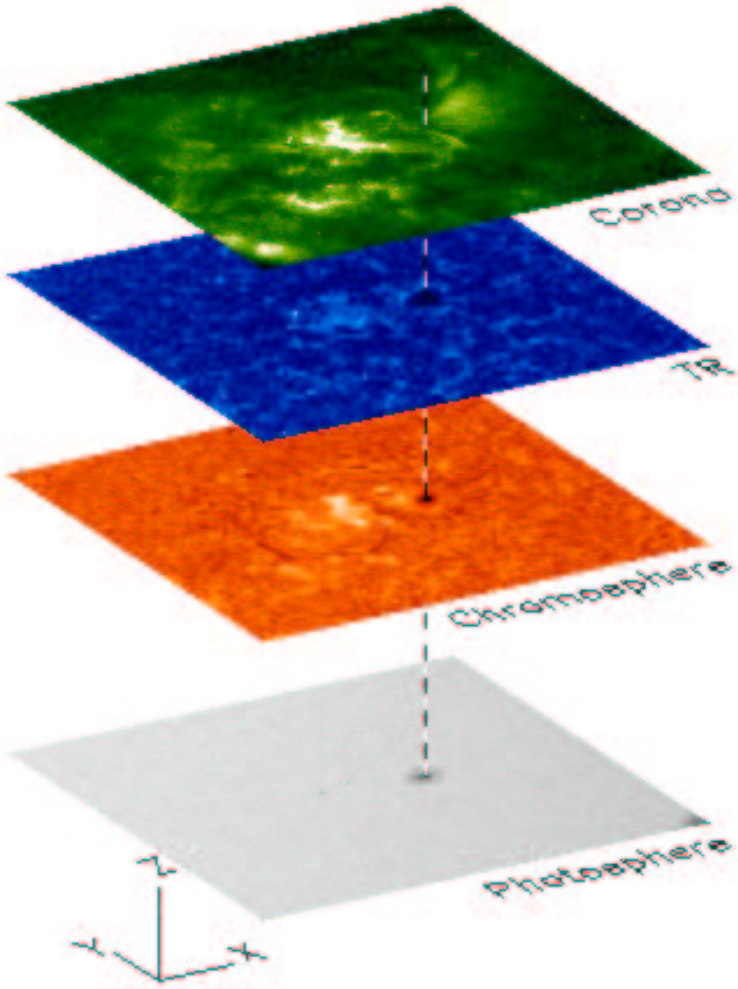

Figure 1.5: Stacked plot of four levels in the solar atmosphere, not to scale. All observations were made on 2000 August 24 at around the same time. From bottom to top: I) continuum photosphere around an active region taken by *TRACE*; II) chromosphere in Hα showing sunspot and surrounding plages (bright) and filament/prominence (curved dark channel), taken at Big Bear Solar Observatory; III) *TRACE* transition region image in λ1600 Å (continuum UV), showing remnants of the chromosphere's magnetic network structure (bright lanes); IV) the corona taken in Fe IX/X λ173 Å, showing the dominant loop structures associated with the strong active region magnetic field.

different than the local kinetic temperature ($\sim 10^5$ K).

1.3.4 The corona

In terms of volume, the corona makes up by far the largest part of the solar atmosphere.

It is also the region of highest temperature, as already discussed, and of lowest density.

Table 1.1: Prominent lines in the transition region spectrum, in decreasing order of intensity. After Mariska (1992). Only lines with intensity greater than 100 erg.cm^{-2}.s^{-1}.sr^{-1} have been included.

Species	Wavelength (Å)	log T_{max} (K)	Intensity (erg.cm^{-2}.s^{-1}.sr^{-1})
C III	977.0	4.8	963
Si III	1206.5	4.6	695
C III	1335.7	4.4	396
O V	629.7	5.4	335
C III	1175.7	4.8	315
C II	1334.5	4.4	309
O VI	1031.9	5.5	305
C IV	1548.2	5.0	207
O VI	1037.6	5.5	204
N V	1238.8	5.3	148
Si IV	1393.8	4.8	127

Emission from the corona is made of several parts:

- *F corona* – (for *Fraunhofer*); photospheric continuum light scattered by dust grains with low velocity, and features the Fraunhofer absorption lines visible in the photospheric spectrum
- *K corona* – (for *Kontinuum*); photospheric continuum light scattered by free electrons with much higher thermal velocities (because of the much lower electron mass), which smear the Fraunhofer lines so widely (in wavelength space) that they are no longer seen
- Emission line corona – line emission from atoms which have become very highly ionised (*e.g.* Fe XXII) by collisions with very high energy electrons. Although material is predominantly concentrated around magnetic field lines by the Lorentz force, density enhancements in active region loops and associated solar flares mean that these regions, in particular, dominate the line emission from the Sun

The plasma β parameter expresses the ratio of the local kinetic pressure in a magnetised

plasma, such as the corona, to the magnetic pressure:

$$\beta = \frac{p_{\text{kinetic}}}{p_{\text{magnetic}}} = \sum_i \frac{N_i k T_i}{\left(\frac{B^2}{8\pi}\right)} \tag{1.2}$$

where k is Boltzmann's constant and p_{kinetic} is the sum of partial pressures due to all species i. In practice, the majority of the pressure is due to electrons since hydrogen forms the largest part of the atmosphere, and collisions quickly equate the kinetic temperatures of all particles; therefore $p_{\text{kinetic}} \approx N_e k T_e$. In the photosphere, β is greater than one, and gas pressure in fact dominates. In the chromosphere, the structure is largely ordered by the magnetic field, and β is less than unity. In the transition region and (especially) the corona, however, the extremely tenuous plasma has a very low kinetic pressure, and the magnetic field dominates all structure, with $\beta \ll 1$. As a result of this, although the majority of emission is in the EUV and X-ray régimes, there is also a good deal of radio emission from the corona due to spiralling charged particles emitting gyrosynchrotron photons at gigahertz frequencies.

Large-scale structure in the corona can be broken down into three categories. Active regions and the quiet Sun have already been described. Coronal holes, lastly, are regions of open field lines which extend into interplanetary space. Whilst these high-temperature, low density regions are always present at the poles of the Sun, they are sometimes found extending to equatorial latitudes. Because particles tied to these field lines are not bound to the lower corona, coronal holes are known to be the source of the high-speed solar wind – an escape of high-energy charged particles into space.

A clue to the heating mechanism of the corona is the spatial correlation between high-temperature plasma and active regions. Even non-flaring coronal active regions exhibit emission from extremely highly-stripped ions such as Ca XV and Fe XV, with detectable lines in the visible spectrum. This relationship between the magnetic field and the observed high temperature plasma will shortly be discussed (§1.4.3).

1.4 Energy transport in the transition region and corona

In the upper chromosphere, transition region and corona of the Sun, the temperature gradient is the reverse of what one would normally expect, so that convection is not an issue. Energy transport is therefore by conduction, radiation, bulk motions and a fourth mechanism, discussed in due course: wave motion.

1.4.1 Radiation transport

The basic equation describing radiative transport of energy is the equation of radiative transfer:

$$\frac{\mathrm{d}I_\lambda}{\mathrm{d}x} = -k_\lambda \rho I_\lambda + j_\lambda \rho \tag{1.3}$$

which relates the change in specific intensity I_λ, with distance x along the line of sight, at a certain wavelength to the atomic processes involved. k is a catch-all *mass absorption* parameter for removal of photons from the beam, by both scattering (denoted by σ_λ) and absorption (κ_λ). The first term on the right-hand side includes both of these simply by $k_\lambda = \sigma_\lambda + \kappa_\lambda$, with each term expressed per unit mass. The second term is the amount of energy introduced into the beam, and expresses the emissivity j_λ per unit mass. The source function S_λ relates the emission and absorption coefficients of the plasma by

$$S_\lambda = \frac{j_\lambda}{k_\lambda}. \tag{1.4}$$

These parameters must be determined for each individual line, using calculations of the rates of various atomic processes. In any given emission line, two energy levels are involved, denoted 1 (lower level) and 2 (upper level). If we assume that the region of the atmosphere that we examine is in a steady state – temperature, and density remain constant for each ion species and electrons – then we can assume statistical equilibrium. In other words, all processes responsible for exciting an electron to level 2 are balanced,

over a given time interval, by all the processes responsible for de-exciting an electron to level 1.

Excitation of electrons in ions can be achieved by absorption of a photon (Einstein coefficient B_{12}) of the correct energy or collisions with other particles (collision rate C_{12}), predominantly free electrons in a highly ionised plasma. De-excitation can likewise be achieved by collisions (C_{21}) or photon emission, the latter being either spontaneous (A_{21}) or induced (B_{21}). An approximation used in the corona, and often applied to the transition region, is that the emission is *optically thin – i.e.* to a good approximation, all photons created by radiative de-excitation escape the solar atmosphere without being lost through absorption or scattering back down to the photosphere. We can show this by considering the atomic processes involved.

An important consideration in the low-density corona is that the radiation field I_λ is vastly reduced, and no longer isotropic as it is in the inner layers of the Sun. We therefore neglect the process of radiative excitation (B_{12}). The rate of excitation R_{12} is therefore dominated by collisions with electrons. In a plasma where the electrons follow a Maxwellian velocity distribution, the collision rate C_{12} will depend on the velocity distribution with energy $f(E)$ as well as the effective cross-section for collisions σ, also a function of E. Conservation of energy demands that for an electron to excite an ion from state 1 to state 2, it must have energy greater than or equal to the difference in energy between these states, E_{12}. Therefore

$$C_{12} = \int_{E_{12}}^{\infty} \sigma(E)\, f(E)\, dE. \tag{1.5}$$

and hence C_{12} takes the form

$$C_{12} = \frac{8.65 \times 10^{-6}}{g_1 \sqrt{T}} \Omega_{12}(T) \exp\left(\frac{-E_{12}}{kT}\right) \tag{1.6}$$

where g_1 is the degeneracy of level 1, and Ω_{12} is the effective collision strength for the

transition. Ω_{12} is in turn related to the spontaneous radiative decay probability A_{21} by

$$\Omega_{12} = \frac{8\pi}{\sqrt{3}} \frac{I_H}{\Delta E_{12}} g \omega_1 f_{12} \tag{1.7}$$

where I_H is the ionisation energy of hydrogen (13.6 eV), and g is an effective Gaunt factor. Likewise, the collision strength for the reverse process will be given by

$$C_{21} = \frac{8.65 \times 10^{-6}}{g_2 \sqrt{T}} \Omega_{12}(T). \tag{1.8}$$

Given these transition probabilities, it remains to determine the transition rates, R. R_{12} will be proportional to the number of ions with electrons in level 1 (or ions in the 'lower state' of excitation) per unit volume N_1, as well as the number of electrons per unit volume N_e, so the excitation rate is given by $R_{12} = N_e N_1 C_{12}$. The statistical equilibrium in the corona can therefore be written as

$$N_e N_1 C_{12} = N_2 A_{21} + N_e N_2 C_{21} \tag{1.9}$$

i.e. collisional excitation is balanced by spontaneous emission and collisional de-excitation.

1.4.2 Emission line diagnostics

1.4.2.1 Line ratios

For a plasma to be optically thin, the collisional de-excitation rate must be negligible compared with the radiative decay rate, *i.e.* $N_2 A_{21} \gg N_e N_2 C_{21}$. Cancelling the N_2 term in Equation 1.9 gives a critical density, N_c for which these de-excitation rates are equal.

$$N_c = \frac{A_{21}}{C_{21}} = 1.16 \times 10^5 g_2 \sqrt{T} \left(\frac{A_{21}}{\Omega_{21}} \right) \tag{1.10}$$

So where $N_e \ll N_c$, we can assume that the atmosphere is indeed optically thin. For lines with small oscillator strengths, this is true in both the transition region and corona, but for lines where the oscillator strength (*i.e.* spontaneous transition probability) is great, the line becomes optically thick. This is the rationale behind emission line ratio diagnostics in solar and stellar atmospheres, illustrated if we consider a three-level situation in a given ion. Where both lines are optically thin,

$$\frac{I_{12}}{I_{13}} = \frac{\lambda_{13}}{\lambda_{12}} \frac{\Omega_{12}}{\Omega_{13}} \exp\left(\frac{E_{13} - E_{12}}{kT}\right) \tag{1.11}$$

so that the ratio of the lines is a function of only one variable, temperature. Alternatively, if one upper level (3) is still predominantly de-populated by collisions, then

$$\frac{I_{12}}{I_{13}} = \frac{\lambda_{13}}{\lambda_{12}} \frac{8.65 \times 10^{-6} \Omega_{12}}{A_{31} g_3 \sqrt{T}} \exp\left(\frac{E_{13} - E_{12}}{kT}\right) N_e. \tag{1.12}$$

Where $E_{12} \rightarrow E_{13}$, this ratio becomes much more sensitive to N_e than T. These ratios are extensively used to derive local conditions for plasmas in observations of the Sun (Chapter 6), and of average values for stellar atmospheres (Chapter 3).

Whilst it is generally true that the transition region is lumped in with the corona as being optically thin, there are certain cases, such as Equation 1.12, where this is not valid. Chapter 3 contains a discussion of a very important effect of opacity in this thin region of stellar atmospheres.

1.4.2.2 The emission measure

It follows from statistical equilibrium (Equation 1.9) that at distance r, the flux of a given optically thin line, from a volume of atmosphere V, per unit area and into unit solid angle, is given by

$$F_{21} = \frac{hc}{\lambda_{12}} \frac{1}{4\pi r^2} \int_V n_e n_1 C_{12} \, dV \tag{1.13}$$

$$= \frac{hc}{\lambda_{12}} \frac{1}{4\pi r^2} 8.63 \times 10^{-6} \frac{\Omega_{12}}{g_1} 0.8 \frac{n_{el}}{n_H} \int_V n_e^2 \frac{n_{ion}}{n_{el}\sqrt{T}} \exp\left(\frac{-hc}{\lambda_{12} kT}\right) dV$$

where $n_H/n_e = 0.8$, $n_{\rm el}/n_H$ is the abundance of the element with respect to hydrogen, $n_{\rm ion}/n_{\rm el}$ is the fraction of the element in a given ionisation stage, and all variables are kept within the integral over volume. In practice, all these variables are temperature-dependent terms which can be grouped together as the *contribution function*, $G(T)$, by

$$G(T) = \frac{n_{\rm ion}}{n_{\rm el}} T^{-\frac{1}{2}} \exp\left(\frac{-hc}{\lambda kT}\right) \tag{1.14}$$

which will be the same for any two lines emitted from the same ion at the same temperature. For a given ion, the dependence of F_{21} on the precise line emitted is therefore contained only in the terms before the integral in Equation 1.13. Furthermore, G(T) can be assumed to have an average value of 0.7 times its peak value $G(T_{\rm max})$ in a temperature range ΔT (Pottasch 1963), *i.e.*

$$\overline{G(T)}\,\Delta T = 0.7\, G(T_{\rm max})\,\Delta T = \int_{\Delta T} G(T)\, dT \tag{1.15}$$

. F_{21} can now be rewritten as

$$F_{21} = \frac{hc}{4\pi\lambda R^2} \frac{8.63 \times 10^{-6} \Omega_{12}}{g_1} 0.8 \frac{N_{\rm el}}{N_H} \overline{G(T)} \int_V n_e^2\, dV. \tag{1.16}$$

The quantity $\int_V n_e^2\, dV$ is known as the emission measure (EM), and is a gauge of how much emitting material is contained in a given volume V; substituting $dV = \frac{1}{2} 4\pi R^2 dh$ for the visible hemisphere of a shell over height dh, one can rewrite the emission measure as $\int_R N_e^2\, dh = \int N_e^2 \frac{dh}{dT}\, dT = \int N_e^2 \frac{dh}{d\log T}\, d\log T$. The integrand in the second or third of these integrals (either form is acceptable) is referred to as the *differential* emission measure, DEM(T). The most important point is that, given the flux of a certain emission line, and assuming a certain temperature, the fluxes of all other emission lines at that temperature can be deduced. More common, though, is the construction of an emission measure distribution (*cf.* Dere & Mason 1993; Raymond & Doyle 1981)

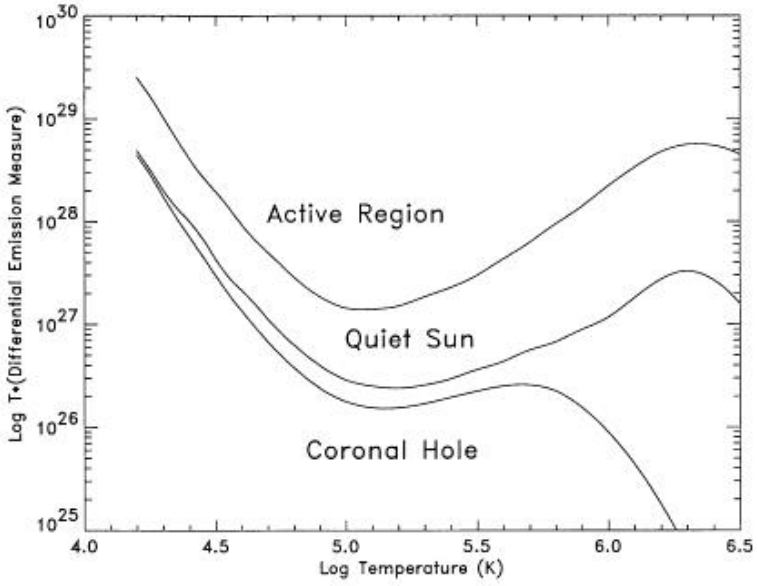

Figure 1.6: Differential emission measures for the solar corona, taken from Dere & Mason (1993).

which describes the amount of material as a function of temperature. By using lines of ions formed over a range of temperatures, a DEM curve can be constructed, such as those in Figure 1.6.

1.4.3 Transport of wave energy

Since thermodynamics forbids the upper chromosphere, transition region and corona from being heated by radiative energy transport, other explanations are proposed. An umbrella for the theories of heating in these regions of the solar atmosphere is that of *wave heating*. The vast array of forces in a magnetically influenced plasma means that different wave modes contribute in different ways according to the local conditions (see review by Stein & Leibacher (1974)). The principal restoring forces in these wave modes are gravity/buoyancy, pressure and magnetic tension, and interact under the umbrella term of *magneto-acoustic-gravity* (MAG) waves.

1.4.3.1 Gravity waves

Gravity waves operate in a density-stratified atmosphere with a negative radial density gradient, and are the effect of an interaction between buoyancy and gravity. Although gravity waves can operate at low frequencies in the highly stratified lower, chromosphere, they are not important in the upper atmosphere since they are non-propagating (evanescent) above the Brunt-Väisälä cut-off frequency

$$N_{\mathrm{BV}} = \frac{c_s\sqrt{\gamma-1}}{\gamma H} \tag{1.17}$$

where c_s is the local sound speed, and $H = \frac{p_0}{\rho_0 g}$ is the height over which the local pressure p_0, in a plasma of mass density ρ_0 and local gravity g, decreases by factor $1/e$ (the zero subscripts represent unperturbed values, since acoustic waves necessarily modulate these parameters); H is known as the *pressure scale height*. In the lower chromosphere $N_{\mathrm{BV}} \sim 5$ mHz (Lou 1995). Only waves of very low frequency – *i.e.* those excited by long-timescale perturbations – can propagate as far as the transition region and lower corona, where they are eventually dissipated.

1.4.3.2 Acoustic waves

Acoustic waves are longitudinal, and therefore detectable on the solar disc as Doppler-shifted (low frequency) or Doppler-broadened emission. Like gravity waves, they too have a frequency 'cut-off', but this is now a lower limit to propagating frequencies:

$$\omega_a = \frac{c_s}{2H}. \tag{1.18}$$

In a plasma with adiabatic index $\gamma = \frac{5}{3}$, this acoustic cut-off is $1.02 \times N_{\mathrm{BV}}$. The p-mode internal solar oscillations with periods of 3 and 5 minutes (ν = 5.6 and 3.3 mHz) are particularly dominant in the acoustic mode frequency spectrum of both internetwork and network areas. Because of the density stratification of the lower chromosphere,

however, acoustic waves are normally reflected downward and cannot propagate to the upper chromosphere where the heating problem begins.

1.4.3.3 Magnetohydrodynamic waves

Magnetohydrodynamic (MHD) waves (sometimes *hydromagnetic* waves), are a broad family of wave modes incorporating acoustic waves, purely magnetic *Alfvén* waves, and both *fast* and *slow magnetoacoustic* (or *magnetosonic*) waves. There are five basic equations of MHD. The first is the induction equation

$$\frac{\partial \mathbf{B}}{\partial t} = \nabla \times (\mathbf{v} \times \mathbf{B}) + \eta \nabla^2 \mathbf{B} \tag{1.19}$$

where $\eta = \frac{1}{\mu\sigma}$, and σ is the electrical conductivity of the plasma, which is very high in the corona. The right hand side of Equation 1.19 is made up of the advection term (first) and diffusion term (second). Where the plasma velocity $v \to 0$, the diffusion term dominates, but is very slow, and the timescales τ for diffusion of field lines over large distances L are long (Phillips 2000):

$$\tau = \frac{L^2}{\eta}, \tag{1.20}$$

helping to explain the long lives of sunspots and active regions. The remaining four equations are of the forms:

$$\frac{D\rho}{Dt} + \rho \nabla \cdot \mathbf{v} = 0 \tag{1.21}$$

$$\rho \frac{D\mathbf{v}}{Dt} = -\nabla p + (\nabla \times \mathbf{B}) \times \frac{\mathbf{B}}{\mu} - \rho g \hat{\mathbf{z}} \tag{1.22}$$

$$\frac{D}{Dt}\left(\frac{p}{\rho^\gamma}\right) = 0 \tag{1.23}$$

$$\nabla \cdot \mathbf{B} = 0 \tag{1.24}$$

where the operator $\frac{D}{Dt} \equiv \frac{\partial}{\partial t} + \mathbf{v} \cdot \nabla$ is the *material, convective* or *full* derivative, used to express these equations in a plasma with velocity $\mathbf{v}$. Respectively, these express

the continuity of mass, momentum and energy in a gas, and the absence of magnetic monopoles.

Alfvén waves propagate in three ways (Priest 1982): by magnetic tension $\mathcal{T}_B = \frac{B_0^2}{\mu}$, where propagation is entirely parallel to the magnetic field, by magnetic pressure p_B (§1.2.1), in which case they are *compressional* Alfvén waves and may propagate in any direction; or they may be torsional Alfvén waves, which are a propagating azimuthal twist in a flux tube. Pure and torsional Alfvén waves do not cause either pressure or density variations. All Alfvén waves propagate at the Alfvén speed given by

$$v_A = \frac{B_0}{\sqrt{\mu\rho_0}}. \tag{1.25}$$

When both gas pressure and the magnetic field are considered, the fast- and slow-mode magnetoacoustic waves are introduced. Essentially, these are modifications of the Alfvén and acoustic waves, but the restoring forces depend on the relative speeds of these pure waves (Stein & Leibacher 1974). Table 1.2 expresses the restoring forces in each of these modes. It should be noted that the slow-mode wave will always travel at a velocity approximately equal to the lesser of c_s and v_A, but always less than both. This is a consequence of the relation giving the slow-mode speed v_s, in a flux tube of enhanced density with respect to that of its environment, ρ_e (as found in coronal loops) :

$$\frac{1}{v_s^2} = \frac{1}{c_s^2} + \frac{1}{v_a^2} \tag{1.26}$$

(Roberts 2000). Similarly, the fast-mode or *kink* speed v_f will tend to the greater of these same speeds, but always be greater than both:

$$v_f^2 = \frac{\rho_0 v_A^2 + \rho_e v_{Ae}^2}{\rho_0 + \rho_e}. \tag{1.27}$$

Consequently, in an homogeneous slab geometry, $\rho_0 \to \rho_e$, $v_f \to v_A$, and the distinct kink mode vanishes.

Table 1.2: Summary of the fast, slow and Alfvén modes in a magnetised plasma. For each mode, the third and fourth columns describe the restoring force, the direction of the perturbation **u** and the velocity at which the wave propagates. After Stein & Leibacher (1974).

Wave mode	Propagation direction	$v_A \ll c_s$ (weak field)	$v_A \gg c_s$ (strong field)
Slow	Approximately parallel to $\mathbf{B}_0$	Magnetic tension $\mathcal{T}_B$ $\mathbf{u} \perp \mathbf{k}$ $v \sim v_A$	Gas pressure p $\mathbf{u} \parallel \mathbf{B}_0$ $v \sim c_s$
Fast	Isotropic	Gas pressure p $\mathbf{u} \parallel \mathbf{k}$ $v \sim c_s$	Magnetic pressure p_B $\mathbf{u} \perp \mathbf{B}_0$ $v \sim v_A$
Alfvén	Parallel to $\mathbf{B}_0$	Magnetic tension $\mathcal{T}_B$ $\mathbf{u} \perp \mathbf{k}$ & $\mathbf{B}_0$ $v = v_A$	

In the chromosphere, transverse fast-mode waves may provide a means of transporting energy along the bright-point and intra-network magnetic field, into the upper chromosphere. Because of the density gradient in the upper chromosphere, acoustic and slow-mode waves do not propagate efficiently. Horizontal buffeting motions of a sufficiently short timescale, however, can excite upward-propagating fast-mode waves (Hasan & Kalkofen 1999). Although these waves themselves are unlikely to dissipate quickly enough to heat the local atmosphere, they may couple with longitudinal slow-mode waves higher in the atmosphere where $v_s \sim v_f$. These slow-mode waves can then form shocks in the density gradient in the upper chromosphere, heating the atmosphere by shockwave dissipation (Ulmschneider 1991).

Convection-driven stochastic motions in the photosphere are a known candidate for excitation waves which reach the transition region and corona. Magnetic loops are of higher density than the atmosphere, with a corresponding lower Alfvén speed. Alfvén and magnetoacoustic waves therefore are trapped in these structures. However, reconnections of magnetic threads in these structures may also excite oscillations

(Nakariakov *et al.* 1999). It is strongly suspected that MHD waves are responsible for transporting a good deal of energy into the corona, but the principal problem with this idea is that Alfvén and fast-mode damping rates are far too small for low frequency waves to transfer their energy to the ambient plasma (Porter, Klimchuk & Sturrock 1994a). For this reason there is currently a good deal of work – to which this thesis contributes (Chapters 5 & 6) – toward detecting waves of period $\lesssim 1.0$ s, which carry enough energy, and can damp quickly enough, to heat the solar corona.

1.4.4 Magnetic reconnection

Magnetic reconnections require a plasma to have resistivity, so that oppositely-directed field lines can diffuse towards each other across magnetic *neutral lines* or 2-D sheets, thereby releasing the energy stored in the magnetic field. However, across very narrow current sheets (small L in Equation 1.20), separating opposite magnetic field vectors, resistive instabilities can set in. These permit reconnections which are discussed in more detail in Chapter 4. Reconnection scenarios in all parts of the corona are discussed in Moore *et al.* (1999). Flares typically release energies in the range 10^{30} – 10^{32} ergs over timescales of up to several hours. Because flares do not release sufficient energy over time to heat the corona, recent studies (Hudson 1991; Krucker & Benz 1998; Parnell & Jupp 2000) have also focused on the frequency distribution of microflares and nanoflares (Parker 1988). These events are reconnections releasing much smaller amounts of energy $\sim 10^{-6}$ and 10^{-9} that of normal flares, respectively. The assumed power-law distribution of frequency of event $F(E)$ with energy E is continually being constrained and, depending upon the index for this law, there may be enough energy in reconnection processes to heat the quiet Sun and coronal holes. The radiative losses from active regions, however, are orders of magnitude higher, and may not be so easily explained.

1.5 Description of this thesis

This thesis investigates a range of both static and dynamic phenomena in the transition region and corona of the Sun and other late-type stars. Chapter 2 is a preamble to the following chapters, and details the instrumentation used in the reported observations.

Chapter 3 investigates the validity of the optically thin assumption in stellar transition regions and coronae. Although densities and geometries vary from star to star, it is suspected that strong transition region lines, such as those listed in Table 1.1, may in fact be optically thick. We make use of observations in prominent emission lines from a range of ions to determine the opacity in these lines. Densities are also calculated from sensitive line ratios, which allow the estimation of path lengths for the emitting regions in the upper atmosphere of each star. Since flares are known to produce density enhancements, a flare star is observed and shown to exhibit greatly increased opacity in its emission during a flare.

Chapter 4 leads from the analysis of unresolved flares on cool stars to a similar event on our own Sun. Presented are data in a broad-spectrum, multi-wavelength analysis of a solar flare in an active region near the solar limb. The observations range from the visible, using data from a ground-based solar telescope, through the ultraviolet and extreme ultraviolet with the *TRACE* mission, and finally to soft and hard X-rays with the *GOES* and *CGRO* missions, respectively. Although the flare is not particularly energetic in its soft X-ray or Hα flux, it produces a spray event in which large amounts of plasma are ejected from the Sun. The timing and morphology of this unusual event are presented. Finally, the balance of energy between high-energy particles directed downward to the chromosphere and those ejected outward is estimated.

Chapter 5 forms the largest single chapter in this thesis. In this chapter are presented observations by a new ground-based, high-time resolution system: the Solar Eclipse Corona Imaging System. The observations are taken at a sampling rate of 44 frames per second, and are used to search for short-period oscillations and microflare activity

in the corona, either or both of which may heat the solar corona and balance its radiative losses. The observations are made both in white light (which acts as a control 'channel') and the prominent coronal emission line of Fe XIV at λ5303 Å which detects emission primarily from coronal structures such as active region loops. The search for oscillations is carried out on time series of Fe XIV intensity, using the relatively new method of wavelet analysis. This method has the principal benefit of being able to localise oscillatory behaviour in time as well as in frequency space, a facility lacking in familiar discrete Fourier transforms. After surveying the most prominent active region in the data, an oscillation is identified with a period of 6 seconds in an active region loop. This period corresponds closely to the estimated required frequency range for magnetoacoustic wave heating of the solar corona.

Chapter 6 continues the investigation of the detected oscillation by extending the analysis of the data. A determination of the precise mode is carried out, as are estimates of the damping length of the wave in various mode scenarios. Because of the velocity and travelling nature of the 6-second oscillation, it is concluded that the wave is most likely an impulsively generated fast-mode wave. Estimates of the wave's flux and the radiative energy loss from the loop are also finally carried out and compared, in an attempt to establish the culpability of the wave in heating the local plasma.

Lastly, Chapter 7 summarises the conclusions of this thesis and establishes future directions for the work presented herein.

Chapter 2

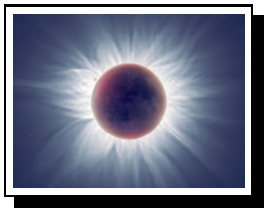

Instrumentation

2.1 Introduction

The scope of the observations presented in this work takes us from the optical régime viewable from Earth to extreme ultraviolet (EUV) wavelengths, and – as such – requires that we use a range of different instruments, with both solar and stellar targets. This brief chapter details the observationally relevant characteristics of all the instruments used to gather data presented in this thesis.

The ground-based facilities used in the presented analyses are the *Dunn Solar Telescope* (DST) in New Mexico, and the Solar Eclipse Corona Imaging System (SECIS). The remaining instruments flew aboard – or constituted – spacecraft which continue to be operational (*TRACE, SoHO, HST*).

2.2 The Goddard High-Resolution Spectrometer

The *Goddard High-Resolution Spectrometer* (GHRS) was a first-generation mission aboard the *Hubble Space Telescope* (HST), launched in April 1990. The instrument was ultimately succeeded by the *Space Telescope Imaging Spectrometer* (STIS) after GHRS' 'catastrophic failure' in January 1997.

GHRS' design was that of a modified Czerny-Turner spectrograph, and is shown in Figure 2.1. GHRS had a wide wavelength range in the ultraviolet, from 1100 Å to 3200 Å, and offered: five gratings – of varying resolutions and individual ranges – which provided single-order spectra; and to two échelle modes, providing cross-dispersed, two-dimensional spectra. In practice, however, the G140L and Ech-A (higher order) modes were unavailable due to problems with the instrument's power supply. Table 2.1 gives a brief synopsis of each mode's spectral range. GHRS was also capable of imaging its target through either the large or small entrance ('science') apertures (LSA and SSA respectively). These apertures were effectively reduced by only 12% with the installation of the COSTAR (*Corrective Optics Space Telescope Axial Replacement*)

Table 2.1: GHRS' useful wavelength ranges in the first-order and echelle gratings. The gratings are labelled 'G', the three-digit number represents the centre of the grating's range in nanometres, and the 'L' and 'M' suffixes denote low and medium resolution respectively.

Grating	Useful Range (Å)	Resolution $\left(\frac{\lambda}{\delta\lambda}\right)$	Bandpass (Å)
G140L♠	1100–1900	2 000	286–287
G140M	1100–1900	26 000	28–26
G160M	1150–2300	23 000	36–33
G200M	1600–2300	26 000	41–38
G270M	2000–3300	29 000	48–44
Echelle-A♠	1100–1700	100 000	5.5–9
Echelle-B	1700–3200	100 000	8.5–17

♠ unavailable during commission due to power supply problems

to *HST* in December 1993. In the interests of being relevant to our later discussions, however, the imaging capabilities are ignored, since we deal only with one-dimensional spectra from the 'G' gratings.

2.2.1 Detectors & Gratings

The two detectors with which we are concerned are labelled D1 (a.k.a. 'Side 1') and D2 ('Side 2') in Figure 2.1. D1 was used to detect the shorter wavelength UV light, and was coated with caesium iodide to give the best response in the 1050 – 1700 Å range. However, with the introduction of the COSTAR optics, the mirrors' combined reflectance at wavelengths below 1150 Å was almost negligible. The faceplate of the detector was made from lithium fluoride, allowing a high transmittance at the short wavelengths for which it was designed. D2, by contrast, lay behind a faceplate of magnesium fluoride, with severe attenuation below Lyα (1216 Å). D2 was coated with caesium telluride which has best response in the range 1700 – 3200 Å). As seen in Figure 2.1, the gratings were mounted on a carousel, such that the G140M and (defunct) G140L gratings dispersed the incident light onto the D1 optics, while gratings G160M,

G200M and G270M dispersed light onto the D2 optical system.

2.2.2 Data

The GHRS data used in this work were downloaded via the *HST* Science Archive at

`http://archive.stsci.edu/cgi-bin/hst_science_search` .

The archive allows the user to search for data from a particular object or co-ordinates, and returns a list of data files which may be selectively downloaded. The data are received as pure ASCII data, in two-column (wavelength & intensity) format, while the details of exposure times, observation dates, etc. are given by the online archive file listing.

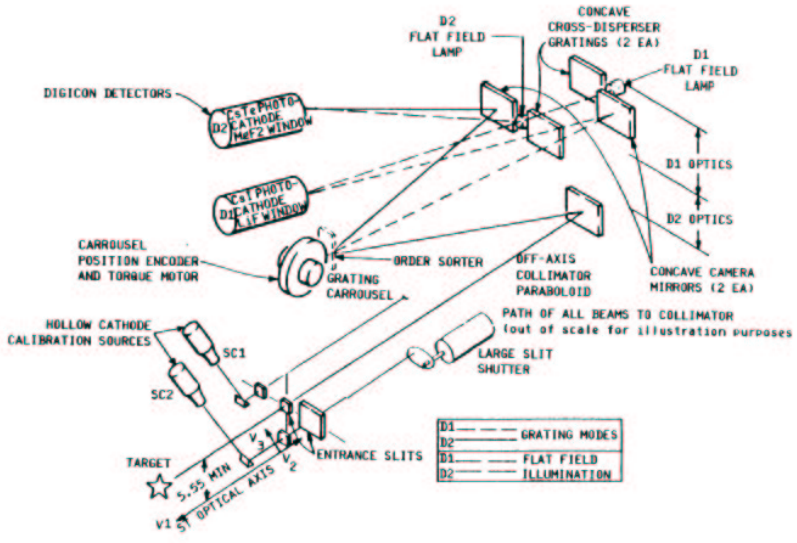

Figure 2.1: Optical layout of the GHRS instrument

2.3 The Transition Region And Coronal Explorer

2.3.1 Introduction

The *Transition Region And Coronal Explorer* (*TRACE*) satellite mission (Handy *et al.* 1998), built and managed by LMSAL, was launched in February 1998 as part of NASA's Small Explorer (SMEX) programme. It is a single-instrument mission, although it has filters covering a range of the UV and EUV spectrum. Table 2.2 lists the filters available on *TRACE*, including the primary wavelength (and emitting ion) for which each filter is designed. *TRACE* was put into a Sun-synchronous orbit (orbital

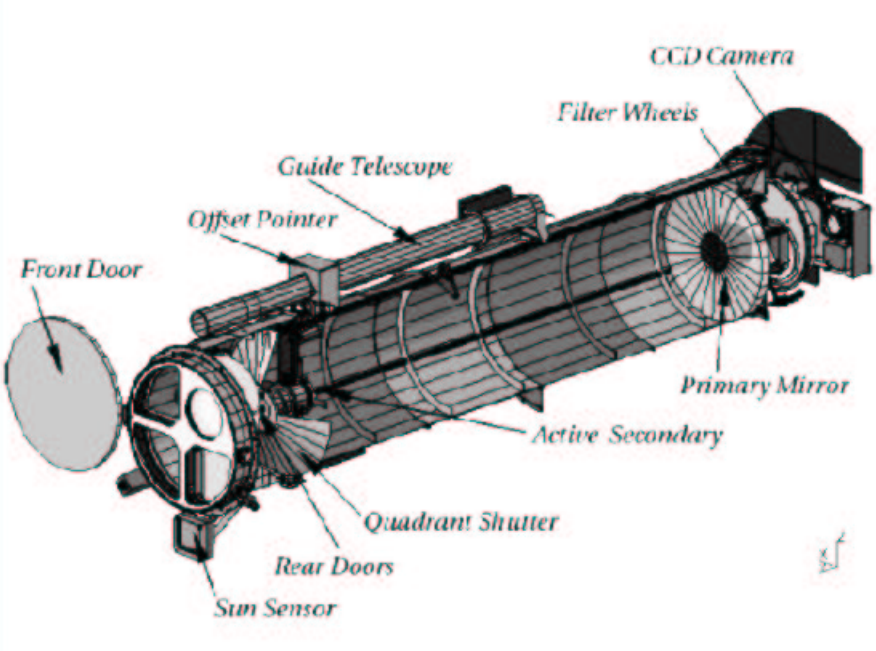

Figure 2.2: Schematic layout of the *TRACE* instrument (taken from the *TRACE* Analysis Guide (TAG; Bentley 2001)).

plane at 98° inclination to the Earth-Sun line) in April 1998 by a Pegasus rocket launch vehicle. Its orbit ensures that *TRACE* spends most of its time with a clear view of the Sun, but periodically endures a day-and-night cycle (once each orbit) for around three months at a time (known as its 'eclipse season').

2.3.2 *The TRACE* telescope

The scientific instrument is a Cassegrain telescope with four entrance quadrants at the aperture, which are selectively opened by the rotation of the open-quadrant shutter (Figure 2.2). The aperture itself is coated in such a way that any light apart from far UV and EUV radiation is reflected. The quadrants of the entrance aperture are assigned to different narrowband EUV and broadband UV passbands (Table 2.2), with one quadrant per EUV passband (A, C & D), and the remaining quadrant used for the ultraviolet passbands (B); these are matched by corresponding, appropriately-treated quadrants of the primary and secondary mirrors. The secondary mirror is active, in that it can correct for pointing 'jitter' to within $0.1''$. The filtering is achieved by two filter wheels at the rear of the telescope. The filters in these wheels can be combined in various ways to achieve either different levels of response in the EUV quadrants, or different passbands in the UV quadrant.

The Lumogen-coated CCD was originally designed for the *Michelson Doppler Imager* experiment aboard the NASA/ESA *SoHO* mission (Fleck, Domingo & Poland 1995). It has a pixel depth of 12 bits, and the gain is set to saturate the pixels at 20% of full-well capacity, to avoid charge leakage to neighbouring pixels in the event of intense radiation.

TRACE enjoys a resolution of $0.5''.\text{pixel}^{-1}$, which means that it can resolve structures on the Sun with dimensions down to $\sim$700 km. Although ground-based solar telescopes can currently achieve angular resolution of $0.15''.\text{pixel}^{-1}$, no prior EUV or UV solar missions (*SMM*, *Skylab*) had achieved anything like this level of detail. With sufficiently small integration times, its cadence can also be reduced to a few seconds. The information which can be gleaned from such detailed observations is highlighted by the observations of MHD wave damping times by Nakariakov *et al.* (2000).

Table 2.2: TRACE observation passbands

Target species	Wavelength (Å)	Bandwidth (Å)	Formation temperature Log (K)	Mirror quadrant
Fe XV	284	10.7	6.1–6.6	D
Fe XII	195	6.5	5.7–6.3	C
Fe IX/X	171	6.4	5.2–6.3	A
C IV	1550	20	4.8–5.4	B
H I (Lyα)	1216	84.0	4.0–4.5	B
C I/Fe II/UV cont.	1600	275	3.6–4.0	B
Continuum (UV)	1700	200	3.6–4.0	B
Continuum (visible)	5000	broad	3.6–3.8	B

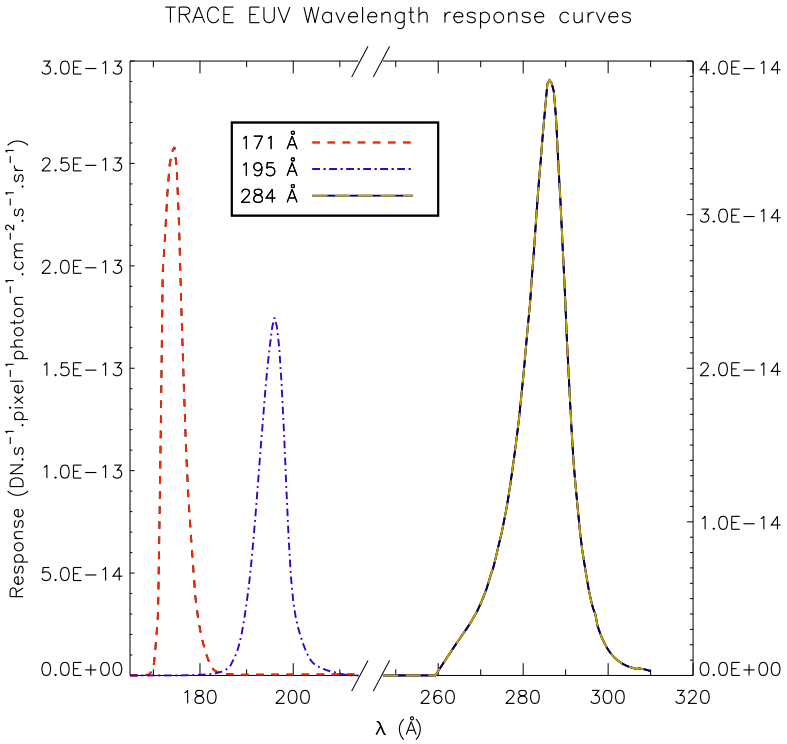

Figure 2.3: Wavelength response of *TRACE* in the EUV passbands.

2.3.3 Data

All data used in this work were downloaded via the *TRACE* data archive, operated by Lockheed Martin Space & Astrophysics Laboratory (LMSAL), and mirrored at several sites, including RAL. The data can be obtained in either individual standard FITS for-

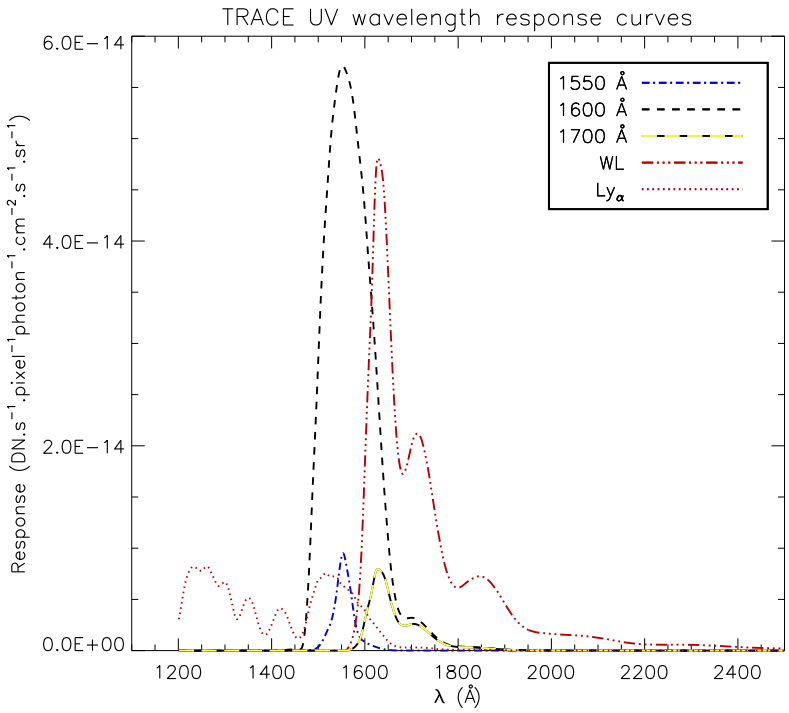

Figure 2.4: Wavelength response of *TRACE* in the UV passbands.

mat images with headers, or MXF (Multi-Extended FITS) format files which contain multiple FITS image/header pairs, in blocks of up to one hour's-worth of observations. Data are typically received through `FTP`.

2.4 The Dunn Solar Telescope (DST)

2.4.1 Introduction

The *Richard B. Dunn Solar Telescope* (DST) was dedicated in 1969 as the *Vacuum Tower Telescope* (VTT) at the US National Solar Observatory's facility on Sacramento Peak, New Mexico. (The re-dedication in 1998 was in recognition of the VTT's inventor.)

The tower, from which the design takes its name, stands 41.5 m above ground,

with a further vertical extent of 69.5 m below ground. The larger part of the optical path is through a contiguous series of evacuated tubes, weighing a total of 185 tonnes. This considerable weight is suspended from a low-friction mercury float at the top of the tower. This allows the tube structure to rotate about its vertical axis. The superstructure is topped by a pair of mirrors, also *in vacuo*, which act as a heliostat for the telescope. Whereas a coelostat compensates for both the Sun's motion across the sky *and* its rotation, a heliostat (see §2.7.2.3) compensates only for its proper motion; however, the rotation of the VTT's optics on the mercury instead compensates for the apparent rotation of the solar axis. After the light is reflected down the tubes from the heliostat, it strikes the 1.6-m primary mirror at the (subterranean) base of the tower. The primary, which can be tilted to divert the beam to various instruments, reflects the light back to ground level, where it is diverted out of the vacuum tube and into a horizontal path toward the optical bench.

2.4.2 Optics

The data taken on 1998 September 27 (Chapter 4) were taken using three different instruments present at the DST: the tuneable Universal Birefringent Filter (UBF; Bonnacini *et al.* 1989); a Hallé Ca II K-line filter (3934 Å); and a Thomson filter centred on the photospheric 'G-band' (4305 Å) of CH. The left- and right-hand circularly polarised lines of the Fe I λ6302 line are compared to infer the local magnetic field strength by analysing the Zeeman split (see Gallagher (1998) for more details on this). The lines used in the optical analysis are marked with a ♣ superscript in Table 2.3. The DST observations included in this work are therefore all taken by the UBF; all the UBF images presented have an angular resolution of $0.17''.\text{pixel}^{-1}$. The data from the UBF are in FITS format, with multiple frames per file reflecting the multiple passbands chosen for the observations. To view the solar atmosphere in a particular band at any observed time, each file is read into IDL as a data cube (i.e. with dimensions x, y and n, where n is the frame number), and the appropriate frame in each is selected and stored. Time

Table 2.3: DST observation wavelengths

Line	Wavelength (Å)
Thomson G-band	4305.0
Hallé Ca II K_3	3933.7
H_α	6562.8
H_α +0.65 Å♣	6563.5
H_α +1.00 Å♣	6563.8
Mg I b_1 −0.40 Å	5183.2
Mg I b_2♣	5172.7
Fe I (*LCP*)	6302.4
Fe I (*RCP*)	6302.4
Continuum	5256.4

♣ wavelengths analysed in this work.

series are constructed by summing intensity over selected areas and storing as a vector of intensities (see Chapter 5 for further details).

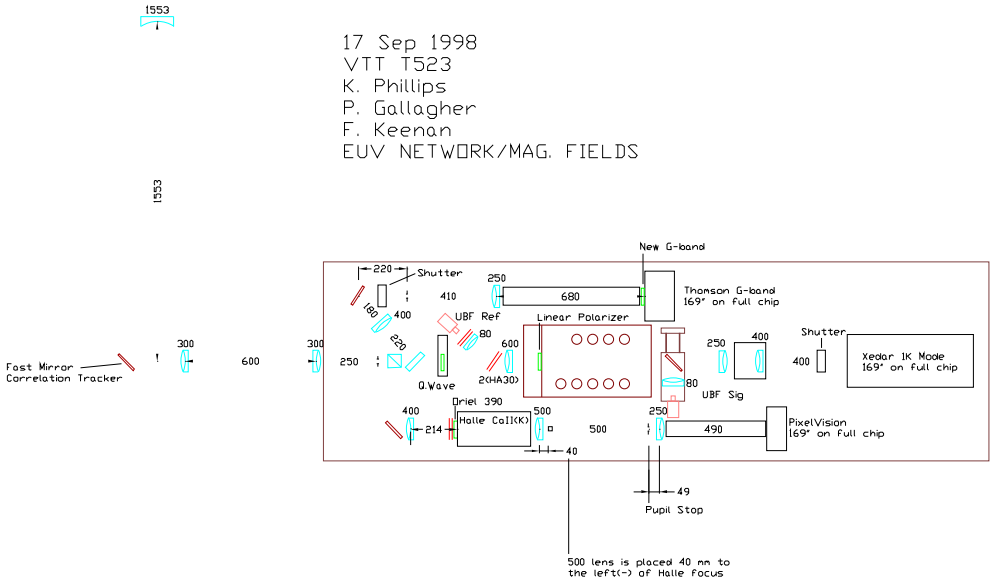

Figure 2.5: Setup of the VTT optics used to observe NOAA AR 8340 on 1998-Sep-27.

2.5 The Coronal Diagnostic Spectrometer

2.5.1 Introduction

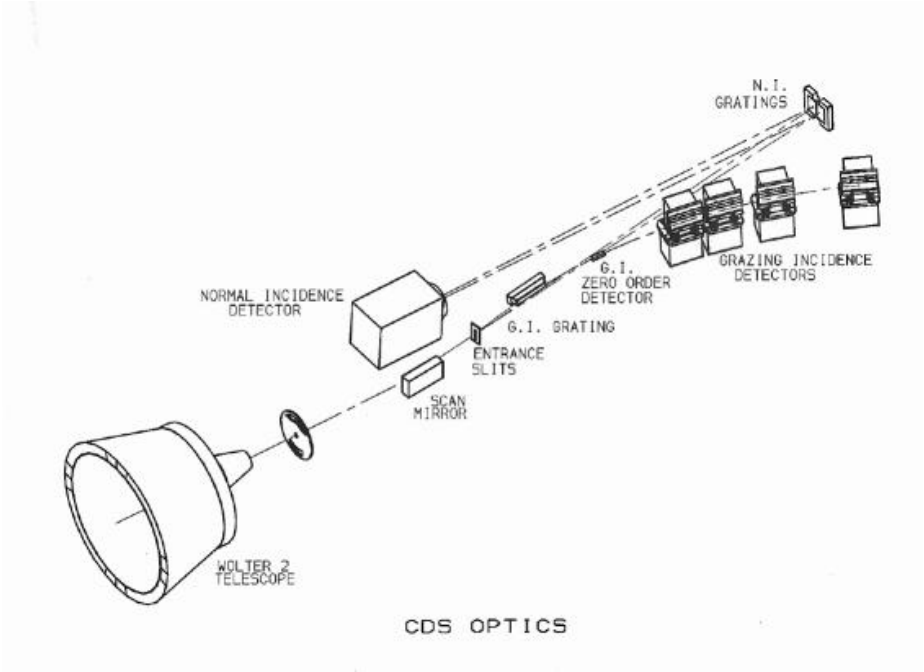

Figure 2.6: Optical schematic of the CDS instrument aboard *SoHO*, showing the light paths to the Grazing Incidence Spectrometer (GIS) and the Normal Incidence Spectrometer (NIS).

The *Coronal Diagnostic Spectrometer* (CDS; Harrison *et al.* 1995) is a dual-mode EUV spectrograph instrument on board *SoHO*. The CDS consortium is comprised of several solar physics research groups, including groups at RAL, Mullard Space Science Lab (MSSL), and NASA/Goddard. The consortium's primary goal is to shed light on the driving forces behind the heating of the corona and the acceleration of the solar wind, and aims to do so by probing the coronal plasma through its EUV emission. The EUV régime contains many lines whose mutual ratios are very sensitive indicators of density, temperature and opacity. In addition, since CDS is capable of imaging chosen parts of the corona, it can be used to develop density, temperature and velocity maps of the observed region, when used in conjunction with accurate atomic data.

Table 2.4: Primary observational characteristics of the two CDS detectors.

	GIS	NIS
Wavelength ranges (Å)	151 – 221 256 – 338 393 – 493 656 – 785	308 – 311 513 – 633
Prime slits (arseconds)	2×2 4×4 8×50	2×240 4×240 90×240

2.5.2 NIS & GIS

CDS is comprised of two primary detectors: the Normal Incidence Spectrometer (NIS) and the Grazing Incidence Spectrometer (GIS). Normal incidence reflection from gratings is highly attenuated at very short EUV wavelengths and, for this reason, GIS was designed to complement NIS by observing the corona at shorter wavelengths. Table 2.4 lists the main scientific features of the CDS detectors. It is noticeable that GIS' wavelength range is considerably broader than that of NIS. This is because grazing incidence can be efficiently employed at wavelengths of up to ∼1000 Å. The available slits for GIS, however, are notably smaller than those of NIS; for this reason, NIS is much more effective in creating large-area rastered images of the Sun (see §2.5.2.1). Since GIS is not used for any of the observations described in this work, it will suffice to give a description of NIS and its detector system.

2.5.2.1 The NIS dispersion system

The dispersion system used for NIS utilises a Rowland circle design, an example of which is illustrated in Figure 2.7. In the case of NIS, the grating is divided into two parts: the first with a dispersion of 3.17 Å.mm^{-1}; the second with 5.56 Å.mm^{-1}. NIS forms images of the chosen slit on the detector such that the slit is perpendicular to the dispersion axis. The former half of this grating is used to disperse incoming light onto

the upper part of the detector (referred to as NIS1) and the latter onto disperses onto the lower part of the detector (NIS2). NIS greatly reduces any potential astigmatism by using normal incidence dispersion over relatively small wavelength ranges (Table 2.4), so that it enjoys good spatial and spectral resolution. A slight tilt of the two halves of the gratings, with respect to one another, allows a vertical displacement of the two projected slit spectra onto the single detector (§2.5.2.2). NIS is capable of building up a time-lapse movie of the area on the Sun imaged by the slit, and of rastering the slit across a chosen area of the Sun to build up a 3-dimensional image (wavelength, Solar_Y and Solar_X or time). Figure 2.8 shows this system schematically.

2.5.2.2 The VDS detector

The NIS detector is known as the *Viewfinder Detector Subsystem* (VDS) and is essentially an intensified CCD system. A microchannel plate (MCP) detector at the front of the VDS generates an electron cascade (photoelectrically) for each incident EUV photon. A standard phosphor (P-20) then converts the electrons into visible light which is

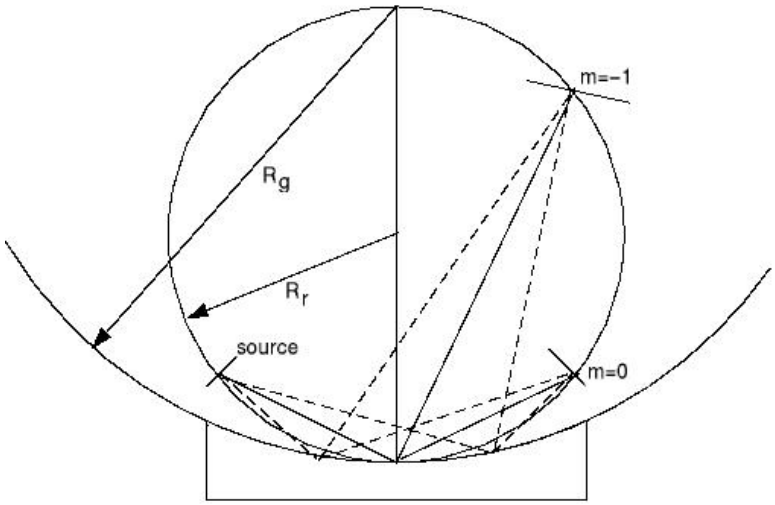

Figure 2.7: Schematic of a Rowland circle spectrograph (adapted from the online X-ray lithography tutorial at Wisconsin University). The concave grating has a radius of curvature R_g equal to twice the radius of the Rowland circle, R_r. It should be noted that the circle is not a tangible object, but merely a locus of the focal points of the light reflected from the concave grating, along which detectors are placed.

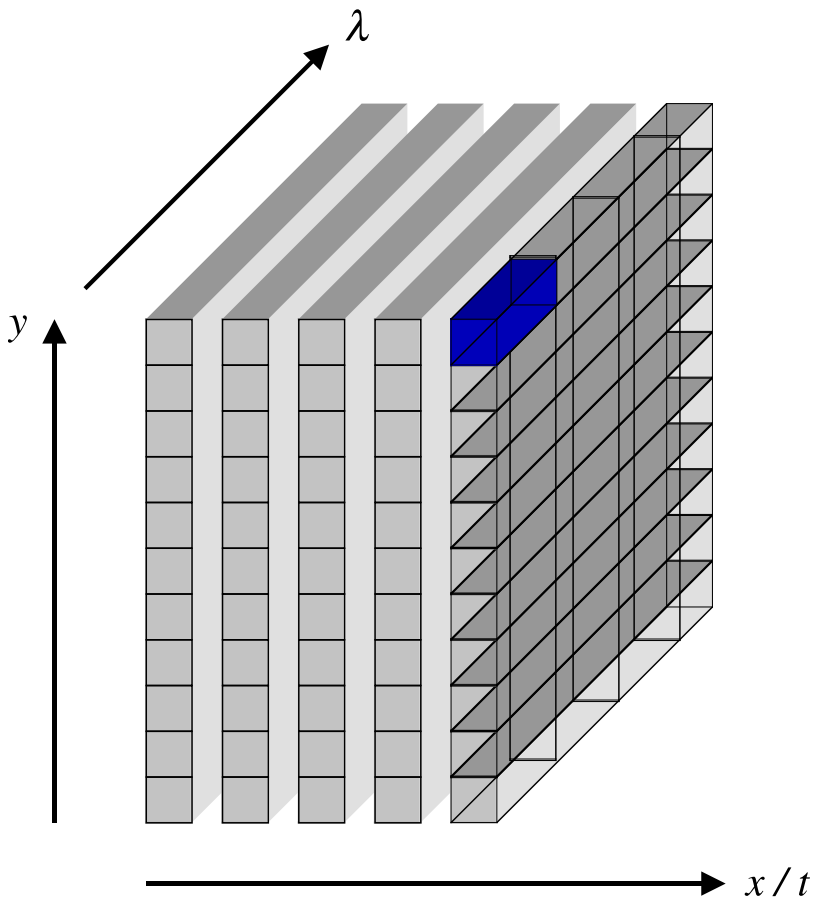

Figure 2.8: Schematic of how NIS rasters across multiple slit images of the Sun to build up 3-dimensional image 'cubes' which can either be movies (third dimension is time) or X-Y images of the Sun (third dimension is Solar_X). The highlighted block represents a single pixel with *y*, λ and *x* (or *t*) co-ordinates. The projected spectra of NIS1 and NIS2 can be thought of as being in the *y*-λ plane.

picked up by the CCD.

2.5.3 Data

Data from the NIS system are a little unusual in that arbitrary spectral 'windows' are chosen in NIS1 and NIS2. Each window represents a 2-dimensional area on the CCD defined by the projected height of the spectrum and a chosen range along the dispersion axis. This presents significant advantages when rapid series of exposures are required. Each window is assigned a label, and all the chosen windows – together with the ex-

posure times and slit pointings – define an observing 'sequence'. Data are stored in a modified FITS format, and a vast suite of tools for IDL *SolarSoftWare* are available to calibrate the data, extract and analyse images and spectra, etc.

Since the CDS/NIS data presented in this work were taken after the recovery of *SoHO* in 1998, it is worth noting that the instrumental line profiles were modified in the NIS1 and NIS2 detectors. The change in line profiles is more evident in NIS1 than in NIS2, but the changes in each detector are qualitatively similar. Whereas the profiles had previously been Gaussian, and of the form

$$G(\lambda) = \exp\left[-\frac{1}{2}\left(\frac{\lambda-\lambda_0}{\sigma}\right)^2\right], \tag{2.1}$$

the post-recovery profiles included an extra 'wing' term described by

$$W(\lambda) = \frac{1}{\left(\frac{\lambda-\lambda_0}{\sigma'}\right)^2 + 1}. \tag{2.2}$$

After much empirical testing, the σ' function was defined as

$$\sigma' = 2\sigma\sqrt{2\ln(2)}. \tag{2.3}$$

(Thompson 1999). With this relation for σ', the FWHM of $W(\lambda)$ is exactly twice that of $G(\lambda)$. These terms combine to describe the new profile shown in Figure 2.4:

$$B(\lambda) = A_0[(1-\alpha)G(\lambda) + \alpha W(\lambda)] \tag{2.4}$$

where A_0 is the amplitude of the line profile and α can take different values depending on whether the wing is on the 'blue' or 'red' side of the line.

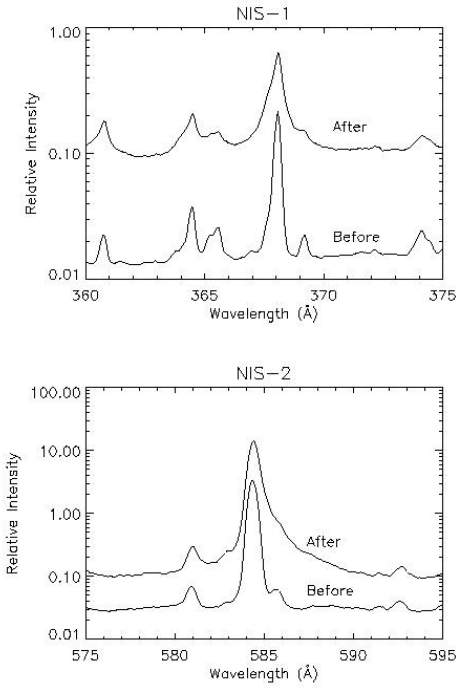

Figure 2.9: Pre- and post-recovery line profiles in the NIS1 and NIS2 detector systems, which are fitted by the relation given Equation 2.4 (taken from Thomson (1999)).

2.6 The Extreme Ultraviolet Imaging Telescope

2.6.1 Description

The Extreme Ultraviolet Imaging Telescope (Delaboudinière *et al.* 1995) is a four-bandpass instrument capable of imaging the Sun in both full-disc mode and in selected areas out to a distance of $1.5R_{\odot}$. EIT is the first instrument able to make uninterrupted observations of the Sun in the EUV thanks to SoHO's orbital position at the L1 Earth-Sun Lagrangian point.

2.6.2 Instrumentation

EIT's CCD is made of 1024×1024 21 μm pixels, giving the system a spatial resolution of is $2.62''$.pixel^{-1}. It can therefore resolve structures on the Sun down to a scale of

Table 2.5: Filter bandpass information for *SoHO*/EIT (taken from Delaboudinière *et al.* (1995)).

Wavelength (Å)	Ion	Formation Temperature
304	He II	8.0×10^4
171	Fe IX/X	1.3×10^6
195	Fe XII	1.6×10^6
284	Fe XV	2.0×10^6

$\sim$4000 km. The telescope itself is a Ritchey-Chrétien design; this design's main disadvantage is a moderate astigmatism, which is not a real concern for EIT observers since it is designed to look at narrowband filtergrams of the Sun. The hyperbolic mirrors are coated with a molybdenum/silicon mixture and, like *TRACE,* each filter corresponds to a matched quadrant of the mirrors with each mirror quadrant being appropriately treated. Again, as on *TRACE,* light is admitted via an open-quadrant shutter.

The filters contained in the filter wheel are listed in Table 2.5, and the wavelength response profiles are shown in Figure 2.11.

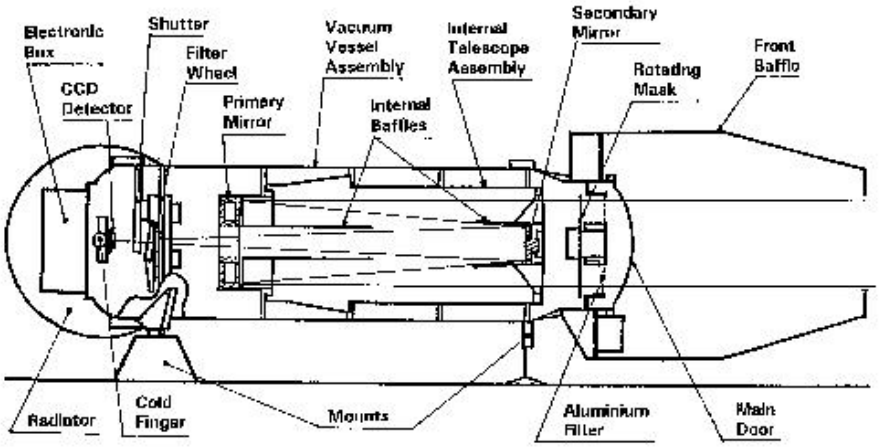

Figure 2.10: Layout of the optical system of EIT

2.6.3 Data

Data from the 1024×1024-pixel^2 CCD are saved, either whole or windowed, in a modified FITS format. These data may then be read, calibrated and analysed using the EIT suite of SSW software. EIT shares a telemetry system with the Large Angle Spectroscopic Coronagraph (LASCO), with a combined telemetry rate of 5.2 kbps. Consequently, high-cadence observations are only really possible if the CCD is used in windowed mode (the full-frame readout time being 21 s).

The use of narrowband filters means that emission measure distributions can more easily be made since the filters will encompass only one (or two) very strong lines in the EUV. The data also complement those from the *Soft X-ray Telescope* aboard the NASA/ISAS/PPARC *Yohkoh* satellite (Svestka & Uchida 1991), since they image a part of the corona at temperatures lower than that seen in soft X-rays.

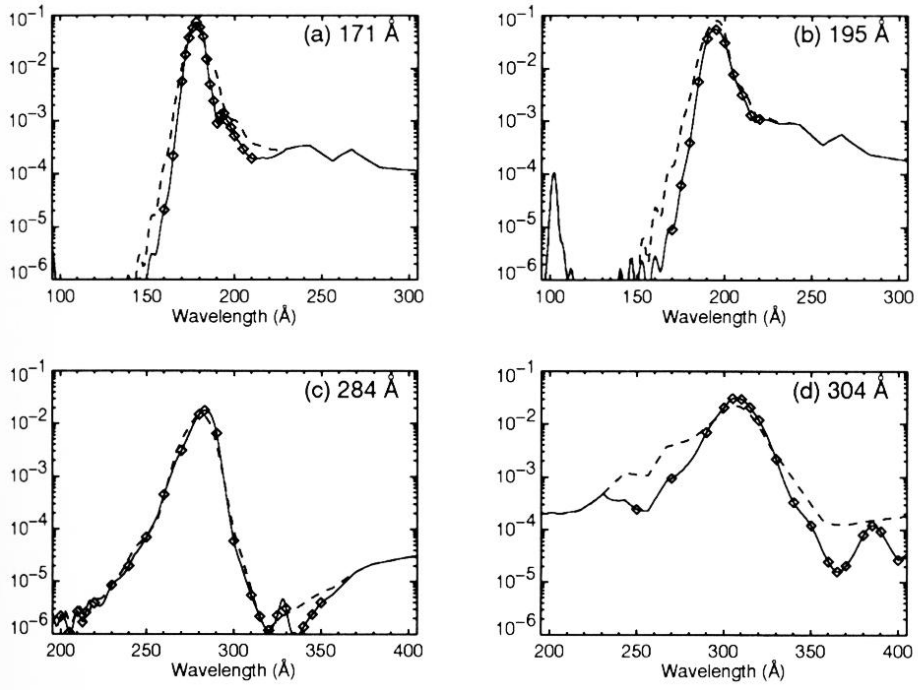

Figure 2.11: Plots of the wavelength response of EIT in each of its four bandpasses, from Delaboudinière *et al.* (1995).

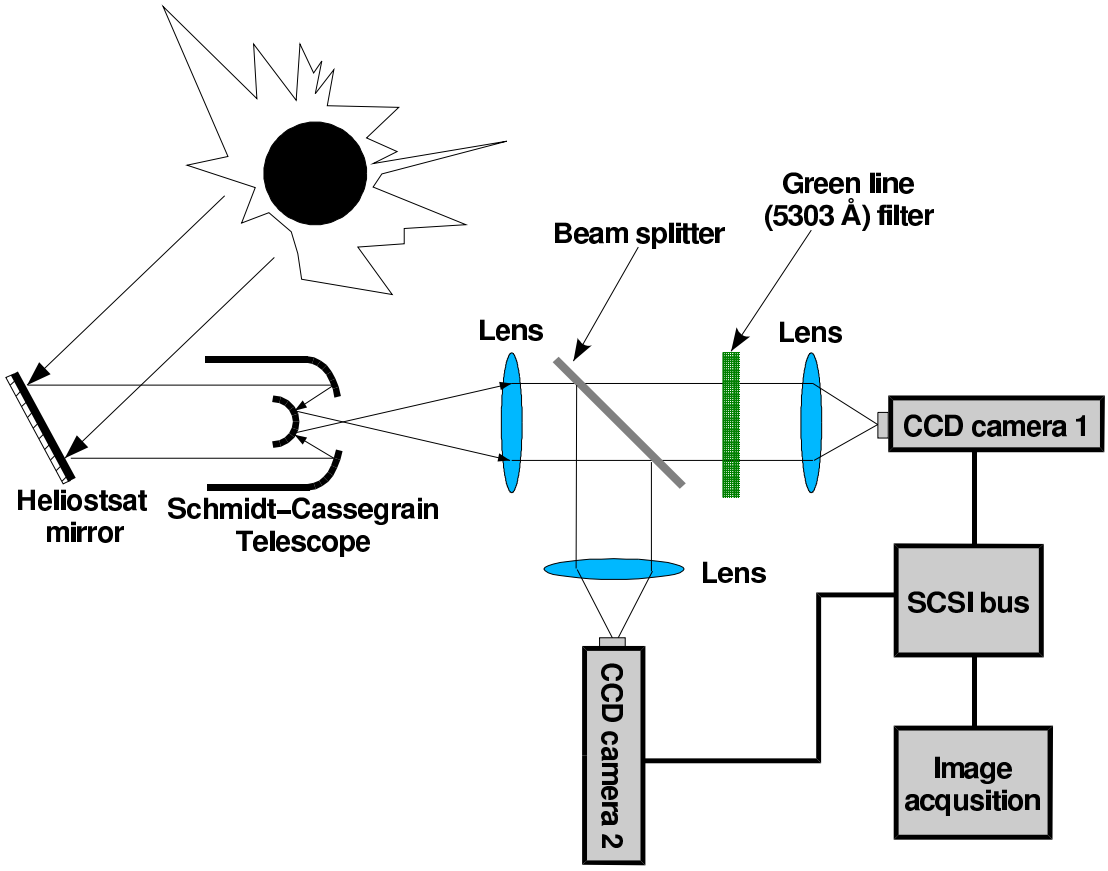

Figure 2.12: Schematic diagram of the SECIS instrument used during the 11th August 1999 total eclipse.

2.7 The Solar Eclipse Corona Imaging System

2.7.1 Experiment description

The SECIS instrument is a collaboration between the University of Wrocław, the Rutherford Appleton Laboratory and Queen's University Belfast. It has been designed to look for fast changes in the solar corona, a brief that includes nano- and micro-flares as well as short-period oscillatory signals generated by waves in the corona. The idea behind SECIS is the ability to record a high number of frames per second. The maximum detectable (or 'Nyquist') frequency of a time series is exactly equal to half the rate of sampling. Hence, if a detector samples intensity at a rate of 60 frames per second, then the maximum detectable frequency in the resulting data will be 30 Hz. In order to detect high-frequency oscillations, then, it is necessary to sample at high frequency also

– at least twice as high as the maximum frequency we expect to observe. This presents technical challenges for any data collection system.

In the context of the field of solar oscillation studies, it should be explicitly stated that SECIS is a photometric experiment, not spectroscopic or spectrographic. The expected flux from the Fe XIV line is sufficiently weak that distribution of the incoming photons across a dispersion axis, as in a spectrographic system, is impractical. Koutchmy *et al.* (1983) presented a contemporary list, similar to that of Aschwanden *et al.* (1999), of detected coronal oscillations, along with the methods by which these oscillations were found: fluctuations in intensity, velocity or line width. The SECIS instrument observes in two channels: a green-line filter of measured FWHM 4 Å (manufactured by Barr Associates, Westford, Massachusetts), centred on 5303 Å with maximum transmission of 27% at this wavelength; and a white light channel, with no filter in place, which observes the continuum corona emission. (If desired, though, a filter can also be placed in front of this camera, *e.g.* centred on the cooler 'coronal red line' of Fe X (6374 Å), or a broad-band filter to view the local coronal continuum). The channel of primary interest in observing coronal structures with SECIS is therefore the green-line channel, while the white light channel acts as a reference channel for monitoring atmospheric disturbances, problems with instrumental pointing, etc., since it enjoys a much higher level of signal. A block diagram illustrating the instrumental setup is shown in Figure 2.12.

The heliostat keeps the Sun's light directed onto the telescope by turning at an angular speed equal to half that of the Sun's motion across the sky in both right ascension (RA) and declination (Dec.). The instrument's field of view is $\sim 0.57^\circ \times 0.57^\circ$, and although this is not much larger than the angular size of the solar photosphere, it provides enough coverage for a chosen portion of the limb (approximately half of the limb) out to a significant radial distance, and gives a resolution of ~ 4.05 arcsec.pixel^{-1}.

The horizontal beam enters a telescope mounted on the front of the optical bench, by which it is focused and is then collimated by a lens behind the telescope focus.

The collimated light then continues to a beam splitter which reflects 10% of the light to a perpendicular path. The undeviated component of the light is passed through the green-line filter, and focused onto the first CCD camera, while the reflected component of the light passes unfiltered to the second camera. The integrated exposures are split in the PC's RAM and stored on disk as continous streams before conversion to the FITS standard format for analysis at a later stage.

2.7.2 SECIS Instrument description & layout

2.7.2.1 CCD cameras & data storage computer

SECIS uses two SuperPhoton model CAM17-16/X224 'frame-drop' CCD cameras built by EEV (formerly of Chelmsford, Essex, UK, now part of Marconi Instruments) which have a maximum frame rate of approximately 70 frame.sec^{-1}. Frame-drop CCD cameras have two parts to their chip, in that one half ('image array') is uncovered while the other ('storage array') is always protected from exposure to light. In principle, light is 'collected' on the image array, and then, on a clock pulse, is transferred to the storage array – in a time much less than conventional readout times – so that the image array can again begin to record. Meanwhile, the only constraint on the readout time is that it should be less than the exposure time, in order that the image array of the CCD should have time to read out the charge before the next exposed frame arrives. In practice, frame-drop CCDs operate in one of two modes: continuous and asynchronous. In continuous mode, the exposure and readout operations are initiated by the same clock pulse, meaning that pixels accumulate a small amount of charge as they are being read. In asynchronous mode, there is a delay between the end of the readout and the beginning of the next exposure, so that no photons are accumulated during readout. The latter mode is the one used during SECIS experiments.

Each pixel has a depth of 12 bits, and dimensions of 15 μm$\times$15 μm. The CCD

chip is arranged in a 512×512 pixel^2 format, and the output clocking rate is 20 MHz. With this clocking rate, the RMS readout noise is approximately 150 electrons (e^-). To put this in context, the full well capacity (the maximum amount of charge held by each pixel) is 200,000 e^-. As the conversion from charge to ADUs (analogue-to-digital units) is necessarily linear – whereas the relationship between accumulated charge and incident intensity is not – we can express the readout noise in terms of its binary readout value:

$$200,000\ e^- \equiv 2^{12}\ \text{levels} = 4096\ \text{levels} \tag{2.5}$$

so the number of levels equivalent to the RMS readout noise is

$$\frac{150\,e^-}{2 \times 10^5\,e^-} \times 4096 = 3.07. \tag{2.6}$$

Using this information, we know that dumping the least 2 significant bits (*i.e.* levels 0–3, when converted from binary) from the 12 bits of data read from each pixel leads to the dumping of a level equivalent to the readout noise. The analogue-to-digital conversion units in each camera use this fact to reduce the amount of redundant data output by 17%. This also leads to a rescaling of the output data, so that (200,000 - 150) e^- is now equivalent to 1024 (2^{10}) levels, *i.e.* the ADU readout for each pixel now represents 195 electrons per pixel; there is a degradation in the signal resolution of the data. However, the reduction of each readout to 10 bits means that 3 consecutive 10-bit words can be run together by the controller cards as a 32-bit data 'word' with only 2 empty bits. Compare this with two 12-bit pixels per word, leaving 8 wasted bits per word, and we see that the method employed greatly enhances the efficiency of data transfer to RAM and disk storage (below).

The computer control of the system is afforded by a custom-built PC system, designed and built by 4C's (Carr Crouch Computer Company) of Maidenhead. It is a dual-CPU system built on a Supermicro P6-series motherboard, with 128 MB of RAM, and runs on Windows NT™ 4.0 Workstation. The system's design brief also included

the need for a high data transfer rate disk system (solved using a RAID array of 4×9.0-GB SCSI disks), control interface to the CCD cameras (via PCI interface cards and Image32™ software both from C-Vision™), and a data backup system (DAT DDS 3 backup tape drive).

The Image32™ software allows a certain degree of control over the cameras' operation. The exposure time and the delay between exposures (necessary for the asynchronous mode frame-drop transfer action) are controlled from a single dialogue box, while the field of view of one camera at a time can be monitored by selecting a 'burst mode'; this is most useful in aligning the cameras with respect to the Sun and one another. The software also ensures that the cameras are synchronised with each other when recording stream data.

Because of the very high transfer rate required by the experiment, the disks must have a certain range of hardware addresses pre-allocated on each disk so that the computer does not waste valuable time searching for free sectors on which to write the data as it arrives at high speed from the RAM buffer. Data storage is achieved by segmenting each frame from each camera into two parts. The top half of each image is written to the first and third physical disks while the read/write heads of the second and fourth disks are positioned ready to write the second half of each image to those disks. While the second and fourth disks are in use, then, the heads of the first and third disks are repositioned to the next addresses in the pre-allocated range, and this process continues until the data ceases streaming. As pre-allocation takes approximately one minute for every 500 frames that are intended to be recorded (per channel), this process required almost 13 minutes for the Bulgarian eclipse (6364 images).

2.7.2.2 Optical guide

An optical bench is used as a mount for all the optical components. In Bulgaria, this was attached to a trestle-form aluminium table using adjustable screws. The aluminium table, in turn, was stabilised by being mounted on wooden sleepers sunk into the ground.

A Meade 20-cm f/10 Schmidt-Cassegrain telescope is mounted at the front of the optical bench, which in turn is fixed to the top of an A-frame support. The height of this optical bench is determined by the position of the Sun and the observing latitude as detailed in §2.7.2.3 below. Light entering the telescope from the front is brought to its prime focus before passing through a collimator lens. The emerging parallel beam continues along the primary optic axis before until it encounters a 1μm mylar beam splitter, angled at 45° to the incident light, which has a $\frac{90\%}{10\%}$ transmission/reflection ratio. The undeflected beam continues along the primary optic axis and passes through the green-line filter, before being focused by a final lens onto Camera 1. This filter's central wavelength can be held constant over a wide temperature range, shifting by only 0.02 Å.K^{-1}. This is made possible because of the filter's refractory oxide coating, treated using an ion-assist deposition system. Meanwhile, the deflected beam continues unfiltered along the secondary optic axis, before focusing onto Camera 2. The entire optical system described was housed in a light-tight wooden box for the Bulgarian eclipse observations to obstruct any extraneous scattered light.

2.7.2.3 Heliostat

The 250 mm-aperture heliostat (Figure 2.13) was designed and built by Dr Paweł Rudawy and colleagues at the Astronomical Institute in Wrocław, and has dimensions 50 cm × 80 cm (pedestal dimensions) × ∼1 m (height). The critical optical component is the 265 mm-diameter mirror *(14)*, manufactured by the Turnow Optical Workshop (Slovakia) from low expansion glass. This mirror is flat to within $\frac{\lambda}{10}$ at 5460 Å and has a coating of Al and SiO, to give a reflection of 89% at the wavelength of the Fe XIV line. The heliostat weighs approximately 90 kg, and this weight helps to keep the system steady, particularly in blustery conditions. Additionally, the bottom of the pedestal *(1)* can be attached to a stable base (wooden blocks sunk into the ground, in the case of the Bulgarian eclipse), to provide further stability. The pedestal itself *(2)* can be tilted to aid adjustment of its orientation to the local horizon. The primary axis is component *(4)*

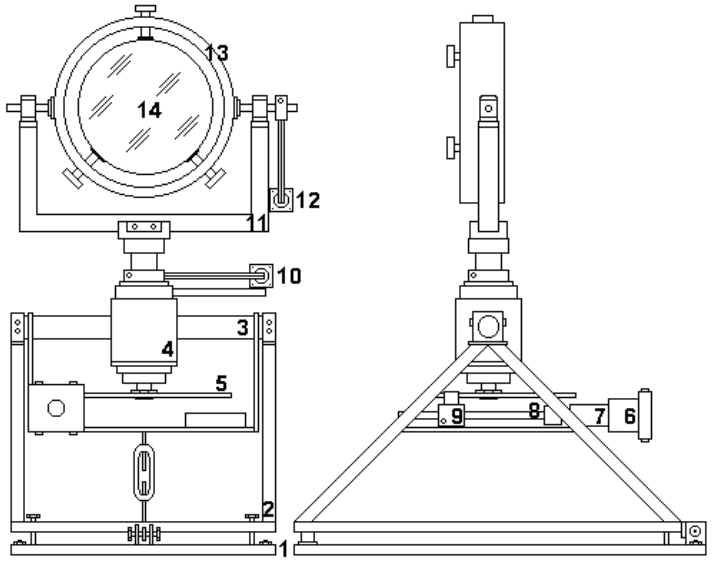

Figure 2.13: Schematic diagram, with front and side views (rotated to the reader's right), describing the heliostat used by SECIS. The numbered components are: 1) Pedestal base; 2) pedestal proper; 3) horizontal axis; 4) main axis unit; 5) driving mechanism disc; 6) diurnal motion stepper motor; 7) planetary gear; 8) power screw; 9) power screw nut; 10) hour angle correction unit; 11) fork; 12) declination correction unit; 13) mirror container; 14) mirror.

in Figure 2.13, and consists of three co-axial steel tubes, connected by high-precision ball bearings, and an externally attached horizontal axis *(3)*, which links the heliostat's rotating fork *(11)* to the pedestal. This main axis unit can be inclined to the pedestal base at a non-normal angle: specifically, an angle equal to the latitude of the observing site so that it allows the mirror to turn in hour angle (or right ascension). At the top of the main axis is the fork unit. The fork carries the mirror container, and therefore bears the mirror, on a horizontal axis which allows the mirror to turn in declination.

The rotation of the mirror is made possible by a 2512 Hz diurnal stepper motor *(6)* (with 1600 steps per revolution), geared down using a three-stage planetary gear *(7)*, with a ratio of 1:256 (giving the additional benefit of a higher torque). The planetary gear transfers power to a screw *(8)*, which in turn drives a screw nut *(9)* and the main drive disc *(5)*. The disc's axis is connected to the middle tube of the main axis unit.

Fine tuning of the position of the solar disc in the field of view is achieved via

a double-joystick, remote box from which the hour-angle *(10)* and declination *(12)* correction units can be adjusted. This it typically performed by first placing a neutral-density filter along the primary beam, and/or a mylar filter over the telescope entrance, and then by adjusting the position of the uneclipsed Sun in the preview 'burst-mode' of either CCD camera. An important point is that, as the position of the mirror is dictated by the geometry of the observing site (latitude of the site, declination of the Sun during eclipse), the height of the mirror from the ground during totality dictates the optimal height of the telescope and, hence, optical bench.

Chapter 3

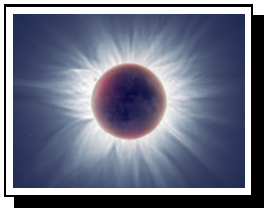

Opacity Effects in the Transition Region of Cool Stars

*In this chapter, HST/*GHRS *observations of two late-type stars are presented: the dMe flare star YZ CMi, and the RS CVn binary star Capella. The effect of opacity is investigated in prominent lines of their ultraviolet transition region spectra, and the resulting optical depths can be used to estimate scale lengths for the emission from a flare on YZ CMi, and for the depth of the transition region of Capella.*

3.1 Introduction

In the analysis of emission from the corona and transition region (both of the Sun and of other cool stars), an important simplifying assumption normally used is that the emission is classed as *optically thin, i.e.* all photons created by radiative de-excitation escape the solar atmosphere. Resonant scattering and collisional de-excitation are negligible in a corona where the electron density and appropriate ion density are low, so this approximation is normally justified. The escape probability (§3.1.3) is a helpful concept in determining the effect of resonance scattering on the emergent intensity of a spectral line from a plasma. If the expected intensity of a stellar spectral line is greater than that actually observed (when accurate calibration has been performed), then the escape probability of that line may be less than 1.0. If this is the case, the line is not optically thin and we must find a way to relate the optical depth of the line to the escape probability of the atmosphere at that wavelength. However, in recent years, Schrijver, van den Oord & Mewe (1994; hereafter SVM) and Schrijver *et al.* (1996) have invoked debate by raising a challenge to this assumption.

Jordan (1967) investigated the relative intensities of two lines originating from a common upper level ($2p3s\ ^3P^o_1$ to $2p^2\ ^1D_2$ and $2p^2\ ^3P_1$) in C I, in the solar UV spectrum. She pointed out that the ratio of the intensities of two lines will deviate from that predicted if an optically thin assumption is not valid. This can, of course, be extended to

other line ratios. In the optically thin case, the (energy) intensity ratio of two emission lines from a common upper level k (*i.e.* common electron population) is given by:

$$\frac{I_{ki}}{I_{kj}} = \frac{A_{ki}}{A_{kj}} \frac{\lambda_{kj}}{\lambda_{ki}} \tag{3.1}$$

where A_{ki}, A_{kj} are the spontaneous transition probability of each line, and λ_{ki}, λ_{kj} are the corresponding wavelengths of the emitted photons. In the case of two lines arising from transitions to a common lower level, however, (and assuming statistical equilibrium) the optically thin flux ratio is given simply by the ratio of the collision rates to the upper level. Because the lower level is a common population, this is simply the ratio of the collision *strengths*, Ω_{ij} to each upper level, j. For a given allowed electric dipole transition $i \leftrightarrow j$, this is related to the oscillator strength f_{ij} by the following (Mariska 1992):

$$\Omega_{ij} = \frac{8\pi}{\sqrt{3}} \frac{I_H}{\Delta E_{ij}} g\, \omega_i\, f_{ij} \tag{3.2}$$

where I_H is the ionisation energy of hydrogen, g is the Gaunt factor, ω_i is the statistical weight (*i.e.* degeneracy) of level i and ΔE_{ij} is the energy difference between the levels. In practice, though – as is discussed later – this ratio is modified according to the escape probability in each line.

The SVM challenge to the assumption of optically thin stellar coronae arose because of a peculiar observational result. An anomalous 'hot' component was observed in the emission measure distribution, EM(T) of the stars α Cen (a G2V + K1V binary) and Procyon (α CMi, an F5IV-V binary). The symptom, in the EUV, is the reduction of the observed line-to-continuum ratio. Since most of the dominant emission lines in this range are from Fe ions, the distribution may have been explained by a lower Fe abundance than assumed. However, adjusting such an abundance involves increasing the emission measure at lower temperatures, and does little to improve the overall fit (Schrijver *et al.* 1996).

Schrijver *et al.* (1996, and references therein) list a number of possible causes for

the observed ratio deficit, including: numerous, closely-spaced lines not yet included in spectral simulation codes, merging to form an excess pseudo-continuum; a true, hot component; an optically thick continuum source; and an asymmetric plasma that is optically thick in the strongest emission lines.

In certain, highly active stars, there is a case for a very hot component of emission, *e.g.* AU Mic & Procyon (Schrijver *et al.*1996). SVM suggest, however, that for Procyon and α Cen, true hot components in the atmosphere do not solve the problem, and that the deficiency in the line-to-continuum ratio derives from opacity in the strong iron lines due to resonant scattering.

A counter-argument was proposed by Schmitt, Drake & Stern (1996) which takes neither the classical stance, nor that of Schrijver *et al.* (1994, 1996). Rather, they argue that the discrepancy between Procyon's flux in the range 110 – 140 Å is independent of resonance scattering. They do allow, though, that very active stars may fit the SVM scenario, and exhibit significant opacity which would affect the accuracy of any emission measure estimates.

An important parameter to introduce is the *optical depth*, τ_λ, which relates the emitted intensity I_λ, at a given wavelength λ, to that received at distance z by

$$I_\lambda(z) = I_\lambda(0)\, e^{-\tau_\lambda(z)}. \tag{3.3}$$

Jordan (1977) gives the following relation for the optical depth at line centre, τ_0, due to resonant absorption:

$$\tau_0(L) = 1.2 \times 10^{-14} \lambda f \sqrt{M} \int_{l=0}^{L} \frac{1}{\sqrt{T_e}} \frac{n_{\rm ion}}{n_{\rm el}} \frac{n_{\rm el}}{n_H} \frac{n_H}{n_e} n_e \, {\rm d}l \tag{3.4}$$

where λ is the wavelength in Å, f the oscillator strength of the transition, M the mass of the absorbing ion species in atomic mass units (amu), T_e the electron temperature in K, L the path length in cm, and $n_{\rm ion}, n_{\rm el}, n_H, n_e$ the number density in cm^{-3} of the

ion, element, hydrogen and free electrons respectively. If we assume average values for each of these parameters along the line of sight, l, then this relation is naturally simplified to

$$\tau_0 = 1.2 \times 10^{-14} \lambda f \sqrt{\frac{M}{T_e}} \frac{N_{\rm ion}}{N_{\rm el}} \frac{N_{\rm el}}{N_H} \frac{N_H}{N_e} < n_e > l \tag{3.5}$$

where T_e is assumed to be the formation temperature of the relevant ion, the N values now represent *column density* (in cm^{-2}), l is the path length and $< n_e >$ is the line-of-sight average of the electron density.

Because of the linear dependence of optical depth on wavelength, Schmitt *et al.* (1996) correctly point out that a small departure from the optically thin approximation at X-ray wavelengths implies more significant opacity in the EUV range. We might therefore expect that in a denser medium, such as the transition region, where the emission is predominantly in the ultraviolet, strong lines would exhibit opacity signatures. Doyle & McWhirter (1980; hereafter DMW) and Keenan & Kingston (1986; KK) investigated the effect of opacity in transition region lines of C III and Si III, respectively, in the solar atmosphere near the observed limb where the line-of-sight path length is greatest. In certain lines, they found evidence of optical depths of order unity, hinting that opacity effects may indeed be important in cool stellar atmospheres. The path length is a useful physical parameter to know for a stellar emitting region. If we know the path length of the emitting region – such as a stellar active region – then we instantly have an order-of-magnitude figure for its physical scale. Of course, this requires us to know the electron density, n_e of the region, which may be derived from a combination of linear emission measures with column densities (Phillips *et al.* 1996):

$$\tau = \frac{3.11 \times 10^{-13} \frac{N_{\rm ion}}{N_{\rm el}}}{\sqrt{\frac{2kT_e}{M} + \xi^2}} \int n_e \, dl \tag{3.6}$$

where ξ is the micro-turbulence velocity in the local atmosphere, and the $2kT_e/M$ term represents the thermal Doppler broadening of the line profile. Alternatively, the local density, n_e may be inferred from density-sensitive line ratios (*e.g.* Schmitt *et al.* (1996),

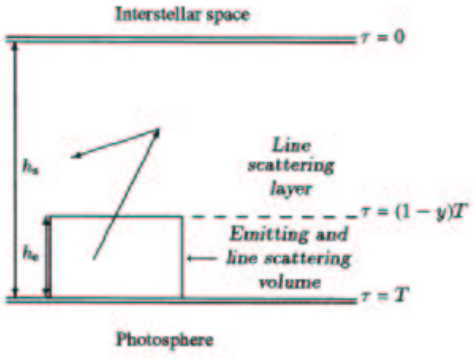

Figure 3.1: Geometry of inhomogeneous scattering from Schrijver, van den Oord & Mewe (1994).

Dere *et al.* (1997)) as per DMW and KK; or from a combination of linear emission measures with column densities $n_e l$ (Phillips *et al.* 1996). One can therefore calculate all other parameters to derive l.

3.1.1 Geometric effects on opacity

If a given line has a significant oscillator strength, then it cannot be thought of as optically thin since it will suffer non-negligible attenuation during its passage through the absorbing plasma. The geometry of the emitting and scattering areas is important, though: since the dominant process is resonant scattering, not photon destruction, these scattered photons must be re-emitted in another direction. In an homogeneous atmosphere, the amount of resonant scattering out of the line of sight would be balanced by the resonant scattering of photons into the line of sight. Opacity by scattering would therefore go undetected. However, if the emitting region is smaller than the scattering region, then it follows that the intensity of an optically thick line will be reduced. Figure 3.1, taken from SVM, illustrates this. This inhomogeneity has a particularly relevant application to active regions (Schmelz *et al.* 1997). If the line of sight from the emitting region, such as an active region, passes through an associated set of nested coronal loops – which constituting a scattering volume – then the intensity of an opti-

Table 3.1: The line transitions used in the present study.

Ion	Wavelength (Å)	Transition	Oscillator Strength
Si IV	(1393.76)	$3s\ ^2S_{1/2} - 3p\ ^2P_{3/2}$	0.52 [1]
Si IV	(1402.77)	$3s\ ^2S_{1/2} - 3p\ ^2P_{1/2}$	0.26 [1]
C IV	(1548.20)	$2s\ ^2S_{1/2} - 2p\ ^2P_{3/2}$	0.20 [2]
C IV	(1550.77)	$2s\ ^2S_{1/2} - 2p\ ^2P_{1/2}$	0.10 [2]

[1] Oscillator strengths from Maniak et al. (1993)

[2] Oscillator strengths from Wiese et al. (1966)

cally thick line will be reduced.

Study has also been carried out into the solar case of the variation of coronal opacity with position on the solar disc, to conclusions which were recently at odds (Phillips *et al.* 1996; Saba *et al.* 1997). Phillips *et al.* (1996) appear to find that the scattering is greatest at disc centre and that scattering decreases almost linearly (*i.e.* $\frac{dR}{d\theta} \sim$ constant), with heliocentric distance, θ, where R is the ratio of the observed flux of an optically thick line to the expected flux. This is in contrast to findings from the same data (Schmelz *et al.* 1997; Saba *et al.* 1999) which indicate that the scattering in fact *increases* with heliocentric distance.

One of the strongest pairs of lines in the UV spectrum of the transition region is the resonance line doublet of C IV. These lines are formed from transitions to the $2s\ ^2S_{\frac{1}{2}}$ ground state from the excited $2p\ ^2P_{\frac{1}{2},\frac{3}{2}}$ states which are separated by fine structure. However, the lines have significantly different oscillator strengths (Table 3.1). In this doublet, the stronger of the lines (hereafter referred to as *resonance*) has an oscillator strength which is double that of the weaker (*reference*) line. The lines are predominantly formed at a temperature of 10^5 K, which corresponds to the upper transition region of the Sun. A similar pair of lines is formed by Si IV at a slightly lower temperature (6×10^4 K), *i.e.* somewhat lower in the transition region. However, since the temperature gradient in this part of the atmosphere is extremely steep (*see Introduction Chapter*), the physical separation of the C IV and Si IV emitting regions is negligible, partic-

ularly when compared to the range of temperatures in which they overlap. Importantly, these lines show no density dependence over the range $10^6 < n_e < 10^{14}$ cm^{-2}, a range much larger than that analysed in the solar transition region ($5 \times 10^8 < n_e < 10^{10}$ cm^{-2}).

3.1.2 Line ratios and escape probabilities

In an optically thin scenario, the ratio of the resonance and reference intensities will be the ratio of the oscillator strengths. From Schmelz *et al.* (1997):

$$\frac{F_{res}}{F_{ref}} = P_e \frac{\Omega_{res}}{\Omega_{ref}} \tag{3.7}$$

where F_{ref} & F_{res} are the fluxes of the resonance (optically thick) line and the reference line respectively. Hence the ratio of the line intensities from a common upper level is the same as the ratio of their respective oscillator strengths, provided that we are dealing with and optically thin case. In an optically thick case, however, this ratio is modified by the *ratio* of the escape probabilities (Kastner & Kastner 1999), since the optical depth in a given line is a function of the oscillator strength; *i.e.*

$$\frac{F_{res}}{F_{ref}} = \frac{P_{res}}{P_{ref}} \frac{\Omega_{res}}{\Omega_{ref}} \tag{3.8}$$

where P_{res} and P_{ref} are the escape probabilities for the respective lines.

3.1.3 Calculation of escape probability

P_e is rigorously calculated by Athay (1972), but Kastner & Kastner (1990) numerically calculated the escape probability from the optical depth using equation 3.9 for $10^{-3} < \tau_0 < 10^5$, for the cases of homogeneous and inhomogeneous distribution (the latter in their Table 1) of emitters and absorbers. They use a parameter q to define the degree of homogeneity. It is defined such that $q = 1$ desribes a uniform distrubution of absorbers

amongst emitters, whereas $q = 0$ for a plasma where the emitting and absorbing regions are spatially removed from one another. For an inhomogeneous mixture ($q = 0$), P_e is given by:

$$P_{e,\mathrm{inhom}}(\tau_0) = \frac{1}{\tau_0\sqrt{\pi}} \int_{-\infty}^{\infty} \exp(-x^2 - \tau_0 e^{-x^2})\, \mathrm{d}x \tag{3.9}$$

where τ_0 is the optical depth at line centre, x the dimensionless frequency variable $x = \frac{\nu-\nu_0}{\Delta\nu_D}$ and $\Delta\nu_D$ the half-width, at half-maximum, of the thermal Doppler line profile. They also give the numerical solution to this as:

$$P_{e,\mathrm{inhom}}(\tau_0) = 1 + \sum_{i=1}^{\infty} (-1)^n \, \tau_0^n \, \frac{1}{n!\sqrt{n+1}} \tag{3.10}$$

Since we know that the ratio of the lines' optical depths must be 2:1, and since the lines in question are separated by only a few angstroms, we can use Kastner & Kastner's calculations to deduce τ_0 from the line flux ratio and the ratio of the escape probabilities (see figure 3.2).

3.1.4 Applicability to stellar sources

Schmitt *et al.* (1996) imply that active stars may exhibit EUV opacity signatures (§3.1). Because stellar sources are unresolved point sources from Earth, studies such as those by KK and DMW are not viable. It is only possible to examine line ratios, without necessarily knowing where on the stellar disc these photons are formed. Very active stars demonstrate strong chromospheric lines in *emission* rather than absorption (the latter being the case on the Sun), and are of spectral type F and later. Dwarf M (dM) stars which are sufficiently active that the chromospheric Hα and Ca II H & K lines appear in emission are labelled dMe. These stars represent candidates for demonstrating opacity in strong lines in their atmospheres. Also active, often with extended coronae, are the ageing main-sequence RS CVn (RS Canum Venaticorum) type stars. These

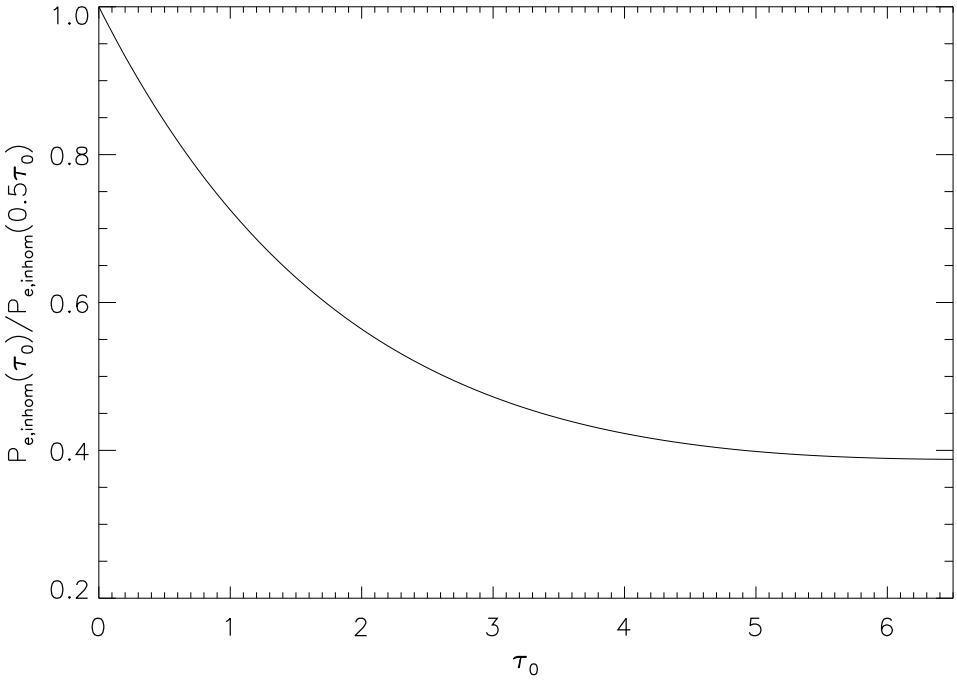

Figure 3.2: The ratio of escape probabilities, for the lines of each doublet, as a function of optical depth for an inhomogeneous distribution of emitters and absorbers, as calculated by Kastner & Kastner (1990). Note that this is the ratio of the escape probabilities of the reference line to the resonance line, *i.e.* $P(\tau_0)/P(0.5\tau)$.

tidally-locked binaries typically have fast rotation (and therefore orbital) rates, of the order of only days. Consequently, they are highly active stars, consistent with the initial findings of Wilson (1966), then Mathioudakis *et al.* (1995), viz. that faster rotation rates in late-type stars largely correspond to higher levels of chromospheric and coronal activity.

Since late-type stellar sources are known to exhibit solar-like atmospheres (Linsky *et al.* 1995; Phillips 1992), it is reasonable to unify the work on the solar limb in C III and Si III with the opacity work in the EUV emission of cool stars. In this chapter, we analyse the C IV and Si IV emission of the transition region in two known active stars: the dMe flare star, YZ CMi (of type BY Dra); and the nearby RS CVn binary, Capella.

The choice of YZ CMi and Capella reflects a test of the opacity hypothesis in two situations. YZ CMi is a dwarf star of spectral type M4.5Ve, and is therefore chromospherically active. It is also a known flare star, and hence produces events in which

enhancements of density and temperature occur (Chapter 4). Such localised enhancements in density introduce a greater inhomogeneity in the emitting/scattering region, such as that shown in Figure 3.1, and we would expect enhanced opacity effects to be evident. Sylwester *et al.* (1986) have already achieved such a detection in the Soft X-ray emission of Mg XII (4.5×10^6 K) at λ8.42 Å, during a solar flare. Detectable stellar flares are typically much more energetic; thus, one might expect that – by this simple selection effect – opacity effects on emission lines in observed stellar flares are more important still than those in solar flares.

It is of interest to see whether an active, non-flaring star will exhibit opacity, and for this reason we choose our RS CVn star. Capella is a binary system composed of a G8III star and its G1III companion. The G1III star has the larger $v \sin i$ (line-of-sight rotational velocity) than its companion, and is consequently the more active star (Mathioudakis *et al.* 1995). Doppler shifts in the emission wavelength of the resonance doublets of C IV (λ1548 & λ1551 Å) and Si IV (λ1394 & λ1403 Å) are consistent with $v \sin i$ of the hotter G1 star, implying that the bulk of this emission is from that star; although the same is not true of the X-ray flux (Linsky *et al.* 1998).

3.2 Method

3.2.1 Observations

In order to find data applicable to our study, we trawled the *HST* Public Data Archive. We find two appropriate GHRS (§2.2) datasets for Capella, taken in April 1991 and April 1996 with the G160M and G140M gratings ($\frac{\lambda}{\Delta\lambda} \approx 20\,000$), respectively; and two, more extensive datasets for YZ CMi, taken in December 1994 and April 1996 with the G140L grating ($\frac{\lambda}{\Delta\lambda} \approx 2000$). Table 3.2 gives the details of these data.

The three, higher resolution datasets for Capella consist of one spectrum including the C IV resonance doublet, and two including the Si IV doublet with nearby lines of

Table 3.2: Details of the GHRS datasets used for YZ CMi and Capella (α Aur).

Resonance Doublet Studied	Dataset Name	λ_{start} (Å)	λ_{start} (Å)	Exposure Time (s)	Start Time (U.T.)	
Capella						
Si IV	z0jr010ct	1532	1567	163.20	1991-Apr-15	05:32:55
C IV	z0jr010dt	1384	1420	380.80		05:37:18
Si IV	z2uw0305t	1390	1418	4125.00	1996-Apr-09	19:16:04
YZ CMi						
Si IV	z2lm0104t	1150	1436	2535.28	1994-Dec-21	06:31:54
Si IV	z2lm0106t	1150	1436	2555.28		08:08:06
Si IV	z2lm0108t	1150	1436	2563.28		09:44:30
Si IV	z2lm010at	1150	1436	2557.28		11:21:06
Si IV	z2lm010ct	1150	1436	2562.03		12:57:30
Si IV	z2lm010et	1150	1436	2564.03		14:34:00
Si IV	z2lm010gt	1150	1436	2566.03		16:10:30
Si IV	z2lm010it	1150	1436	2561.28		17:47:06
Si IV	z2lm010kt	1150	1436	2505.28		19:23:54
Si IV	z2lm010mt	1150	1436	2206.03		21:06:36
Si IV	z2lm010ot	1150	1436	1845.15		22:48:55
Si IV & C IV	z2yv0304t	1377	1663	2648.00	1996-Apr-18	05:46:13
Si IV & C IV	z2yv0306t	1377	1663	2647.00		07:22:13
Si IV & C IV	z2yv0308t	1377	1663	2647.00		08:58:43
Si IV & C IV	z2yv030at	1377	1663	2648.00		10:35:13
Si IV & C IV	z2yv030ct	1377	1663	2617.00		12:11:03

O IV, whose ratio is an indicator of density. For our purposes, the 1994 data of YZ CMi include only the Si IV doublet, and are taken over the course of almost one full day. The 1996 data, on the other hand, are taken over the course of just over six hours, but include both resonance line pairs. The fact that many more hours' observations were taken of YZ CMi reflects the fact that this is a highly active flare star, with frequent flare activity.

3.2.2 Reduction

The data were downloaded from the *HST* online archive in ASCII text format, and analysed using the DIPSO programme available as part of the STARLINK software group. DIPSO is designed as a spectrum analysis suite, and is therefore well-suited to reduction of 1-dimensional spectra. Specifically, the Emission Line Fitting (ELF) facility was

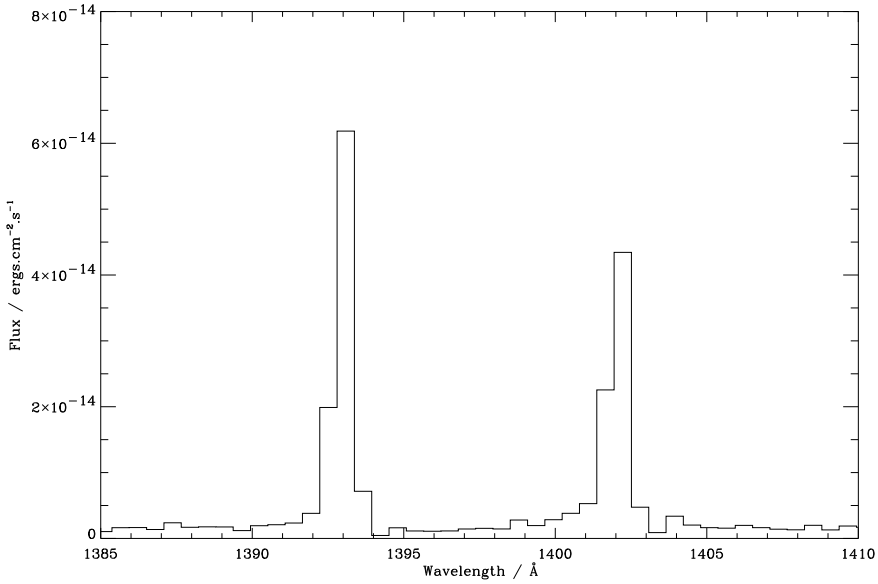

Figure 3.3: GHRS spectrum of YZ CMi in the wavelength region of Si IV, during the flare observed in 1994 April. The O IV lines used to determine electron densities are noted with vertical dashed lines.

used to fit the Gaussian profiles of the emission lines shown in Figures 3.3 and 3.4. ELF returns a fit to each line, by an iterative method, based on either approximate, exact or relative initial-guess parameters. The results can be stored in memory and saved, and take the form of central wavelength, full width at half maximum (FWHM), peak flux (*e.g.* in erg cm^{-2} $s^{-1}Å^{-1}$) and integrated line flux (*e.g.* in erg cm^{-2} s^{-1}). Each of these parameters is also returned with errors to 68% confidence (*i.e.* 1σ errors) and these are appropriately combined in §3.3 to yield 1σ errors for the flux ratio and therefore τ_0. We assume that the errors in the escape probability ratio are entirely due to errors in the line flux, and neglect errors in the oscillator strengths.

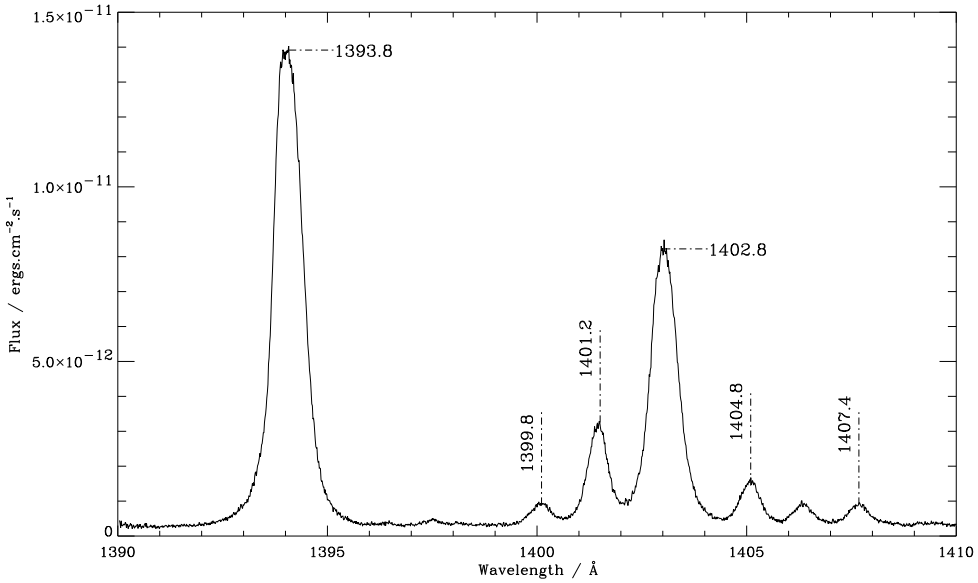

Figure 3.4: GHRS spectrum of Capella in the wavelength region of Si IV. The O IV lines used to determine electron densities are noted with vertical dashed lines.

Table 3.3: Line fluxes and ratios of the Si IV multiplet for YZ CMi and Capella. The fluxes are given in units of 10^{-14} erg cm^{-2} s^{-1} followed by the estimated error in brackets. Note that the quiescent fluxes have been subtracted from the flare.

Ion λ (Å)	Si IV 1393.8	Si IV 1402.8	Ratio	$\tau_{1393.8}$	C IV 1548.2	C IV 1550.8	Ratio	$\tau_{1548.2}$
YZ CMi								
Quiescent 1994	3.9 ± 0.07	2.1 ± 0.06	1.86 ± 0.08	$0.23^{+0.13}_{-0.12}$	–	–	–	–
Flare 1994	4.2 ± 0.18	3.6 ± 0.17	1.17 ± 0.11	$1.87^{+0.48}_{-0.38}$	–	–	–	–
Quiescent 1996	5.2 ± 0.15	2.9 ± 0.13	1.79 ± 0.13	$0.35^{+0.23}_{-0.21}$	20.0 ± 0.68	11.0 ± 0.6	1.82 ± 0.16	$0.28^{+0.28}_{-0.25}$
Flare 1996	19.0 ± 0.64	13.0 ± 0.60	1.45 ± 0.11	$1.03^{+0.28}_{-0.25}$	46.0 ± 2.1	29.0 ± 1.9	1.57 ± 0.17	$0.74^{+0.39}_{-0.32}$
Capella								
April 1991	$1.2 \times 10^3 \pm 8.29$	$7.0 \times 10^2 \pm 7.5$	1.71 ± 0.03	$0.49^{+0.06}_{-0.05}$	$2.8 \times 10^3 \pm 2.4 \times 10^2$	$1.6 \times 10^3 \pm 228.2$	1.74 ± 0.04	$0.42^{+0.07}_{-0.07}$
April 1996	$1.2 \times 10^3 \pm 5.23$	$6.5 \times 10^2 \pm 4.5$	1.83 ± 0.01	$0.28^{+0.02}_{-0.02}$	–	–	–	–

3.3 Results & Discussion

We assume here that these deviations in the line ratios are due to opacity, and that the absorbing and emitting regions are spatially separated. The latter assumption is an extreme case, and is unlikely to accurately reflect the true distribution of emitting and absorbing ions. However, using this limit where the inhomgeneity index $q = 0$ (§3.1.3), we can find a lower limit to the path lengths involved. From equation 3.8, the quotient of the observed and theoretical line ratios should yield the escape probabilities' ratio. Table 3.3 lists the calculated line fluxes, flux ratios and resultant optical depths in our chosen doublets, for both Capella and YZ CMi. Also indicated are the 1σ errors in these parameters. Since the gradient of $P_{\mathrm{e,inhom}}(\tau_0)/P_{\mathrm{e,inhom}}(0.5\tau_0)$ decreases with increasing τ_0, one would expect the errors in τ_0 to be asymmetric with a positive bias. This is indeed found to be the case for all optical depths, with the minor exception of two of the Capella depths – C IV in 1991 April; and Si IV in 1996 April – where the errors are identical to the second decimal place.

The line ratios listed in Table 3.3 indicate detectable opacity in the transition region of both stars. Two points are noteworthy in the case of YZ CMi: that the line ratio drops dramatically during the flare periods, demonstrating a line-centre optical depth of up to 1.85; and that during the quiescent phases, the line ratio still shows a marginal deviation from the 2:1 ratio. In the case of Capella, there is marked deviation from this optically thin limit in both datasets.

Line-of-sight path lengths for the Capella observations are calculated using the density-sensitive intersystem lines of O IV. The line ratios used are:

$$\frac{1399.78\ \text{Å}\ \left(2s^2\ 2p\ {}^2P_{\frac{1}{2}} \leftrightarrow 2s\ 2p^2\ {}^4P_{\frac{3}{2}}\right)}{1404.81\ \text{Å}\ \left(2s^2\ 2p\ {}^2P_{\frac{3}{2}} \leftrightarrow 2s\ 2p^2\ {}^4P_{\frac{3}{2}}\right)} \tag{3.11}$$

(Figure 3.6a); and

$$\frac{1407.43\ \text{Å}\ \left(2s^2\ 2p\ {}^2P_{\frac{3}{2}} \leftrightarrow 2s\ 2p^2\ {}^4P_{\frac{1}{2}}\right)}{1404.81\ \text{Å}} \tag{3.12}$$

(Figure 3.6b). The derived densities are $n_e \approx 10^{10}$ cm^{-3} in both Capella observations, with the values of log n_e agreeing to within 0.3.

Since there are no suitable density-sensitive line ratios present in the YZ CMi datasets, we estimate the density from the emission measure (EM). We apply this method to the April 1996 dataset by determining the best fit of a density-sensitive line to an existing emission measure (van den Oord *et al.* 1996). As we use lines of several elements in this procedure, our estimated values of density are are likely to be affected by abundance and/or ionisation equilibrium uncertainties. We use the observed flux of the O IV intersystem line at 1401.2 Å (logT=5.2). The best agreement between the EM and the O IV (1401.2 Å) line flux is obtained for $n_e = 10^{11.5}$ cm^{-3}.

Determination of the path length can then be carried out by inserting the correct values into the parameters of equation 3.5. We take our ionisation fraction values of the from Arnaud & Rothenflug (1985).The temperature of maximum formation of Si IV is log $T_{\rm Si\,IV}$ = 4.8; at this temperature, $\frac{n_{\rm SiIV}}{n_{\rm Si}} = 0.35$ (Arnaud & Rothenflug 1985) and $\frac{n_{\rm Si}}{n_{\rm H}} = 1.3 \times 10^{-4}$ (Feldman 1992). Using $M_{\rm Si} = 28.1$, and our estimate of $n_e = 10^{10}$ cm^{-3} for Capella, we derive a path length of $\sim$75 km. In the same fashion for YZ CMi, we find a path length value of $\sim$5 km. The derived path lengths are in very good agreement with the semi-empirical modelling of Houdebine & Doyle (1994), who concluded that the observed line profiles of an active stellar atmosphere can only be reproduced if the transition region is very thin and at a high column mass.

3.4 Conclusions

A widely used assumption in the study of stellar transition regions and coronae, is that the emission is optically thin. We have presented strong evidence for opacity effects in the transition regions of the dMe star YZ CMi and the RS CVn binary Capella. The line ratios presented deviate appreciably from the optically thin approximation.

The method employed used here is shown to be simple but powerful. The Capella observations permit the electron density to be estimated from density–sensitive O IV lines, and a line-of-sight path length of $\sim$75 km in the transition region is derived. In the case of YZ CMi, no such lines are present, but an estimate of the density is made based on the emission measure using the O IV intersystem line at 1401.2 Å, yielding a transition region path length of $\sim$5 km. In this way, opacity can be used as a powerful diagnostic to determine linear dimensions in upper stellar atmospheres.

Observations of cool stars are crucial in understanding the history of the Sun. Younger, highly active stars can reveal important information about the earlier development of the solar surface and atmosphere, while older stars are less active than our own, and may tell us something about the Sun's behaviour in the distant future. What we lack, however, is information on the positions and morphology of emitting regions in stellar atmospheres. This information is abundant in data taken from the spatially resolved Sun. In the following remainder of this thesis, investigations are made into two primary forms of activity in solar active regions, each of which may make a significant contribution to the high temperature of stellar coronae.

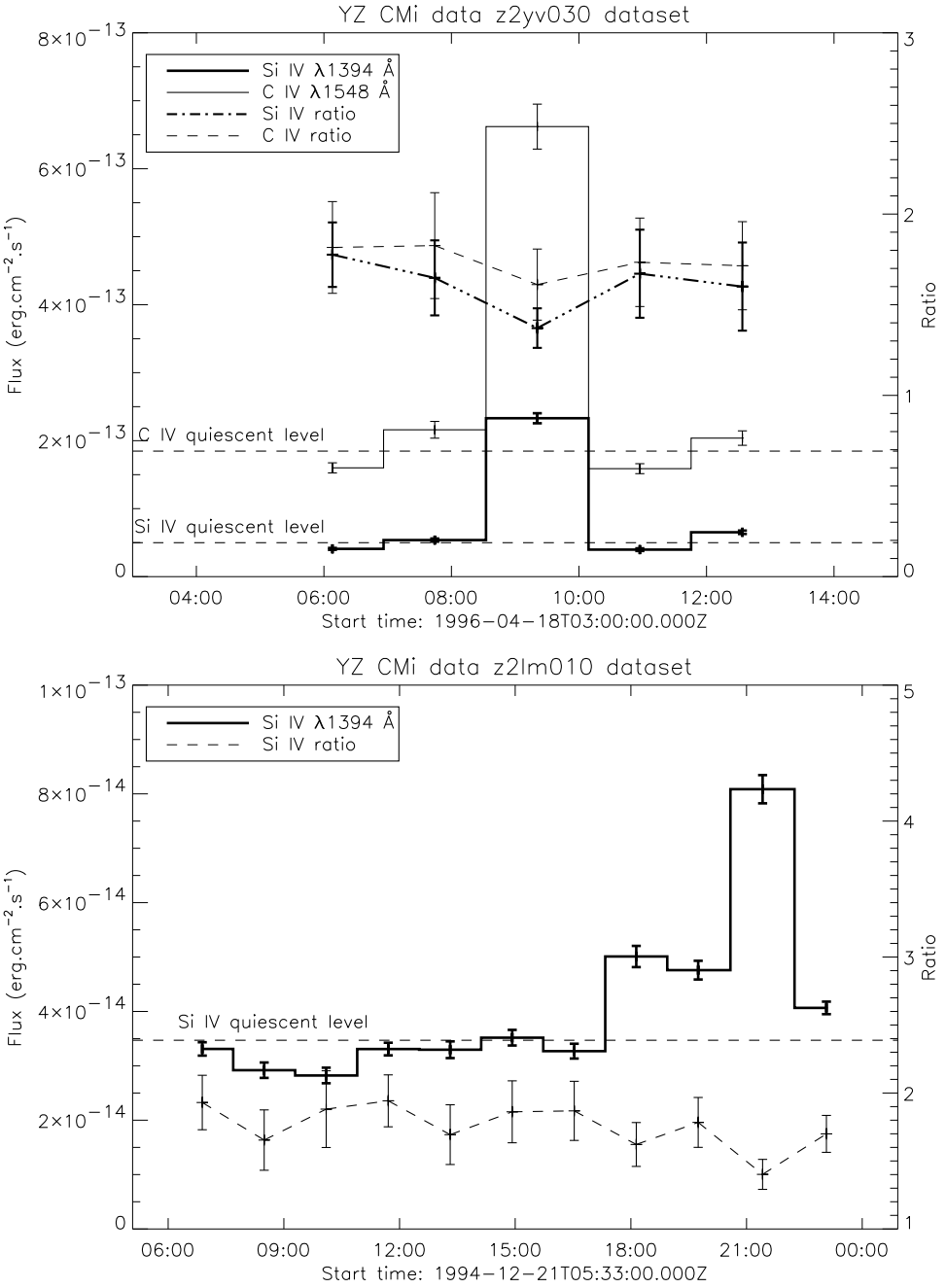

Figure 3.5: Lightcurve data for both flares observed on YZ CMi. Ratios between the resonance lines are also included on each plot. Histogram plots indicate flux levels for each line; broken lines connect points denoting the ration of the stronger resonance doublet line to the weaker line, *e.g.* Si IV Ratio = $F(\lambda 1394)/F(\lambda 1403)$. Ratio values are plotted in all cases with reference to the right-hand vertical axis.

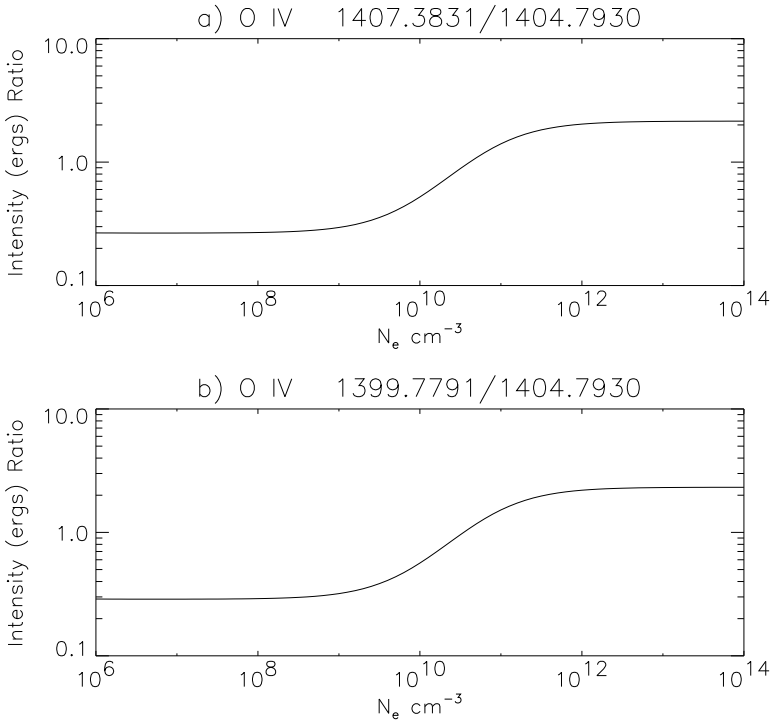

Figure 3.6: Density-sensitive line ratios, as calculated by CHIANTI (Dere *et al.* 1997) used to calculate the electron density in the Si IV-emitting region of Capella.

Chapter 4

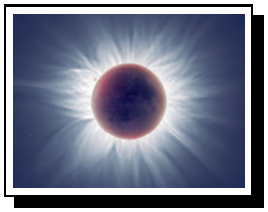

Multi-wavelength observations of a class C5.2 solar flare

In this chapter, we deal with broad-spectrum observations of a three-component, C5.2-class flare. Despite its modest X-ray energy release, the flare releases a large portion of its energy in the form of non-thermal kinetic motions characteristic – in this case – of a flare 'spray' event. The goal of the observations was to track the progress of a flare through the solar atmosphere in wavelength from the optical (using the NSO/Dunn Solar Telescope), through the UV and EUV (recorded with the TRACE observatory), to X-ray wavelengths (with the GOES-8 and CRGO spacecraft). The observations are analysed in terms of the morphology of the flare and the material it ejects, as well as the relative enhancements in emitted flux during its complex evolution.

4.1 Introduction

With the advent of the NASA *Transition Region And Coronal Explorer* (*TRACE*) mission, in 1998, came the ability to image the UV/EUV Sun with a resolution comparable to that of ground-based visible-light observatories, and so close the gap in our understanding of the relationship between the solar chromosphere, transition region and corona. Just as it is becoming recognised that the development of an accurate picture of coronal heating relies on the coupling of the corona, transition region and chromosphere (Aschwanden 2001), so too there is interest in the behaviour and interactions of the various parts of the solar atmosphere during solar flares, not least in their highly efficient mechanism(s) of particle acceleration.

4.1.1 Flare models

In the currently-held picture of flare evolution, the magnetic field above an active region reconfigures itself to a lower energy state, thereby releasing the magnetic energy which

has been stored there.Several models exist to explain the observed detail in the flare mechanism, and any credible model must explain the high temperatures and densities observed, as well as the time profile of emission in each portion of the electromagnetic spectrum.The *helmet-streamer*-like configuration proposed in Sturrock's model (1968), and expanded by Kopp & Pneuman (1976), envisages a Y-shaped (or *Y-type*) neutral point at the interface between closed magnetic field lines and open lines rooted further away from the active region's surface neutral line and, thus, the sub-photospheric dipole at the cause of the field. Sweet (1958) considered the interaction of *two* bipolar regions whose mutual approach would generate a current sheet out of the prior location of an X-type neutral point. Concurrent with this is the rising of the outer field lines, but no reconnection of magnetic field lines is involved. Work by Priest and Raadu (1975) and Heyvaerts *et al.* (1977) extended this model to show that magnetic reconnection would in fact take place, driving the plasma above the reconnection site higher into the atmosphere. These models predict acceleration of particles along the magnetic field in both the upward and downward directions as the magnetic field relaxes from reconnection.

Syrovatsky (1966) then investigated a slightly different picture of current sheet formation in an X-type configuration, with a more generic *single* dipole field (much more characteristic of flaring regions). In his model, the X-type neutral point again collapses to form a current sheet, but in the absence of reconnection, the plasma is heated by the onset of ion sound turbulence, inducing heating sufficient to produce thermal SXR emission. The resulting current – with charged particles at relativistic drift velocities – then constitutes a source of high energy particles with HXR and radio (burst) emission generated as a side effect.

However, since no two flares are exactly alike, these models can only hope to obtain first-order accuracy in describing the physical processes which take place. There is also the distinction between so-called *two-ribbon* (or *dynamic*) flares, more commonly associated with prominences (known as *filaments* on the disc), and *simple-loop* (or *compact*)

flares involving instability in a loop either due to thermal non-equilibrium or initiated by an emerging magnetic flux tube from deeper in the solar atmosphere. Nevertheless, a consensus prevails on the nature of these processes, moderated by MHD analysis and a vast array of data taken during observations of flares both in the visible spectrum – particularly in Hα, *e.g*. Temmer *et al.* (2001) – and latterly in radio/microwave, X-ray and ultraviolet observations.

4.1.2 Two-ribbon flares

A normal precursor to a two-ribbon flare – such as that discussed in this chapter – is the rise of a prominence through the atmosphere (Švestka 1981). Prominences normally lie above the magnetic inversion line between regions where the magnetic field vector normal to the surface is upward (positive) and downward (negative); they are a good proxy for this line in the absence of photospheric line-of-sight field component ($B_{||}$) measurements, although not all inversion lines are traced out by prominences. These structures appear as dark *filaments* on the solar disc since they are relatively cool absorption features: they are most easily viewed against the Hα emission of the chromosphere. The prominence rise can normally be described in two stages: a slow initial rise followed by a fast ascent through the atmosphere as the filament 'erupts' and the flare begins.

Reconnection in this scenario is thought to happen as follows (Priest 1981). The filament begins to rise (pre-flare, slow rise). This can be because of either thermal non-equilibrium in the filament or the emergence of a new dipole of magnetic flux below the original system. An eruptive instability is then encountered as: i) a magnetic flux tube emerges from below the original loop system; ii) the rising magnetic field around the filament becomes magnetically unstable; or iii) a current sheet forms allowing reconnections to take place in the $B_{||} = 0$ plane which it defines. As the prominence rises, it opens the field lines around it (Figure 4.1), and the field lines below the filament then reconnect to fill the magnetic 'void' left in its wake (Priest & Forbes 1990).

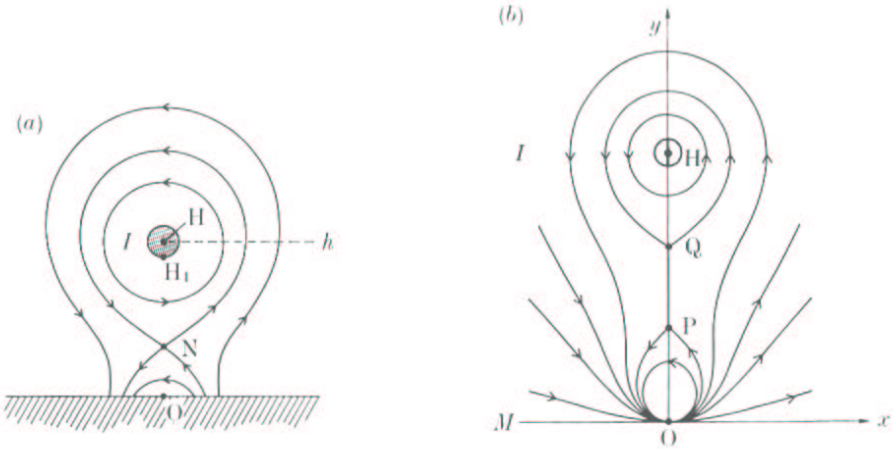

Figure 4.1: Cross-section of the field configuration around a prominence/filament: a) a prominence is initially supported above the $B_{||} = 0$ neutral line, and lies above an X-type neutral point, *N*; b) collapse of the neutral point to form a current sheet *PQ*, and the eruption of the prominence and opening of the ambient field lines as the prominence rises.

These loops appear to rise with the filament, although always underneath it, and drive the eruption of the filament higher into the atmosphere. This is in fact a consequence of progressively higher reconnections of field lines in the atmosphere (Figure 4.2), rather than of the expansion of individual loops.

The observations of hard X-ray (HXR) emission which are normally seen at flare onset mark the acceleration of plasma particles to very high energies from the reconnection site. Although the precise mechanism of acceleration is still the subject of much discussion (§4.1.1), it is known that these particles are driven both downward and upward (radially outward) along field lines to which the high-conductivity plasma is 'frozen'. The upward-accelerated particles often attain relativistic speeds; they can sometimes be detected by near-Earth space environment satellites within an hour of the initial flare reconnection. Meanwhile, the downward high-energy particles soon encounter the progressively much denser transition region and chromosphere, and emit *brehmsstrahlung* in the HXR range as they are slowed down by collisions with this material. At the other end of the spectrum, they also emit at radio wavelengths by gyrosynchrotron emission, as they spiral around the magnetic field lines to which they are

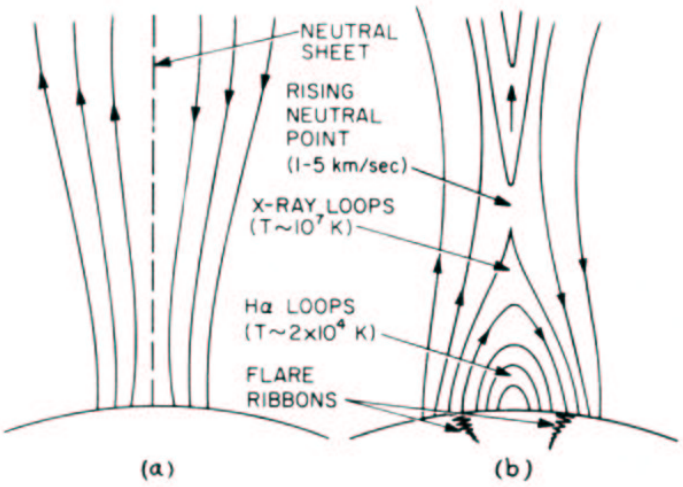

Figure 4.2: Schematic of the reconnection scenario and formation of post-flare loops in a two ribbon flare, taken from Pneuman (1981). The cartoon shows a) the neutral current sheet left between the open field lines of opposite polarity after the eruption of the prominence; b) the formation of the ribbons at the footpoints of newly forming post-flare loops which reconnect the open field lines in the wake of the eruption.

tied, with frequency, ν, given by

$$\nu = \frac{qB}{2\pi m}\left[1 - \frac{v^2}{c^2}\right]^{\frac{1}{2}}. \tag{4.1}$$

Substituting values for the electron charge (q) and mass (m), and assuming a field, B of several hundred gauss near the loop footpoint, with mildly relativistic velocities v, this gives a gyrofrequency of the order of GHz, *i.e.*, emission in the microwave régime.

The rapid emission phase at HXR and radio wavelengths is referred to as the *impulsive phase*, since the particles responsible are at non-Maxwellian energies. The *thick-target* picture described above leads to a second consequence of the flare, which is responsible for the emission seen in the optical, UV and EUV ranges. As the flare continues, what is known as the *main phase* takes over. Emission is now termed *thermal*, *i.e.* it is dominated by radiative cooling of the plasma contained in the loop.

The denser material, which caused the retardation of the incoming particles, naturally receives a great deal of thermal energy and experiences a vast rise in kinetic pressure. Since the pressure lower in the atmosphere is greater (Figure 1.4), the ma-

terial preferentially expands upwards; it is still tied to the magnetic field lines, and expands up along the magnetic threads of the loop, filling the loop with hot material with temperatures of anything up to $\sim 10^7$ K. As a result, the loop appears to brighten in soft X-rays as it cools by radiation. The neighbouring EUV region of the spectrum also brightens, and instruments such as *TRACE* record enhancements in emission from ions as hot as Fe XV ($T \sim 2 \times 10^6$ K – lower corona) at 284 Å down to the 1550 Å UV resonance doublet of C IV ($T \sim 10^4$ K – transition region).

The loops which form in this way, below the eruptive prominence, are known as *flare* or *post-flare* loops (PFLs). They continue to form at greater heights (*i.e.* higher reconnections of open field lines occur), and their footpoints are found further and further apart. At the footpoints, the material becomes evaporated by fresh sources of high-energy particles released by the new, higher reconnections. Footpoints of higher-lying loops are found further apart, and the locations of the ribbon-like brightenings in Hα therefore move further outwards (Kopp & Poletto 1984). A qualifier to this trend is that, if the mutually separating ribbons encounter sunspots – where the outward field strength is much higher – the footpoints of steadily higher loops tend to remain in the same place, simply due to the local concentration of magnetic field lines. As a result, the ribbons appears to 'freeze' at sunspot penumbrae, while the loops continue to form with greater heights only. Loops which are lower down, and therefore less recently formed, have thus cooled for longer, and eventually become visible in the much cooler Hα line. Such Hα loops are necessarily always visible within the boundaries defined by the two outwardly moving ribbons (Figure 4.2b).

4.1.3 Flare spray events

Along with eruptive prominences, two other (sometimes less distinct) types of dynamic events are often features of solar flares. These are the *spray* and *surge* events. A surge event occurs when material is ejected with a vertical velocity component which is

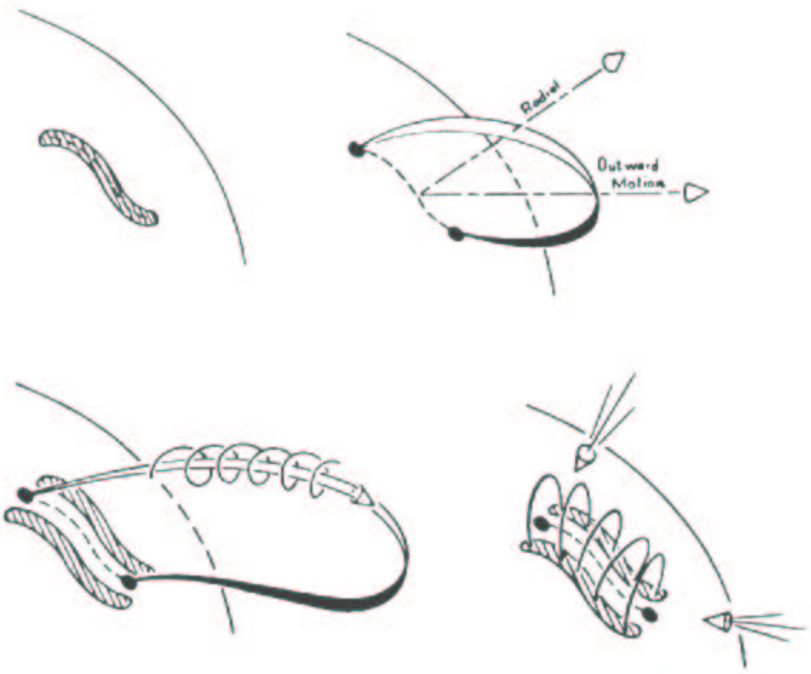

Figure 4.3: Schematic of the expansion of a flux tube during a flare spray event, from Tandberg-Hanssen *et al.* (1980). The initial filament (top-left), supported above the neutral line, becomes activated and expands in an unstable fashion (top-right), deforming and rising into the upper solar atmosphere. Material trapped in the tube expands with the magnetic field lines (bottom-left) and is ejected from the inner corona, provided the velocity of the ejecta is sufficient. Finally post-flare loops form across the two Hα ribbons on either side of the magnetic neutral line (bottom-right), where open field lines reconnect.

insufficient for the material to leave the solar atmosphere. In contrast, material during a spray event is very rapidly accelerated during the first few minutes of the flare, and attains a speed greater than the local escape velocity of ~ 600 km s^{-1} (Valníček 1964), so that it is ejected into the interplanetary medium. The material from these ejecta is thought to come from the prominence itself (Tandberg-Hanssen *et al.* 1980), in that the magnetic flux tube which originally contained the prominence is distorted by the instability responsible for the filament's rapid rise, and deforms as is escapes into the upper solar atmosphere. Figure 4.3 shows a schematic of this. A good example of the approximations with which one must always deal, when attempting to model such events, is the spray event described by Harrison *et al.* (1988). No X-ray emission was detected during this flare – somewhat puzzling since sprays are necessarily energetic

Table 4.1: Details of NOAA active region 8340, which was selected as a target during the (otherwise) quiet Sun observation campaign of September 1998 at the *DST*. These details are taken from the NOAA weekly online bulletins of solar activity, available at `http://www.sel.noaa.gov/weekly/`

Physical description		Events	
Number of sunspots	8	*GOES* X-ray events	$2\times M$
McIntosh sunspot group classification	*Cko*	(by class)	$10\times C$
Hale magnetic complexity classification	β[1]	Hα Flare classes	$22\times S$
			3×1
Fractional coverage of visible solar hemisphere	3×10^{-4}		1×3
Solar co-ordinates	N19 W54		

[1] *N.B.*: NOAA Space Environment Center lists the Hale class of AR 8340 as β, but Gallagher *et al.* (2000) give the complexity as $\beta\gamma$. See Figure 4.5b and caption for explanation.

events, throwing matter from the solar atmosphere at greater than the escape velocity.

4.2 Observations

4.2.1 Observing plan

From 1998 September 17, observations were carried out at the *Richard B. Dunn Solar Telescope* by Peter T. Gallagher and Kenneth J.H. Phillips. The observation plan included requests for support from the then-new *TRACE* satellite telescope and the *Solar Ultraviolet Measurements of Emitted Radiation* (SUMER) instrument on the *SoHO* space-borne observatory. However, contact with *SoHO* had been lost on 1998 June 24 and only the data from *TRACE* was available as support. The eleven-day-long observing campaign was designed to look at the quiet Sun chromosphere and transition region, but the opportunity was also taken to record multi-wavelength image sequences of a mature active region near the north-west solar limb which had traversed the east limb on the first day of the *DST* observations. The active region had produced several *GOES* C-class flares, and its magnetic complexity was such that it was thought likely

Table 4.2: *TRACE* and *DST* observation wavelengths and passbands. The average cadence of the *TRACE* observations was governed by the total time taken to image in all chosen channels, plus a relatively short time to move the filter wheel and, when necessary, the shutter. This time came to around 100 s. The *DST* observations, meanwhile, had an average cadence of 45 s.

Ion	Wavelength (Å)	Exposure Time (ms)
TRACE		
Fe XII	195	16400[a]
Fe IX/X	173[b]	13800[a]
C IV	1550	13800
C I / Fe II / UV cont.	1600	860
Continuum (UV)	1700	3440
Continuum (visible)	5000	3.2
DST		
Hα (+0.65 Å)	6563.5	200
Hα (+1.00 Å)	6563.8	200
Mg I b_2 (-0.40 Å)	5183.2	450

[a]EUV image exposure times are reduced when TRACE is exposed to radiation belt particles. Initial exposure times are given for Fe IX/X and Fe XII (1993)
[b]173 Å is given as an average wavelength for the passband which includes Fe IX λ171 Å and Fe X λ175 Å.

to flare again, before its west limb passage at the end of the month. As a result, on 1998 September 27 just over 6 hours of *DST* observations (15:06 – 21:43 U.T.) were made of AR 8340, with three hours of support observations from *TRACE* (16:04 – 19:10 U.T.). AR 8340 appears to be the same region (AR 8319) seen on the previous solar rotation during a series of fast-cadence green-line coronal observations made with the high speed Solar Eclipse Coronal Imaging System (SECIS; Chapter 5) on the John W. Evans Solar Facility (ESF) coronagraph at Sacramento Peak on 1998 September 5 (Phillips 2000). Its physical description and flare activity are summarised in Table 4.1, whilst details of the *TRACE* and *DST* observations are given in Table 4.2.

4.2.2 Calibration

Flat-fielding and dark current subtraction were performed on the *TRACE* data using standard *SolarSoftWare* routines (Freeland & Handy 1998), while calibration of the *DST* data was performed using daily flat field and dark current files taken at the observing site. Absolute calibration of *TRACE* data was not possible at this time, and the same was true of data from the *DST*. However, since both observatories had been recording quiet Sun data up until this point, it was decided to use quiet Sun data from 1998 September 22 at around 14:00 U.T. to ultimately act as a reference level in each passband (§4.2.3). All pixel values in data from *DST* and *TRACE* were divided through by the exposure time to give pixel values in DN.pixel^{-1}.s^{-1} (where the term DN (data numbers) is interchangeable with the term 'counts').

4.2.3 Reduction

In order to analyse the flare more quantitatively, an algorithm was used to express the intensity of the flare as distinct from the background component of solar emission – from the network filigree/faculae in the case of the optical/UV emission, and emission from other background sources, such as active regions in the EUV passbands.

The nature of the data we wished to quantitatively analyse is that of time series in the flare's emitted intensity. For each image in a given sequence, the algorithm used identified the location of the pixel with maximum intensity in the *TRACE* field, and defined a subfield of side $64''$ centred on this point in each frame for which data was available in *TRACE* UV and white light bands; subfields of side $128''$ were similarly chosen for the EUV passbands, simply because the extent of the field was twice that in the UV and white light.

The following procedure was then applied. Within each subfield, the background level was defined as the average pixel value, and is hereafter denoted by I_{bgd}. The

flare component of the intensity, $I_{\text{total}}(\text{Flare})$, was then defined by co-adding only those pixels whose value was at least 2σ greater than I_{bgd}. $I_{\text{total}}(\text{Flare})$ was then divided by the average pixel intensity in the corresponding quiet Sun data described.

It should be noted that between 16:31 U.T. and 16:39 U.T., three frames were dropped in the *TRACE* Fe IX/X and Fe XII sequences. These missing frames are preceded in both cases by a rapid increase in the amount of noise-like 'spiking', symptomatic of cosmic ray events in the CCD, and most easily visible in panels 2 & 3 of Figure 4.13 and panel 8 of Figure 4.14. Since this is barely noticeable in the UV exposures this image deterioration may well be due to orbital background effects from either the South Atlantic Anomaly (SAA) or radiation in the High Latitude Zone (HLZ). This effect again occurs, although more severely, between 17:05 U.T. and 17:42 U.T., causing missing or unusable data between these times.

Also to be noted it that, in order to track ejecta from the flare spray, the telescope's field was slewed north-west as the material left the site of the original brightening. However, all *DST* sub-fields shown in this chapter (with the exception of two panels in Figure 4.14) are taken from the same area on the Sun so that direct comparisons are possible between different passbands.

4.3 Analysis

Taken together, then, the *DST* and *TRACE* observations allow us to observe the flare and more particularly the associated ejecta over a wide temperature range, from a few thousand kelvin to 1.5×10^6 K, including intermediate temperatures characteristic of the transition region. Figure 4.4 shows the composite plot of all time series generated by this algorithm from the *TRACE* (Figures 4.4d to i) and *DST* data (Figures 4.4j to l), in addition to the SXR data from *GOES-8* (Figures 4.4a & b) and HXR data recorded by BATSE. (Figure 4.4c). The effects of the missing data mentioned earlier can be seen in the 171 Å and 195 Å light curves of Figure 2 as plateaux between the times referred

to.

The flare-related increase in emission can be broken into three components or ‘stages’: to highlight this in Figure 4.4, a vertical line denotes the beginning of each stage. The first line is drawn at the time of the first spike observed in HXR emission; the second is shown at the second-largest peak of emission in almost all bands (the most obvious exception being in Fe XII, where background radiation effects interfere); and the final line is drawn just before the time of the rapid brightening which constitutes the final, most intense component, after which the SXR emission in the 1.0–8.0 Å band reaches its peak level of 5.2×10^{-6} W.m^{-2}, giving the flare its C5.2 soft X-ray designation.

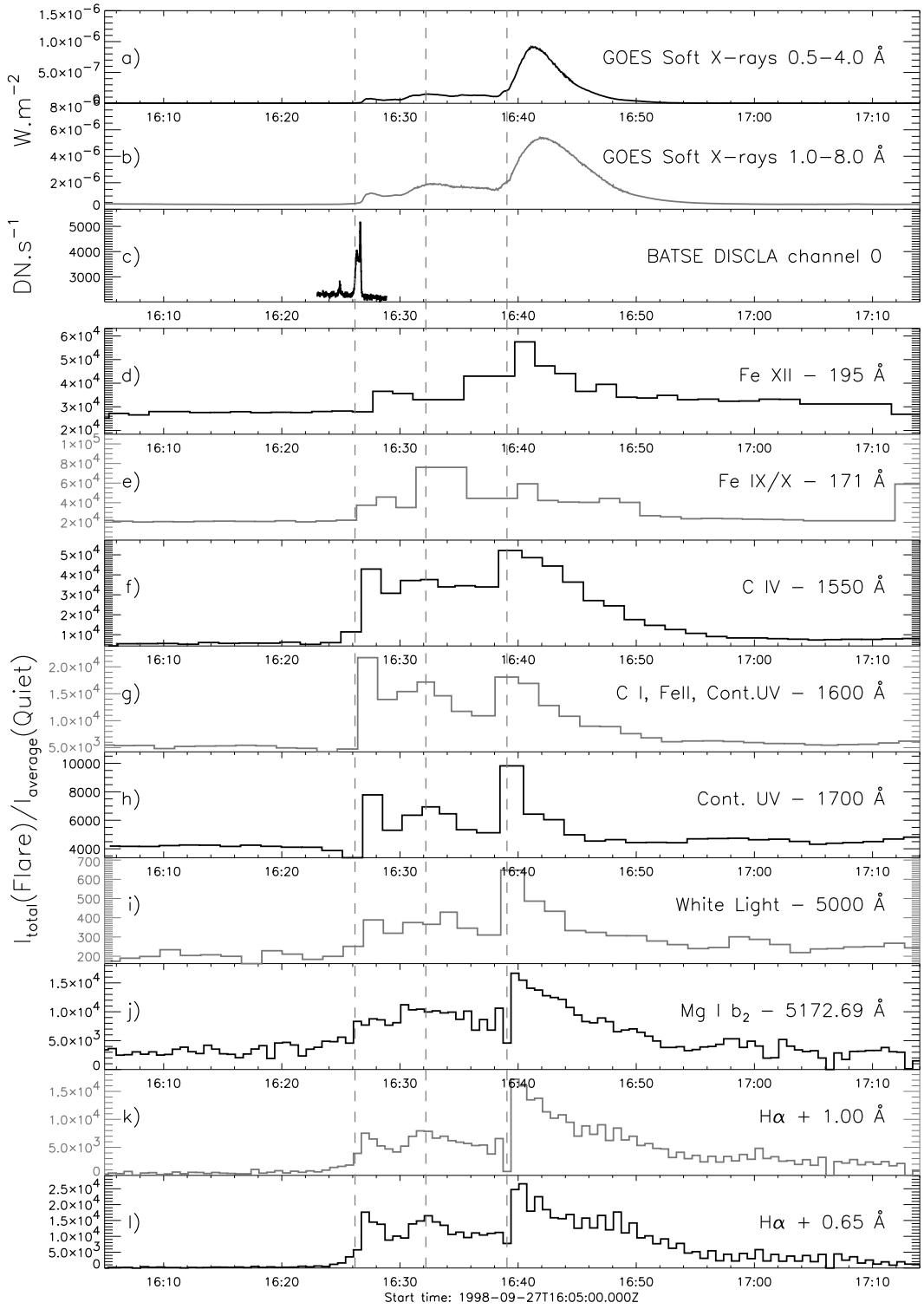

Figure 4.4: Composite plot of all flare lightcurves generated from *DST*, *TRACE*, *CGRO*/BATSE and *GOES-8* satellite data. Vertical lines indicate the start of each, arbitrarily-defined stage of the flare described in §4.3.1. All *DST* and *TRACE* lightcurves are given as values relative to the flux in the quiet Sun observed five days earlier.

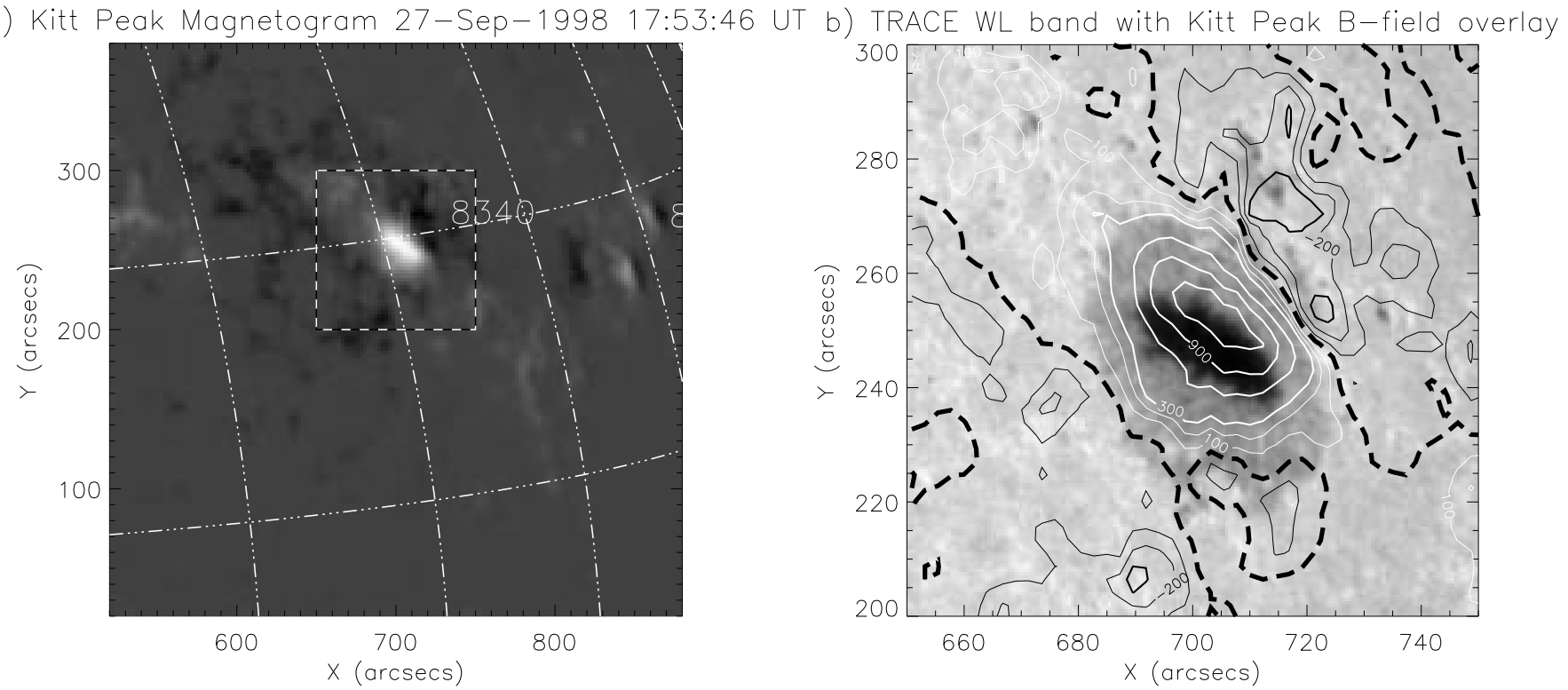

Figure 4.5: a) Kitt Peak magnetogram of NOAA AR 8340 after the 1998 September 27 flare had finished – the dashed box outlines the area shown in figure b); b) TRACE White Light channel image of the same active region with overlaid contours of the longitudinal magnetic field $B_{||}$. White contours indicate an outward pointing field ('positive'), and black contours an inward ('negative') field vector. Thick contours are incremented in steps of 300 G. To better highlight the magnetic field near the inversion line (which itself is shown by the heavy dashed line), thin contours in both black indicate levels of -200 G and -100 G; 100 G and 200 G levels are similarly indicated in white. The relative magnetic simplicity of this β / $\beta\gamma$-class sunspot is evident. Note the island of negative longitudinal field impingeing on the southern portion of the sunspot penumbra which causes ambiguity in the Hale classification of this sunspot.

4.3.1 Flare evolution

At 16:26:20 and 16:26:38 U.T., the large-area discriminator detector (DISCLA) of the *Burst And Transient Source Experiment* (BATSE) on board the *Compton Gamma-Ray Observatory* (*CGRO*) satellite detected two spikes in hard X-ray (HXR) emission from the Sun (Figure 4.4c) just before passing into orbital night-time. This double-spiking signalled the onset of the first of three component brightenings observed in this flare. Figure 4.6 shows a two-stage cartoon outline of the progress of the flare, concentrating on the first and third stages, which are the most energetic in terms of emission (cf. Figure 4.4).

4.3.1.1 Pre-flare

One minute before the hard X-ray burst, two foot-point brightenings (denoted by stars in Figure 4.6) can be seen to the north–west of the sunspot, visible in Hα, Mg b_2, and particularly in C IV (Panel 1, Figure 4.7). The pre-flare activity is perhaps most noticeable in the transition region (C IV – 10^5 K). There is evidence of magnetic reconnection as a high-lying transition region loop (L_1 in Figure 4.6; loop length $\sim 9\times10^4$ km) makes contact with a lower loop (length $\sim 10^4$ km) on the north-western edge of the sunspot's penumbra. Flow is also in evidence along this loop, although its direction is ambiguous due to the restrictions of the time series' cadence.

4.3.1.2 Stage 1

In the first, eruptive stage of the flare (Figure 4.6), an overlying loop (L_1 in Figure 4.6) is seen in C IV to arch from a point north-west of the penumbra to a point above the region B_e around the site of the pre-flare bright footpoints. A loop–like feature connecting these two foot-points then brightens rapidly and erupts (Panels 2 and 3, Figure 4.7) ejecting a large volume of absorbing material. There follows a rapid brightening of this structure in all wavelengths, but most particularly in the wings of Hα and in the UV

bands of *TRACE* (Figures 4.4f to l). In C IV, in fact, the brightening associated with the eruption occupies the entire region B_e, saturating the detector pixels in this region. At the same time, an increase in thermal SXR emission is noted by the *GOES* detectors.

After the eruption, the bright 'loop' visible in Panel 2 of Figure 4.7 separates into two short parallel ribbons clearly visible on Panel 4 of Figure 4.7. By this time (16:30 U.T.), the erupting material is already in the process of rapid acceleration, with cool ejected material visible in the wings of Hα. This initial component of the flare and the associated mass ejection can be interpreted in terms of the emerging flux model described by Shibata (1997) in which a rising magnetic element reconnects with the overlying ambient field. The mass contained within the rising element is then transferred into the reconnected open flux tube to form a jet or spray (Schmieder *et al.* 1995; Canfield *et al.* 1996, see Figure 4.8).

4.3.1.3 Stage 2

The second brightening, at 16:31 U.T., appears to be due to a loop between the penumbra of the major sunspot in AR 8340 and a location around that of the initial eruptive filament. As the two bright ribbons in Panel 4 of Figure 4.7 continue to separate, the ribbon closest to AR 8340 (region B_1 in Figure 4.6b) interacts with a new set of ribbons in the penumbra of the sunspot (marked by region B_2). These ribbons intrude deep into the penumbra, almost to the boundary of the umbra and then gradually fade over the following 7 minutes.

The loop itself is most easily seen in the EUV régime, and its somewhat contorted form is seen to exhibit a brightening in panel 3 of Figures 4.12 and 4.13. The primary sources of increase in UV and optical flux, meanwhile, are at the sites denoted B_1 & B_2 – ostensibly the footpoints of this loop. (It should be noted that, for stage 2 of the flare, the apparent intrusion of the footpoint brightening into the penumbra is not as great as that shown by B_2, which instead refers to the area of enhancement in emission in the final stage of the flare (§4.3.1.4). However, the enhancements are centred at the same

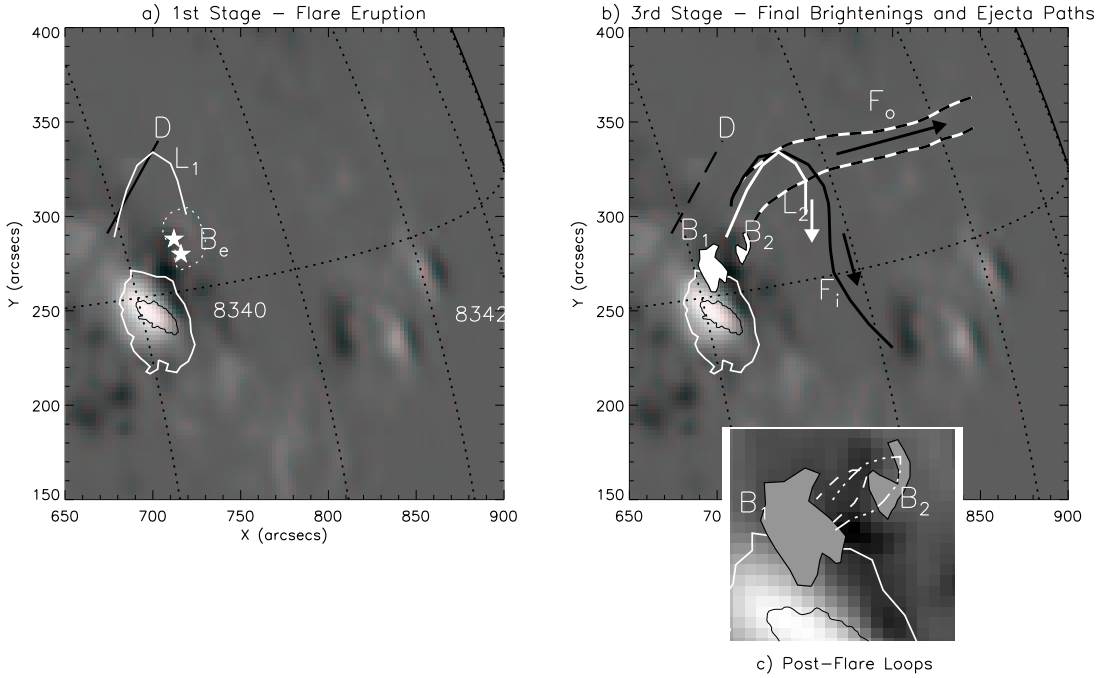

Figure 4.6: Schematic based on *TRACE* Fe IX/X and C IV, and *DST* Hα red-wing sequence data, illustrating the evolution and morphology of the flare and the subsequent ejecta from the initial reconnection out to the solar limb. The Kitt Peak magnetogram (made at 17:53:46 U.T.) underlying the sketched structures has been adjusted to match the field configuration at ∼16:25 U.T. by differentially rotating the image back by 90 minutes. This procedure was performed using the *SolarSoftWare* `DROT_MAP` function. A thin black line delineates the boundary of the umbra, and a similar white line, the penumbral boundary. See text for description of labelled features. The positions of NOAA AR 8340 and AR 8342 are also labelled.

location.)

4.3.1.4 Stage 3

The final stage of the flare (from 16:39 U.T. onward) sees two important developments. At 16:40 U.T. outer footpoint B_2 and the penumbral ribbons (B_2) are again activated and brighten rapidly to produce a C5.2 class event, which then decays exponentially over the final 20 minutes of the flare. The intrusion into the penumbra is deeper than that in Stage 2. The second development is the sudden appearance, marked by a bright flash at 16:47 U.T., of a post-flare loop arcade (Figure 4.7, panel 6), anchored at footpoints between regions B_1 and B_2. These loops – schematically outlined in Figure 4.6c –

appear to be in planes perpendicular to that of the loop connecting these points, much as the reconnecting loops are assumed to form in the wake of a rising filament. The attendant Hα ribbons in such a scenario are not seen, however, although hot EUV-emitting material is still seen to enter the system of outward flows described below. This suggests that the flare is indeed a highly complex example of energy release by reconnection.

As the system re-stabilizes, the loop planes are seen to adjust in apparent orientation, but the loops themselves stay constant in size. At 17:05 U.T. the loops can still be seen and have stopped rotating, but have begun to fade appreciably. Once again, noise effects caused dropped frames and heavily deteriorated data in the EUV bands between 17:05 and 17:42 U.T., after which time the post–flare loops are no longer visible.

Material flow along three main magnetic lanes is also noted in the transition region, each lane originating at a location close to B_1: one lane is a loop with both foot-points near the northern penumbra of the sunspot (L_1); a second is an inter-active region flow, marked by F_i, which rises up from the penumbra along with the first loop, then arcs over this loop to run parallel, and close, to the surface on the region's western side; and a third which is the escaping flow path of the spray (F_o) seen in Figure 1. The flow along each of these paths is denoted by the arrows in Figure 4.6.

4.3.2 Sample flare observations

In the Figures 4.9 to 4.14, we present image sequences taken from some key passbands in our observations, to give a visual representation of the flare's progress.

Figures 4.9 to 4.11 show the development of the flare and associated ejecta at six different times in the two Hα wing filters and the Mg b_2 band respectively. The six times, from 16:21 U.T. to 16:50 U.T., cover the interval from just before the HXR burst to well into the flare decay in soft X-rays. The image field size in each case is 105×113

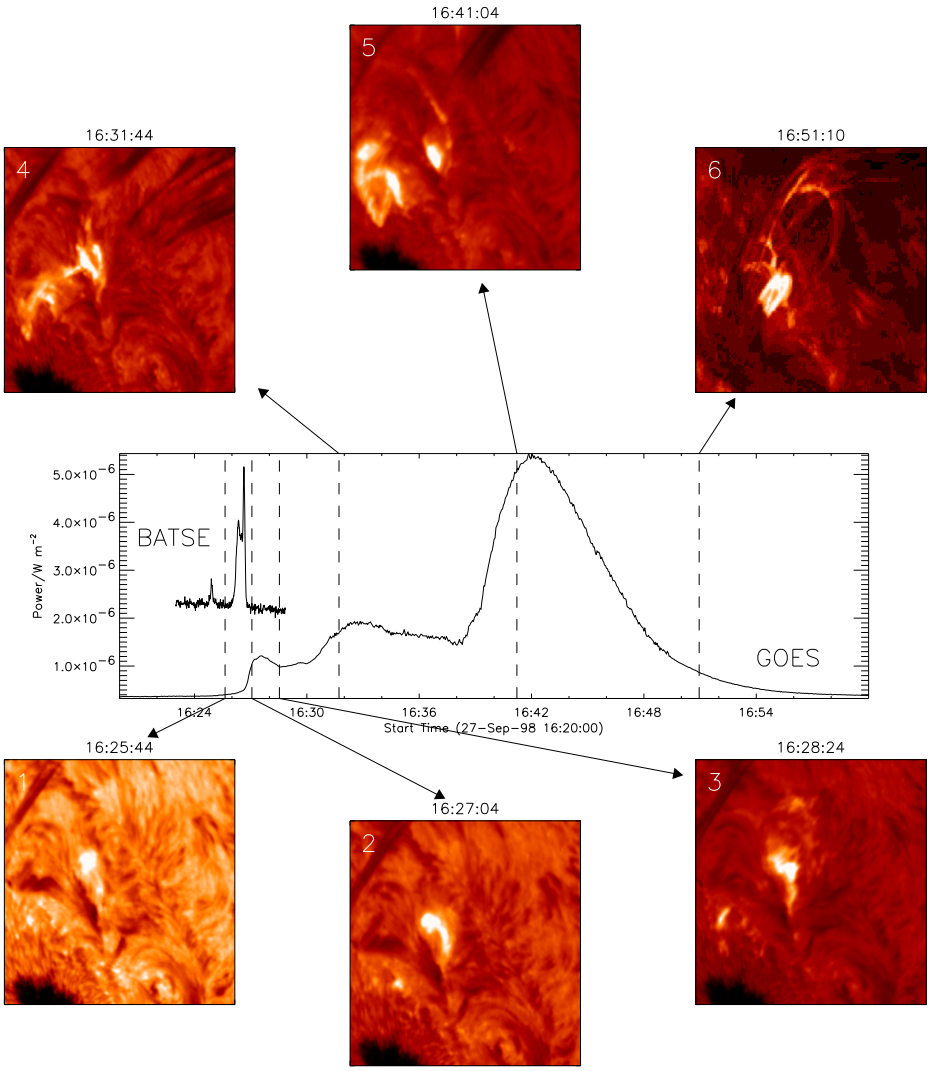

Figure 4.7: The relationship between hard and soft X-ray light curves and the high resolution Hα + 0.65 Å(panels 1–5) and Fe IX/X (171 Å) (panel 6) filtergrams.

arcsec^2. Figures 4.12 and 4.13 show *TRACE* images in C IV and Fe IX/X at six points in time that are almost equivalent to those in the optical images and for the same fields of view. The large sunspot associated with AR 8340 is evident in the optical images and can just be made out in the C IV image from a similar lack of emission at the location concerned.

The six optical images are a selection of the numerous (40-second cadence) images available from the *DST* data. The top portion of Figure 4.14 shows four Hα images, two taken before the telescope slew at 16:39 U.T. and two thereafter. They show the dark absorbing ejected features moving from the flare site, both toward the north-west limb

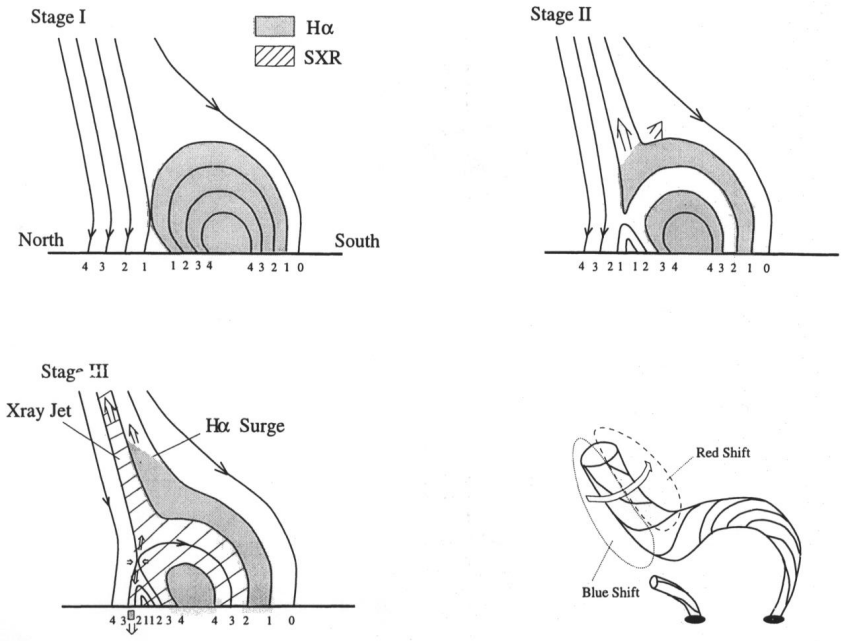

Figure 4.8: Canfield *et al.* (1996) picture of the interaction between emerging flux and an overlying ambient flux tube.

and toward the neighbouring active region AR 8342, to the west; *i.e.* along the paths shown in Figure 4.6. Both trajectories visibly show significant curvature. Inspection of the two Hα sequences, Figures 4.9 and 4.10, show the presence of large amounts of moving absorbing material. This is clear within two minutes of the flare onset (the hard X-ray burst at 16:26 U.T.), the features taking again paths which either connect to nearby regions or are directed outwards at locations to the north-west of the large sunspot.

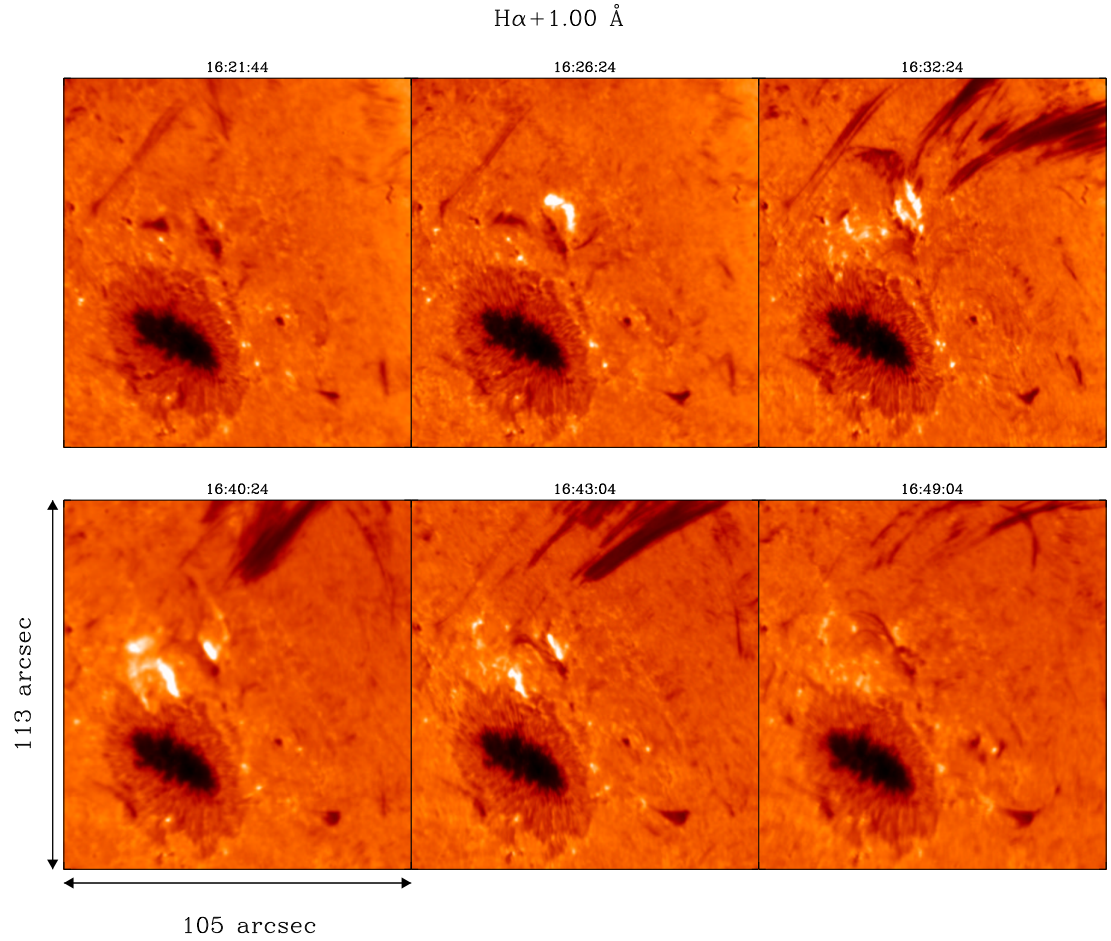

Figure 4.9: Hα + 1.00 Å images of the 1998 September 27 flare (times are indicated above each image).

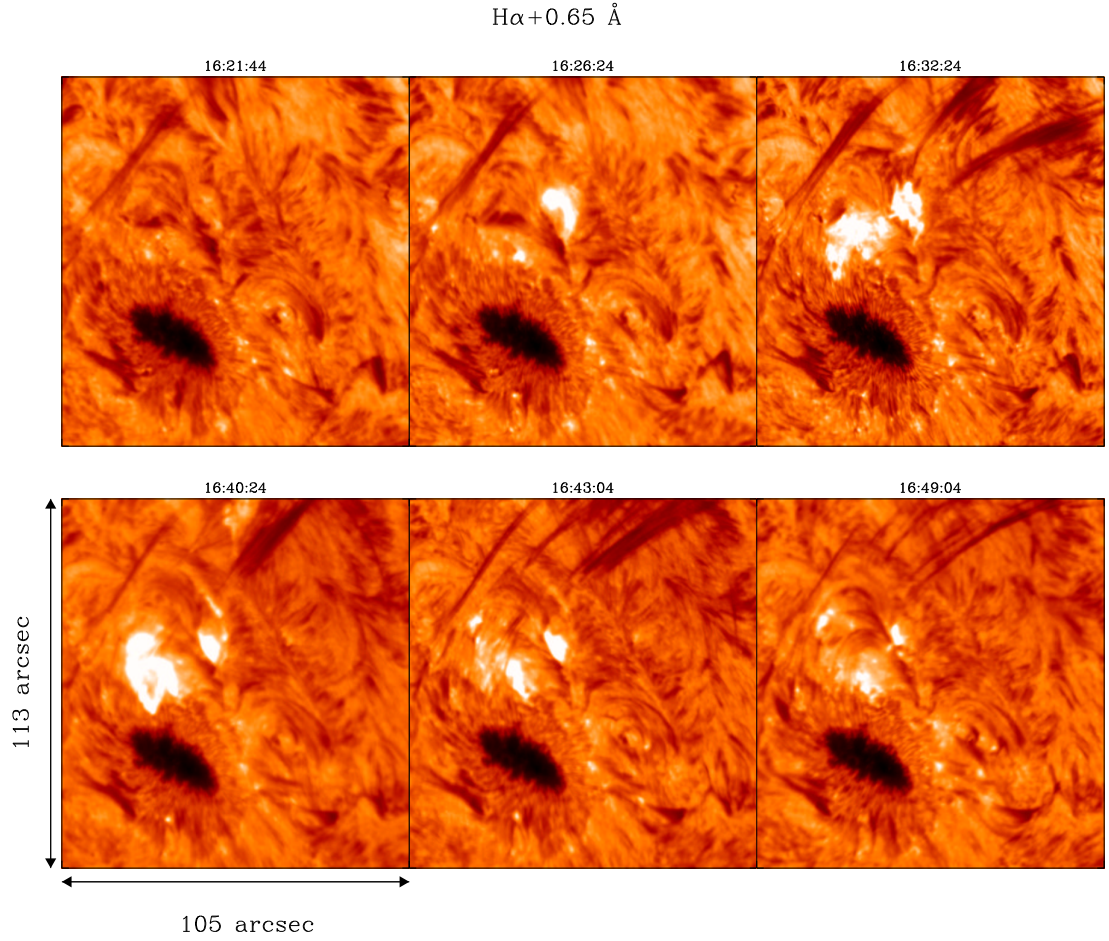

Figure 4.10: Hα + 0.65 Å images of the 1998 September 27 flare (note that the time of the last image is slightly different from the last image of Figure 4).

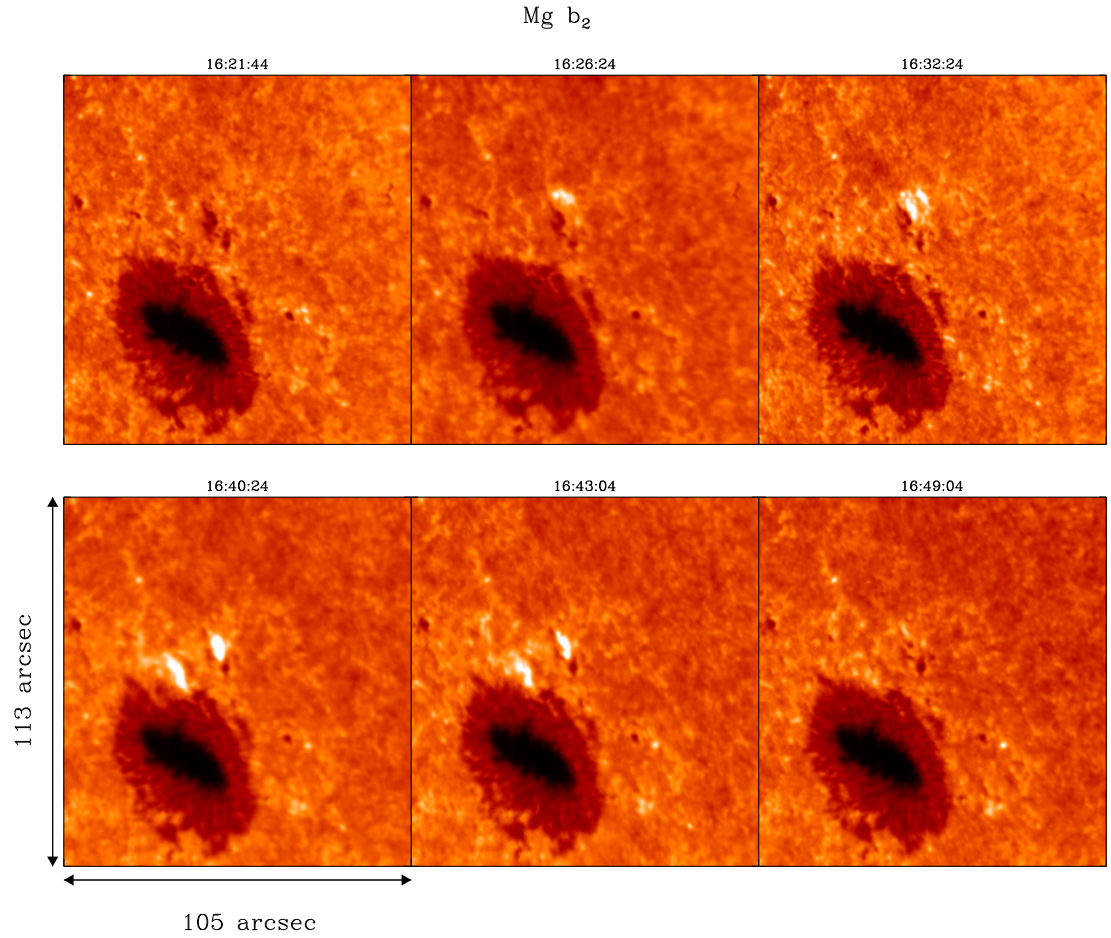

Figure 4.11: Mg b_2 images of the 1998 September 27 flare (times, indicated above each image, are the same as in Figure 4).

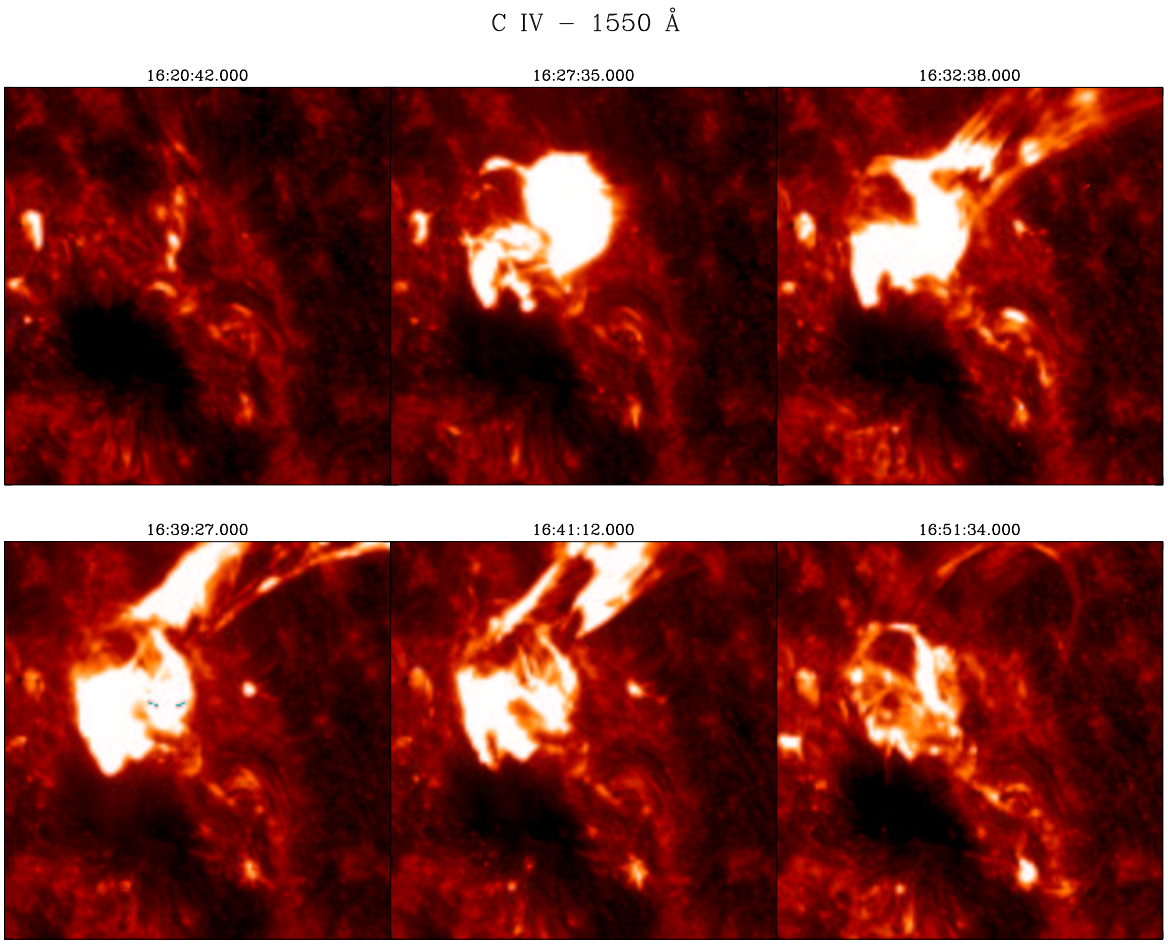

Figure 4.12: *TRACE* C IV (1550 Å) images of the 1998 September 27 flare (times, indicated above each image, are near to those in the optical images of Figures 4–6). The bright emission features have temperatures equal to the emission temperature of C IV, viz. 10^5K.

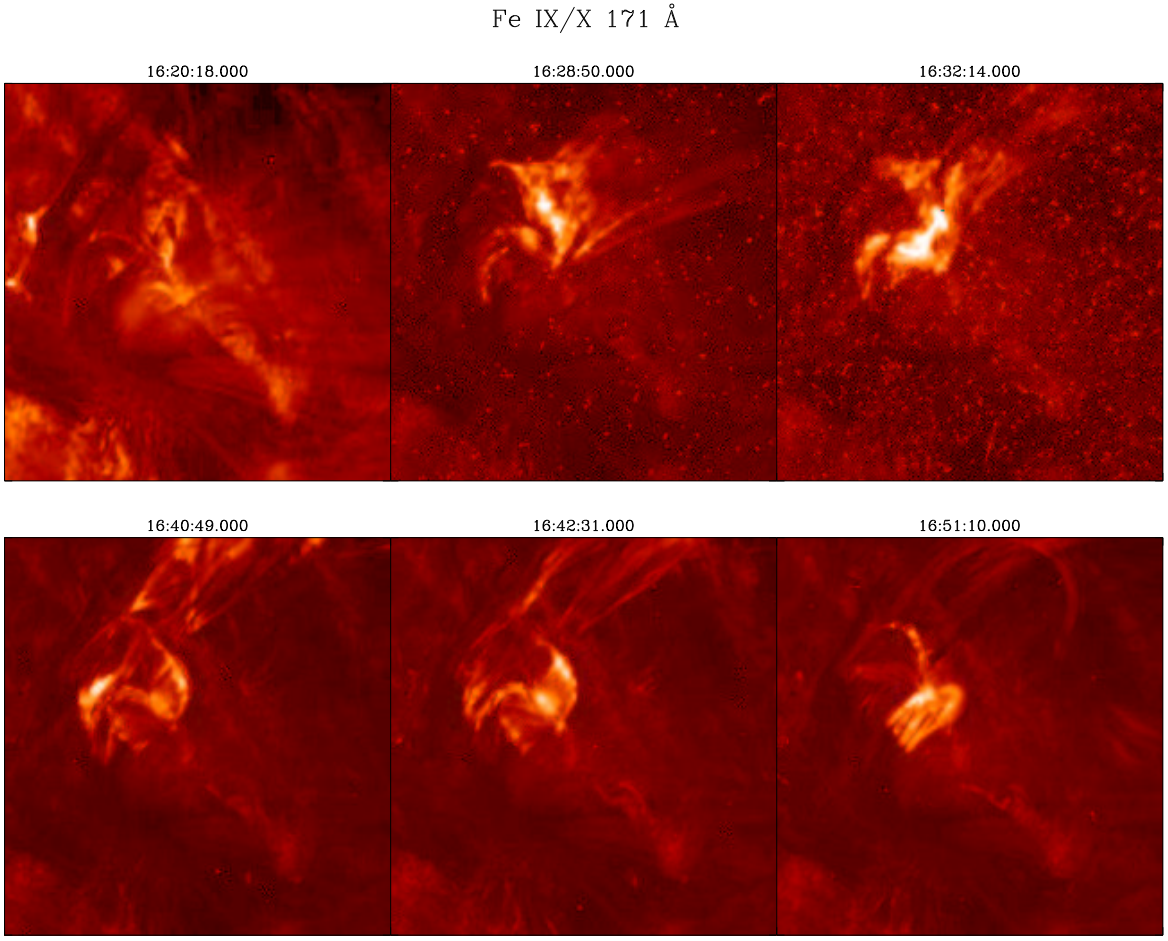

Figure 4.13: *TRACE* Fe IX/X (171 Å) images of the 1998 September 27 flare. The bright emission features have temperatures equal to the emission temperature of Fe IX or Fe X, viz. 10^6K.

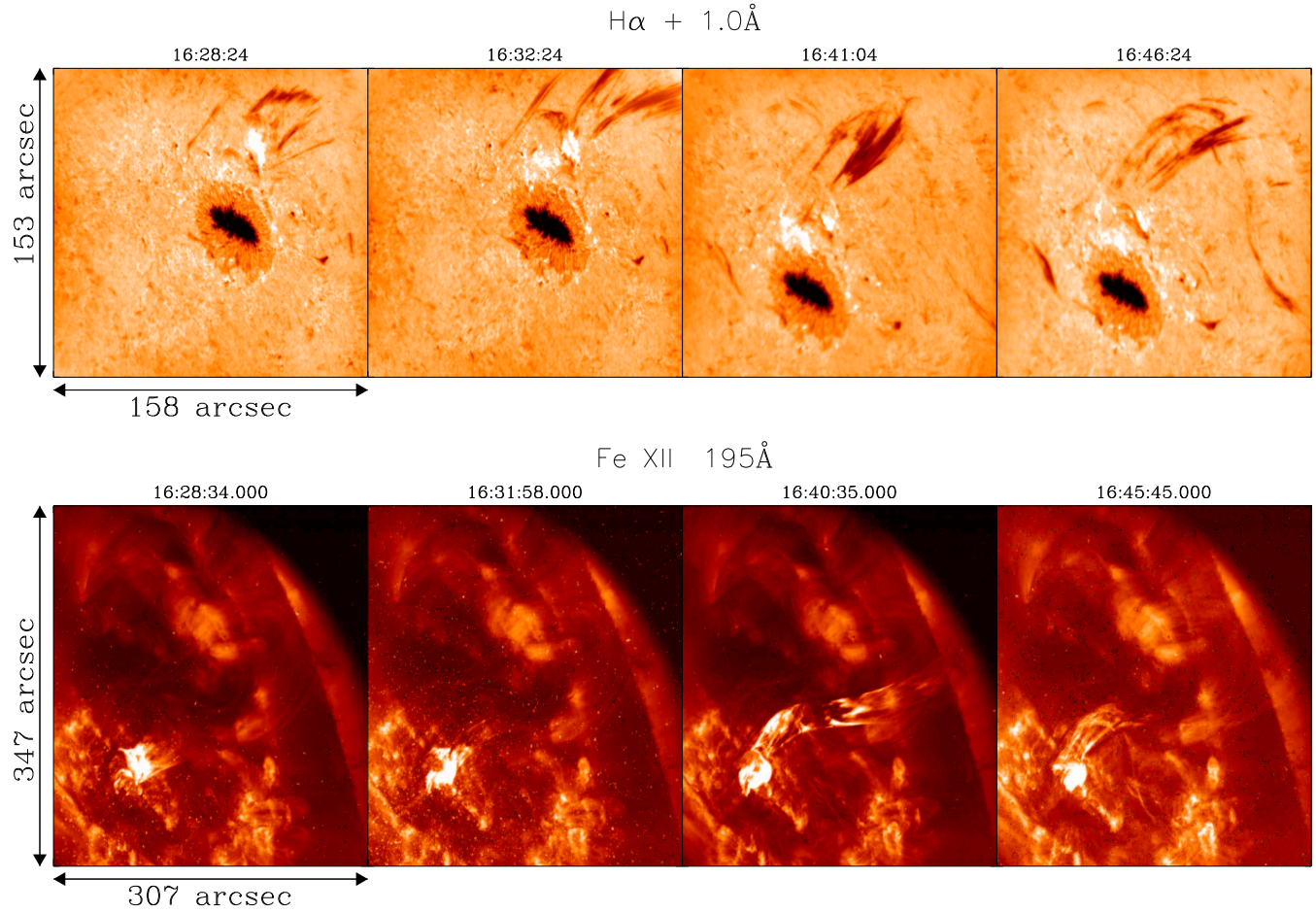

Figure 4.14: Hα + 1.0 Å and Fe XII images of the 1998 September 27 showing the full extent of the spray event. Note, the shift in position of the sunspot in the DST images was due to the telescope being slewed at 16:39 U.T to take in the full extent of the spray.

4.4 Discussion

Because we have discussed the intensity pattern and morphology of the flare in the context of the various passbands in which it was observed, it is worth condensing this information into several noteworthy points.

Two-ribbon flares are normally associated with mature or decaying active regions, of which AR 8340 appears to be an example; we glean this from observations with SECIS on the ESF coronagraph. There is evidence of Hα knots at the impulsive phase (*e.g*. Figure 4.7, panel 1), followed by end-point brightenings (panel 2, same figure), consistent with Hα flare observations (Priest 1981). This is compatible with analysis by Hood & Anzer (1987) which suggests that filaments/prominences are a pre-requisite for such events.

The first *atypical* feature of this (albeit three-stage) flare is the formation of the post-flare loops visible from 16:47 U.T. onward. These buck the normal trend because PFLs are normally associated with two-ribbon flares. These loops are formed below the loop structure thought to be responsible for the second- and third-stage brightenings of the flare. The PFLs do, however, form in planes which are perpendicular to the projection of the above loop on to the solar surface, thereby fitting the two-ribbon picture.

The second unusual feature regarding this loop structure is that the soft X-ray output associated with this brightening appears to be effectively sustained at a constant level for the duration of the second stage of the flare, between 16:32 and 16:39 U.T.. This indicates that either the cooling time is very long in this particular structure, or (perhaps more likely) that multiple reconnections, between magnetic threads in the complex structure, replenish the hot plasma in this loop for several minutes, with the smeared-out soft X-ray time profiles of multiple events resembling a slowly decaying emission.

Perhaps the most puzzling feature of this flare is that the level of soft X-ray emission belies the apparent magnitude of energy released. The intrusion of footpoint brightenings so deep into a sunspot penumbra is usually indicative of very high energy release

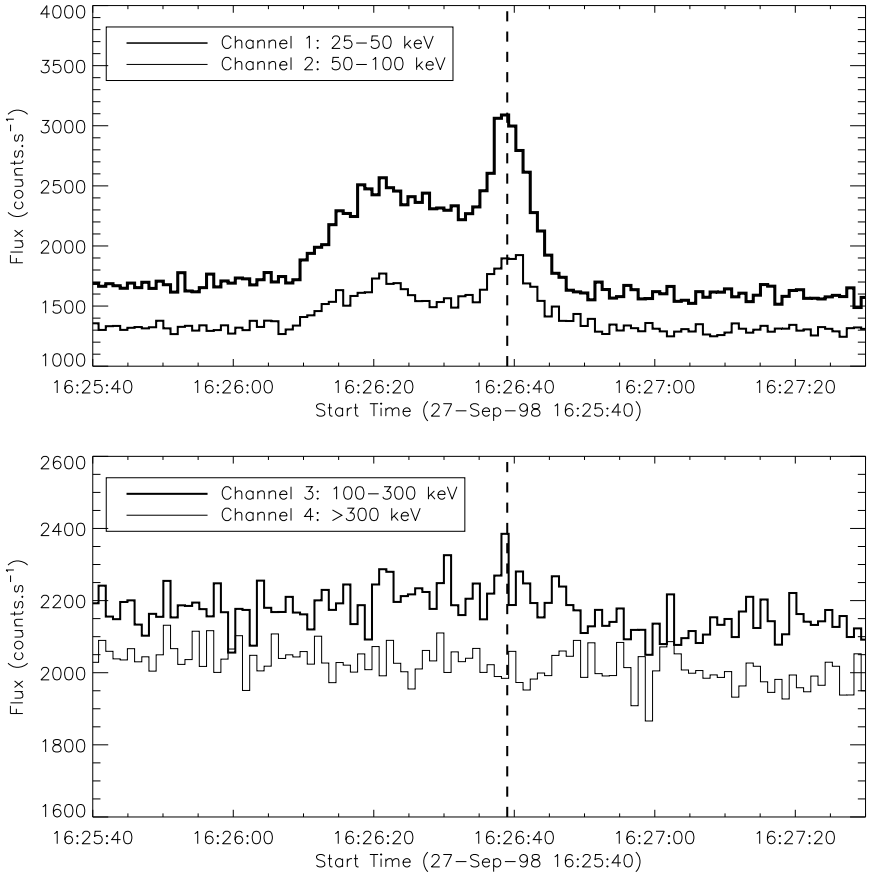

Figure 4.15: Flux in the four channels of the BATSE DISCLA detector. The absence of any enhancement in hard X-ray detection in the $>$ 300 keV range, and the modest increase in the 100–300 keV range (lower panel), imposes an upper limit – of the order of 200 – on the energies of particles released by this flare in the final component of reconnection. The cadence of these observations is 1.024 s, and it is therefore not possible to distinguish the millisecond-timescale lags between the production of progressively higher energy particles, as explored by Aschwanden (1996a,b).

in both hard and soft X-rays. Despite this, the energy release in the third, most energetic stage is only of C-class: this is not a particularly energetic X-ray flare at any stage, let alone in the first and second stages.

To attempt to constrain the energy release, we can refer to the flux in the four available energy channels of BATSE, reproduced in Figure 4.15. The 25–50 keV and 50–100 keV channels show the double-peaked structure which were visible at the start of the flare (16:26 U.T.). Conversely, there is little enhancement (if at all) detected in the HXR flux in the 100-300 keV and no visible increase in the $>$300 keV channel. This helps us to constrain the upper limit of the particle energies to something of the or-

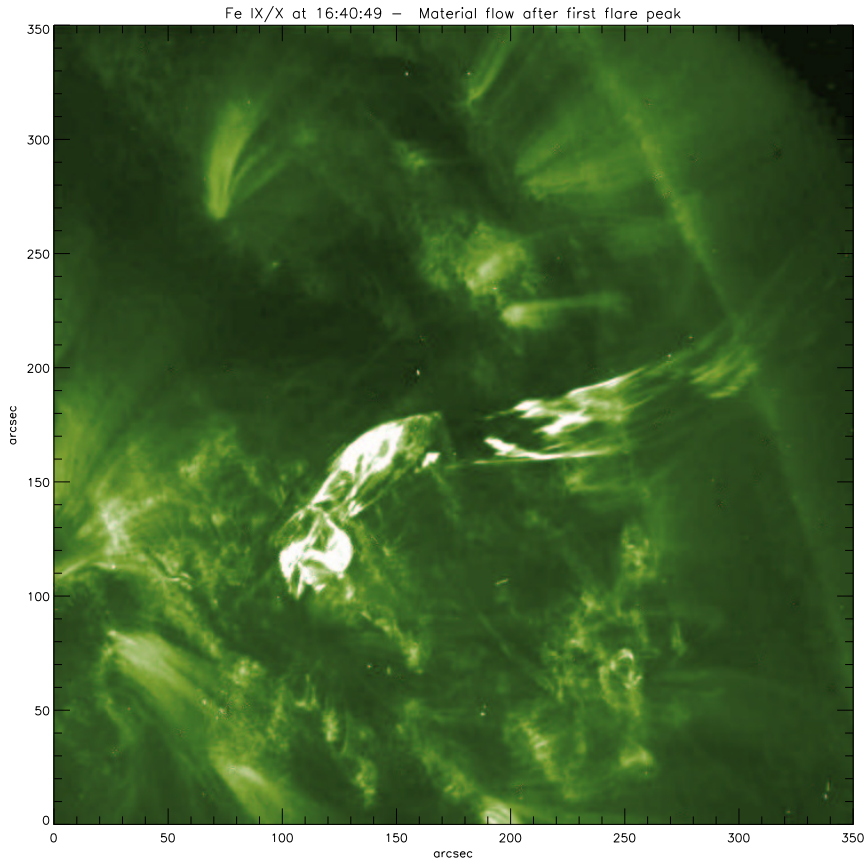

Figure 4.16: Near-full-field *TRACE* Fe XII image taken at 16:49:49 U.T.. The image clearly shows the highly curved path taken by the ejected material, as well as the neighbouring active region AR 8340 at the lower-right of the figure. The vignetting caused by the *TRACE* optics is visible in the upper-right-hand corner of the image. Note that the axes are simply labelled in arcseconds, not in any absolute solar co-ordinate system.

der of 100 keV. We have also tried to constrain the velocity of the ejected material by two *ad hoc* methods, in order to compare its velocity with the apparent X-ray energy release. Figure 4.16 shows an image of the ejected flare material at 16:40:49 U.T.. Attempts were made to isolate blobs or *clouds* (following the nomenclature of Harrison *et al.* (2001)) in the *TRACE* data, and determine their flow velocity from the apparent displacement between two (100-s cadence) images. Assuming that the material at the leading and trailing edges of these clouds can be taken as rigid values for determining their positions, we isolated two, well-defined clouds, *A* and *C* whose motion could be tracked from one frame to the next, and calculated their displacement velocities. These frame-to-frame velocities, V are given in Table 4.4.

Table 4.3: Smear and displacement velocities, U and V, for flare ejecta clouds. Note that the velocities have been corrected for foreshortening from projection effects in the plane perpendicular to the line of sight of *TRACE*.

Frame	Time (U.T.)	A km s^{-1}	B km s^{-1}	C km s^{-1}
17	16:38:51	$U < 614$	$U < 391$	
17-18		$212 < V < 284$		
18	16:40:35	$U < 1260$		$U < 2274$
18-19				$297 < V < 494$
19	16:42:15			$U < 5650$

A constraint – imposed by the second method – is that the length of these clouds, in any given frame, imposes an upper limit on their average velocity at that time, and we may try to calculate a *smear* velocity, U. This assumes that the most distance a cloud can cover in any frame is the distance between its apparent leading and trailing edges. U is therefore defined as the length of the cloud along the path, divided by the exposure time of the frame.

These velocities are clearly rather disparate, but may be interpreted in terms of a spatially dependent acceleration field, implied by the flow's highly curved trajectory. The smear velocities are not quite so useful and impose an upper limit which is very high

Since the jet crosses the apparent limb (e.g. Figure 4.16), we can use a simplified geometric argument to correct the flow velocity for projection effects, and estimate the height at which the leading portion of the jet is observed. Figure 4.17 shows a schematic view of the Sun seen from solar North, where D_r represents the distance of the ejecta from solar centre at point X, as seen (foreshortened) from solar north. We will first assume that the flow takes a path which is entirely radial. Since we know the spherical co-ordinates of the active region (Table 4.1), we know that this radial occurs at a declination angle $\theta = 19^\circ$ (North), and azimuthal angle $\phi = 54^\circ$ (West). At the point X where the flow crosses the limb, the solar latitude, θ_X is 23°. The azimuthal angle of

the active region determines the foreshortening of the apparent path due to projection effects, and θ_X determines the radius r of a great circle at this latitude, and therefore the apparent east-west co-ordinate of X. At X, then, the distance $D_{\rm true} = D_r/\cos\theta_X$ of the ejecta from solar centre is given by

$$D_{\rm true}\cos\theta_X = \frac{r}{\sin\phi}\cos\theta_X = \frac{R_\odot\cos\theta_X}{\sin\phi} \tag{4.2}$$

where the $\cos\theta_X$ term corrects for projection effects along the N-S axis and can be cancelled. The height above the photosphere h is therefore

$$h = R_\odot\left(\frac{1}{\sin\phi} - 1\right) \approx 0.25R_\odot \tag{4.3}$$

At this height, the local escape velocity is not much less than the photospheric escape speed, at $\sim$560 km s^{-1}. Comparing this with the projection-corrected velocities in Table 4.4, we see that many of the estimates fall short of the local escape velocity. However, the material is clearly ejected from the solar atmosphere. This indicates that the features may have been inaccurately matched and/or identified from frame to frame. Alternatively, if we assume that the material *is* travelling at the local escape velocity, then the Fe XII ions have kinetic energy $E_{\rm kinetic} = 1.4\times10^{-7}$ erg. The fastest particles which impacted in the chromosphere have energies of $\sim$ 100 keV, *i.e.* 1.6×10^{-7} erg. So on an order-of-magnitude scale, their appears to be equipartition of energy between the upward- and downward-accelerated flare plasma.

The HXR data presented here serve mostly to indicate the initiation of the flare. Aschwanden *et al.* (1996a,b) use high-cadence, high-energy resolution data from BATSE to determine time-lags between the production of progressively higher energy impulsive hard X-rays. Using these time-lags, they make estimates of the times of flight of these particles to determine the height from which they were produced in the flare of 1992 January 13, *i.e.* the height of the reconnection site. The BATSE observations we present are made with the 1.024 s cadence mode of the DISCLA detector, and it is therefore

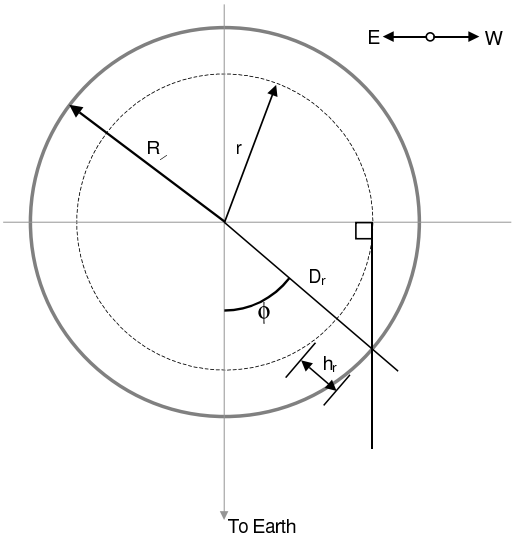

Figure 4.17: Geometry used to estimate flare ejecta velocities. The Sun is viewed from solar north, with $R_\odot$ denoted simply by R. A circle of radius r denotes the great circle at latitude23°, *i.e.* at point X, where the ejecta are seen to cross the limb in the NWSE plane visible from Earth. D_r is the projected distance from Sun centre at X, and h_r is the projected height above the 23° circle. These projected distances must be divided through by $\cos\theta_X$ to return the true values for distance.

not possible to distinguish such time-lags, as can be seen in Figure 4.15. Although we cannot divine the height by Aschwanden's method, Vršnak (1990) suggests (in the abstract) that this height is comparable to the footpoint separation, which in our case is $\sim$15000 km, putting the site safely in the corona ($H > 2000$ km) for the first, eruptive stage of the flare.

More unfortunate, though, is that the data only cover the impulsive phase of the first stage of the flare, and not the more energetic second and third stages. Figure 4.4c shows a slight increase in hard X-ray flux which coincides with the initial rise of the flare in the UV, EUV and optical wavelengths. Interestingly, the main, double-peaked increase in hard X-ray activity recorded by BATSE appears to be nearly *simultaneous* with the rapid increase in flux in all the *TRACE* and DST passbands. The second and third stages are distinct from the first stage in both location and morphology, and we are sadly unable to see if such near-simultaneity exists at those times between the HXR enhancements and the intensity rises in the other observation bands.

4.5 Conclusions

In common with other mass ejections, such as jets (Brueckner & Bartoe 1983; Alexander & Fletcher 1999) and CMEs (e.g., Lyons and Simnett, 1999), this spray is accompanied by a filament eruption which appears to be the case for of the order of 70% of such events (Munro *et al.* 1979). The ejection is directly followed by a two–ribbon flare (e.g., Hirayama, 1974, Švestka and Cliver, 1992) which is observed to move away from the original eruption site along curved paths, some of which extend outwards and others towards a neighbouring active region (see Figure 3), while post–flare loops develop at the flare site itself. A highly complex magnetic field geometry such as that described by Moore *et al.* (1997) and Antiochos (1998) is thus indicated. The second and final components of the flare occur in the penumbral region of the nearby active region AR 8340. In general, flares occurring in the umbral and penumbral regions of large, magnetically complicated spots such as δ or $\beta\gamma\delta$ spots tend to produce M and X class flares such as that discussed by Gaizauskas *et al.* (1998). In this case, and similarly to the 1993 November 11 plasma ejection reported by Ohyama and Shibata (1997), the event had comparatively modest radiative output (C5.2) but seems nevertheless to have been extremely energetic, the bulk of the energy going into the motion of the eruptive material.

It is difficult to reconcile this flare with a particular theoretical picture due to its extremely complex nature. Indeed, the light-curve from about 16:21 U.T. to 16:50 U.T. has been shown to consist of three distinct brightenings which are accompanied by two separate mass ejections. Thus, the combination of these high-resolution ground-based data and complimentary UV/EUV images from *TRACE* reveals that flares and mass ejections such as jets, sprays and CMEs have a more complicated structure than previously observed and should therefore be subject to further high-resolution spatial and temporal investigation.

Chapter 5

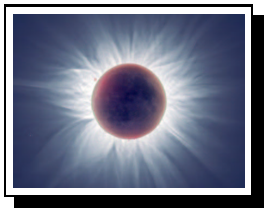

SECIS I: The Solar Eclipse Corona Imaging System

In this chapter, we use data from the SECIS *instrument – developed by the University of Wrocław, Rutherford Appleton Laboratory and Queen's University Belfast – recorded during a total solar eclipse, to search for short-period oscillations and nanoflaring activity in a solar coronal active region. Either or both of these phenomena are believed by many to be responsible for the counter-intuitive heating of the solar corona, but limited evidence exists of short-period coronal oscillations. We use the 4 Å Fe* XIV *λ5303 Å passband of* SECIS *to look for impulsive and oscillatory behaviour in the emitted intensity of coronal features observed on 1999 August 11.*

5.1 Introduction

5.1.1 Background

In the search for oscillations in the outer solar atmosphere, both space-borne and ground-based observations have proved extremely valuable, and evidence exists of oscillations across a broad range of frequencies (Aschwanden *et al.* 1999a). The advantages of satellite observations are perhaps obvious, and are well evidenced by data from the Hubble Space Telescope (*HST*). Firstly, in space, the problem of poor seeing does not exist, since there is no thick, turbulent atmospheric blanket between the observer and the observed object, whether it be a distant galaxy or our closest, parent star. Secondly, there are no effective 'band-block' filters to the spectrum of radiation emitted by astrophysical sources: on Earth, however, the atmosphere is transparent only to visible and radio-wavelength radiation. Important information which can be gathered from UV and X-ray radiation, for example, is lost to our protective atmosphere.

A space-based observatory carries a scientific price, though, above and beyond the financial cost of its launch: the telemetry rate from satellite observatories is severely

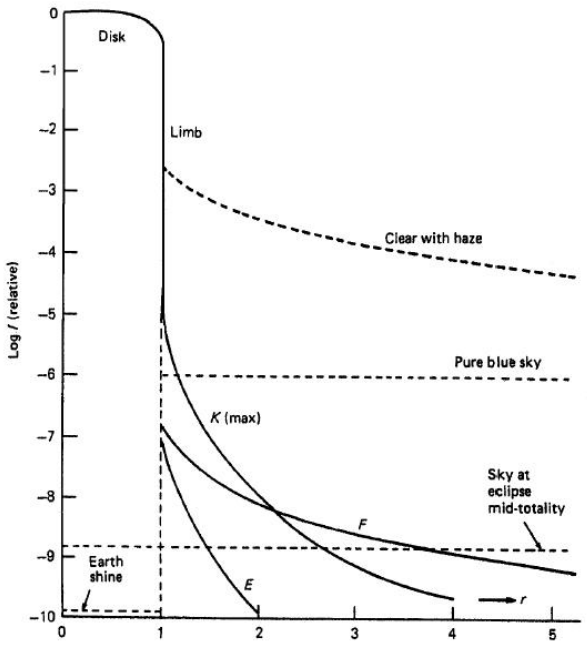

Figure 5.1: Intensity of the corona relative to that of the sky during both normal conditions and a total solar eclipse. From Stenborg (2000).

limited, especially when compared to data rates achievable between ground-based telescopes and neighbouring computers. As an example, consider the rate of data transfer from the *SoHO* satellite observatory (stationed in orbit around the first Earth-Sun Lagrangian point) to its receiving stations on earth. The maximum telemetry rate from *SoHO* is 245.8 kb.s^{-1}, in contrast to the 100 Mb.s^{-1} easily achievable with a standard PC network interface card. This is simply a consequence of information theory, which limits the amount of information which can be received from a remote satellite with finite power, within a given bandwidth of transmission.

Happily, the Sun radiates more than adequate amounts of energy from the photosphere and chromosphere for ground-based observations to be taken at very high cadence ($\sim$100 fps), with high signal-to-noise. This leaves the challenge of observing the much fainter, visible corona at high cadence. In fact, it is in the corona that the highest frequencies are considered by many to be at their most important (Porter, Klimchuk & Sturrock 1994a,b). The large problem is that the faint emission from the corona in visible light is utterly swamped on the disc by the photospheric continuum emission,

and the off-limb emission is washed out by the daytime sky's brightness (Figure 5.1).

An approach used at most solar observatories is to employ a coronagraph – a disk of (arbitrarily) larger angular size than that of the chromosphere – to block the light from the photosphere and chromosphere. During test runs in 1998, SECIS (described shortly) was successfully used at the Evans Solar Facility (ESF) coronagraph at NSO/Sacramento Peak, New Mexico (Gallagher 1999). However, to search for oscillations in the faint light emitted by the corona, it is necessary to remove the sky brightness which acts as a background level. This can only be done when the local sky is not illuminated by the photosphere, *i.e.* during a total solar eclipse. Since these events occur approximately once every 18 months, in highly localised bands all over the world, the means of recording data from the eclipse corona must be portable. The Solar Eclipse Corona Imaging System (SECIS) instrument was designed to be such a portable device for observing coronal emission. It is a collaborative venture built jointly at the Rutherford Appleton Laboratory (RAL) in Oxfordshire and the Astronomical Institute of the University of Wrocław, and jointly funded by the Queen's University of Belfast (QUB).

5.1.2 The forbidden coronal green line of [Fe XIV]

The extremely high temperature of the corona means that the the majority of the emission occurs in the extreme ultraviolet and X-ray wavelength ranges. Since the ions responsible for emission are highly stripped, the energy gaps between the transition terms in any given ion are much larger than in less-ionised nuclei of the same elements, virtually all emitted photons are too energetic to appear in the visible spectrum. There are certain exceptions to this rule, however, thanks to highly forbidden transitions. Two such transitions are the 'coronal red line' of Fe X at 6375 Å, and the 'coronal green line' of Fe XIV at 5303 Å. Both of these lines are due to forbidden magnetic dipole transitions. They are normally only seen in low-density plasmas where collisional de-excitation rates are low enough that magnetic dipole transitions have a

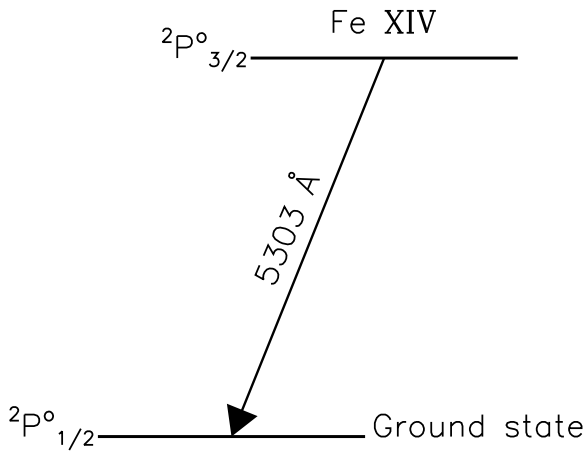

Figure 5.2: Term diagram for the Fe XIV coronal green line. Adapted from Moehs & Church (1999).

much higher probability. These lines are consequently associated with emission from the solar corona, stellar nebulae, and other high-temperature astrophysical plasmas.

For this eclipse experiment, it was decided to observe the corona in the green line of Fe XIV. The choice of the coronal green line over other prominent forbidden lines reflects the structures which one may observe in that light. The Ca XV λ5694 Å line is normally found only in the spectra of highly active regions and flares, where the coronal temperature is hottest: Ca XV has a formation temperature of 4×10 K. The Fe X red line, by contrast, is found at temperatures of 1 MK, characteristic of the base of the corona, and is particularly prevalent in quiet Sun emission. The Fe XIV 5303 line occupies the useful middle ground and is found in almost all coronal active regions, out to great distances, although with varying degrees of intensity. Its formation temperature of ~ 2 MK means that it is seen higher in the atmosphere than the red line, and this satisfies a geometric concern. The higher we see features in the corona during eclipse, the longer we are able to observe them during totality. Features very close to the base of the corona are prone to being occulted much more quickly by the moving lunar disc.

The energy levels responsible for the coronal green line are shown in Figure 5.2. The wavelength was first measured by Edlén to be 5302.86 Å (Edlén 1942), and was in fact a main pointer to the existence of a very hot corona. The line is formed when

electrons in higher terms are radiatively de-excited to the $^2P^o_{\frac{3}{2}}$ metastable level above the $^2P^o_{\frac{1}{2}}$ ground state – *i.e.* this is a fluorescence process. Dr Roger Thomas has therefore suggested using the EUV observations made by the Solar EUV Rocket Telescope & Spectrograph (*SERTS*) experiment (Brosius *et al.* 1998) to calculate the most probable observed wavelength of the transition. It is feasible to try and constrain the energy difference between these two states by taking the energy difference of photons decaying from a common upper level to both lower states. Dr Thomas uses the *SERTS* EUV measurements and associated errors to find a weighted average of these transitions, which he finds to yield a wavelength of 5303.3 ± 1.05 Å (Phillips 2002)

The expected, thermal Doppler width of the Fe XIV line is given by Equation 5.1 (Mariska 1992):

$$w = \frac{\lambda}{c}\sqrt{\frac{2kT}{M} + \xi^2} \tag{5.1}$$

where w is the half-width at $1/e$ of the maximum of the Doppler profile, M is the mass of the Fe nucleus (55.847 amu), k is Boltzmann's constant, T is the electron/ion temperature and ξ is the velocity corresponding to the maximum of the local micro-turbulence velocity distribution. The FWHM of this profile is given by $1.665 \times w$, which gives 0.5Å if micro-turbulence is neglected. In practice, the ξ^2 term will approximately double this width.

5.2 Observing site and timing details

The path of totality of the 1999 eclipse is shown in Figures 5.3 & 5.4. The location chosen to observe the solar eclipse was a military base by the Bulgarian town of Šabla on the western shore of the Black Sea, approximately half-way between the coastal resort of Varna (60 km south-west, on the southern limit of totality), and the Romanian port of Constanta to the north. The latitude/longitude of the site at Šabla was $43°31'.60\,\mathrm{N}$ $28°31'.60\,\mathrm{E}$, and therefore on the central line of totality (Figure 5.4). The site was recommended to the SECIS team by the late Vladimir Dermendzhiev of the Bulgar-

Figure 5.3: Path of totality of the 1999 European total solar eclipse. Eclipse Predictions by Fred Espenak, NASA/GSFC.

ian Academy of Sciences. Using tables of eclipse data calculated by Fred Espenak, at NASA/Goddard Space Flight Center, and interpolating for the exact position of Šabla, it is found that totality ran from 11:11:06.23 U.T. (second contact) until 11:13:27.77 U.T. (third contact), giving a totality of slightly over 141.5 s.

5.3 Data

5.3.1 Capture

Using the Image32™ control software, the exposure time for each of the 6 364 frames in each channel was set to 20 447 μs, and the delay (readout) time to 2 097 μs. This adds up to a total cycle time of 22 544 μs which translates to a frame rate of 44.36

Figure 5.4: Path of eclipse totality through Romania and Bulgaria. Šabla is shown to the top-right of the map.

exposure.s^{-1}, the most crucial number in the interpretation of the SECIS data. It also has the consequence that the recording of the data overran totality by 2 s, as the data recording began at the very beginning of totality, in order to avoid heavily saturating the pixels (particularly in the white light channel) and leaving residual charge during the first few seconds of totality. As a safeguard during recording, a window pops up affording a smaller, side-by-side view of the images being recorded by both cameras in real time. This was used to check the images for signal level, stability, etc.

5.3.2 Conversion

Using SECIS, data are initially stored as a single `.raw` file for each stream, before being imported into Image32™ and converted, via a 'sequence' stage (which can be saved with a `.seq` extension as an intermediate file), into the astronomical standard FITS format. Each image in each sequence is saved as a separate FITS file, in which each

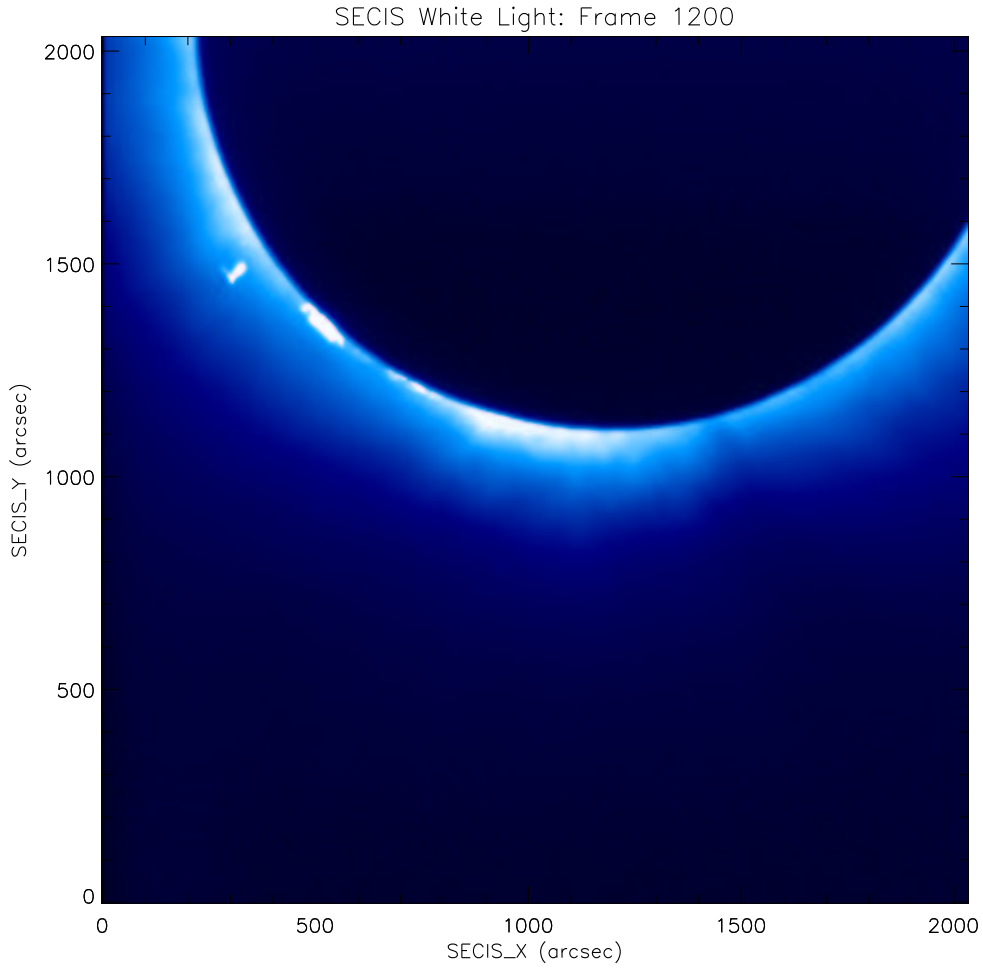

Figure 5.5: Sample SECIS white light image. This is the 1201st image in the sequence. The white light corona, including several chromospheric prominences, can clearly be seen. A so-called 'suspended' prominence can be seen to the upper-left of the image.

pixel has a 16-bit depth, which should not be confused with the native 10-bit output of the SECIS instrument. Each FITS file occupies 501 kB of disk space.

These data were initially stored at the Space Data Centre (RAL) courtesy of Dr David Giaretta. From there, the data were copied to QUB using FTP.

5.3.3 Calibration

In addition to the 12 728 eclipse images captured by the SECIS team, 3000 additional calibration images were obtained in sequences of 500. Two sequences of flat-field im-

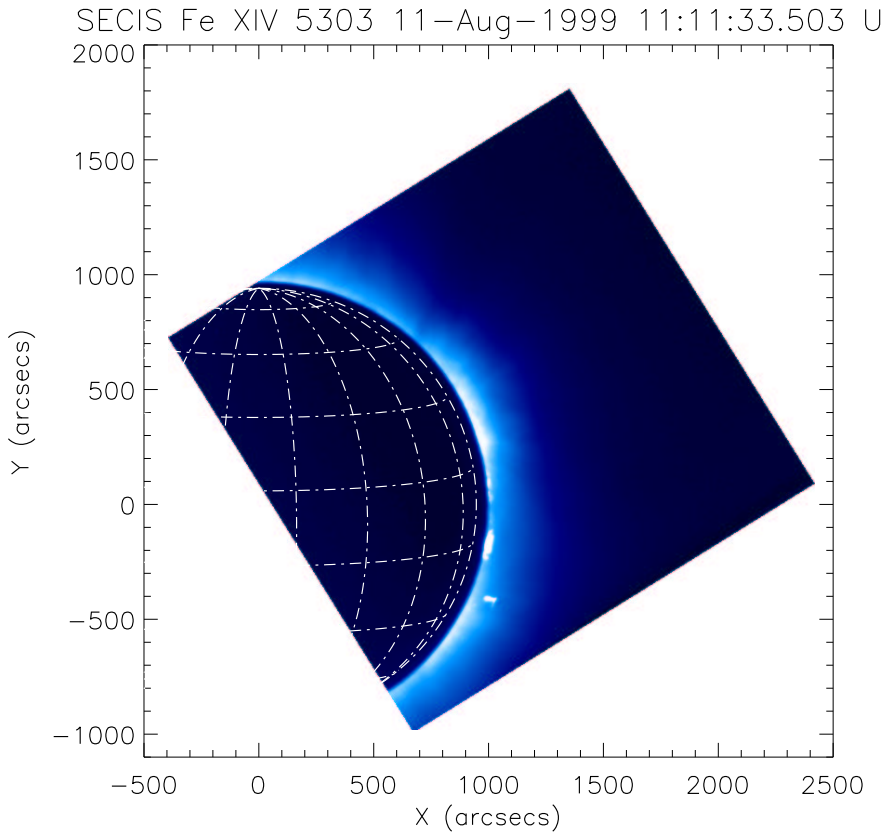

Figure 5.6: Sample SECIS white light image map, created from the image in Figure 5.5, showing exact position and orientation on the solar disc.

ages – used to calibrate the relative response of each pixel – were made simultaneously in each camera by recording illuminated sky immediately after eclipse. Table 5.1 gives the details of these files. The `flatnarrowb` and `flatbroad` sequences were obtained simultaneously, and this is also true for the `flat1` and `dark` sequences. Average flat-field frame surface plots are also shown for the `flatnarrowb` (left) and `flatbroad` (right) series in Figure 5.3.3.

The procedure used to calibrate each image in the SECIS data is as follows.

- average the 500 images in each sequence together to produce average dark-current and flat-fields, ignoring sporadic, anomalously high-value pixels ($>3\sigma$ above the mean).
- choose the most reasonable flat-field I_{flat} for each camera

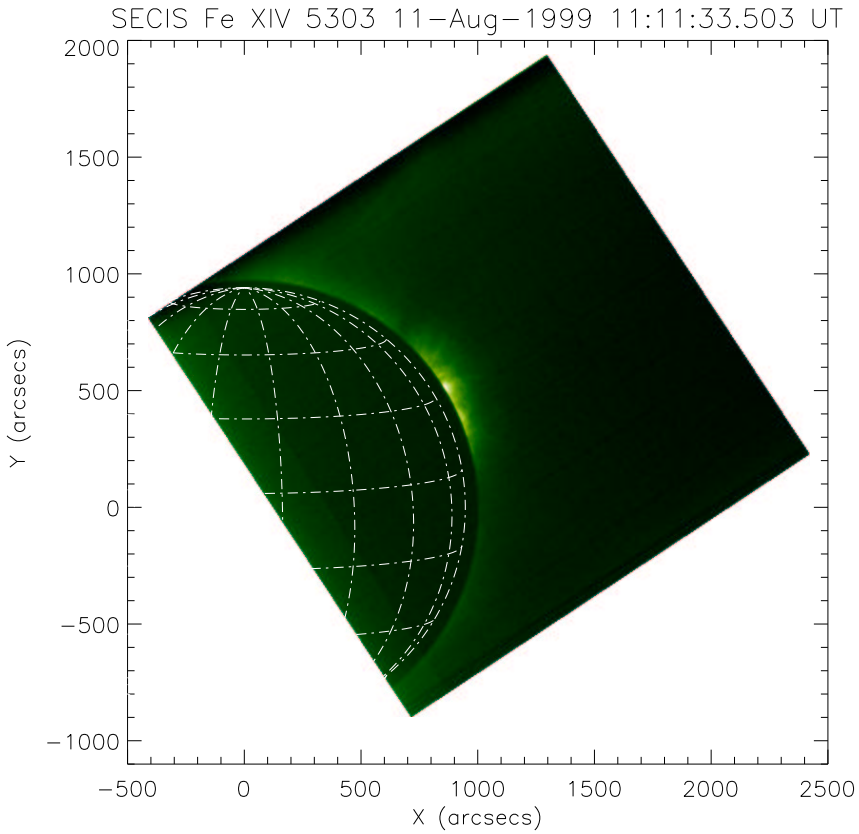

Figure 5.7: Sample SECIS Fe XIV λ5303 Å image map, created by alignment with Figure 5.6, showing exact position and orientation on the solar disc.

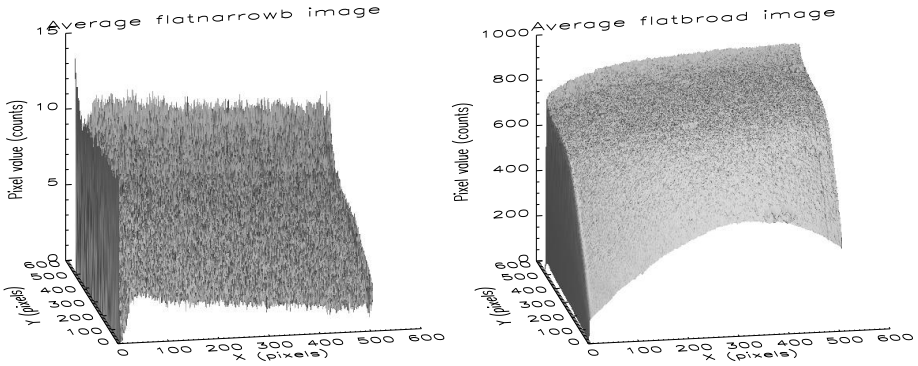

Figure 5.8: Surface plots of the average flat fields in each channel.
Left: `flatnarrowb` average image. Right: averaged `flatbroad` image.

- subtract the averaged dark current I_{dark} from each chosen flat
- use the following algorithm to calibrate each image:

$$I_{\text{true}} = \left[\frac{(I_{\text{raw}} - I_{\text{dark}}) \times \overline{I_{\text{flat}} - I_{\text{dark}}}}{I_{\text{flat}} - I_{\text{dark}}} \right] \tag{5.2}$$

Table 5.1: 1999 August 11 calibration file details. There are 500 consecutive images in each sequence.

Sequence Name	Type	Location on sky relative to Sun	Channel
`flatbroad`	Flat-field	45° W	White Light
`flatnarrowb`	Flat-field	45° W	Fe XIV
`flat1broad`	Flat-field	20° E	White Light
`flat1narrow`	Flat-field	20° E	Fe XIV
`darkbroad`	Dark current	N/A	White Light
`darknarrow`	Dark current	N/A	Fe XIV

where, for each camera, I_{raw} is the raw input frame, I_{dark} is the average dark-current frame and I_{flat} is the average chosen flat-field frame.

Additionally, the term $\overline{I_{\text{flat}} - I_{\text{dark}}}$ is the average value of the averaged flat-field frame, so that the above image is response-corrected by dividing by a flat field which is normalised to its *average* value, rather than its maximum value.

By far the largest task in the calibration, however, was the removal of a time-dependent pointing offset, found in the sequences on first inspection. Qualitatively, this is a drift of the apparent position of the Sun first in the +X +Y direction by a few arcseconds, before reversing and swinging down in the -X -Y direction, before stabilising and returning almost to its original position at the end of totality. This can be seen more quantitatively in Figure 5.9, where the scale of the drift is shown to be $\sim 80''$. This may have been associated with the heliostat, but PR has investigated this problem to no conclusion.

As the idea behind SECIS is to look for short timescale changes in coronal features, the motion of prospective analysis targets with time is clearly undesirable, so the drift had to be removed. Several methods were applied in the attempt to correct for the drift, including cross-correlation of the whole images, lunar limb and the 'detached' prominence at heliocentric co-ordinates ($1000''$, $-400''$) in Figure 5.6 (top-left of Figure 5.5), as well as of the edge-enhanced images. However, the most satisfactory method em-

ployed was that chosen by our collaborator Pawel Rudawy (PR) from the Astronomical Institute in Wrocław. PR used a sobel filter to define the edge of the Moon (the strongest feature) in the white light sequence. Since the motion in each series was observed to be exactly the same (notwithstanding a reflection in the X direction), using the white light sequence seemed the best option, as the signal was much stronger in these data. The Sobel filter returned a portion of almost half the lunar circumference, and PR then fitted these points to a circle, as a first approximation. In a second iteration, all points defined by the lunar limb which fell more than 3σ away from this best fit were discarded, followed by another execution of the circle fit. This had a two-fold benefit, in that both the size and position of the Moon in each image could be determined from this algorithm, allowing a deduction of the angular scale of the pixels.

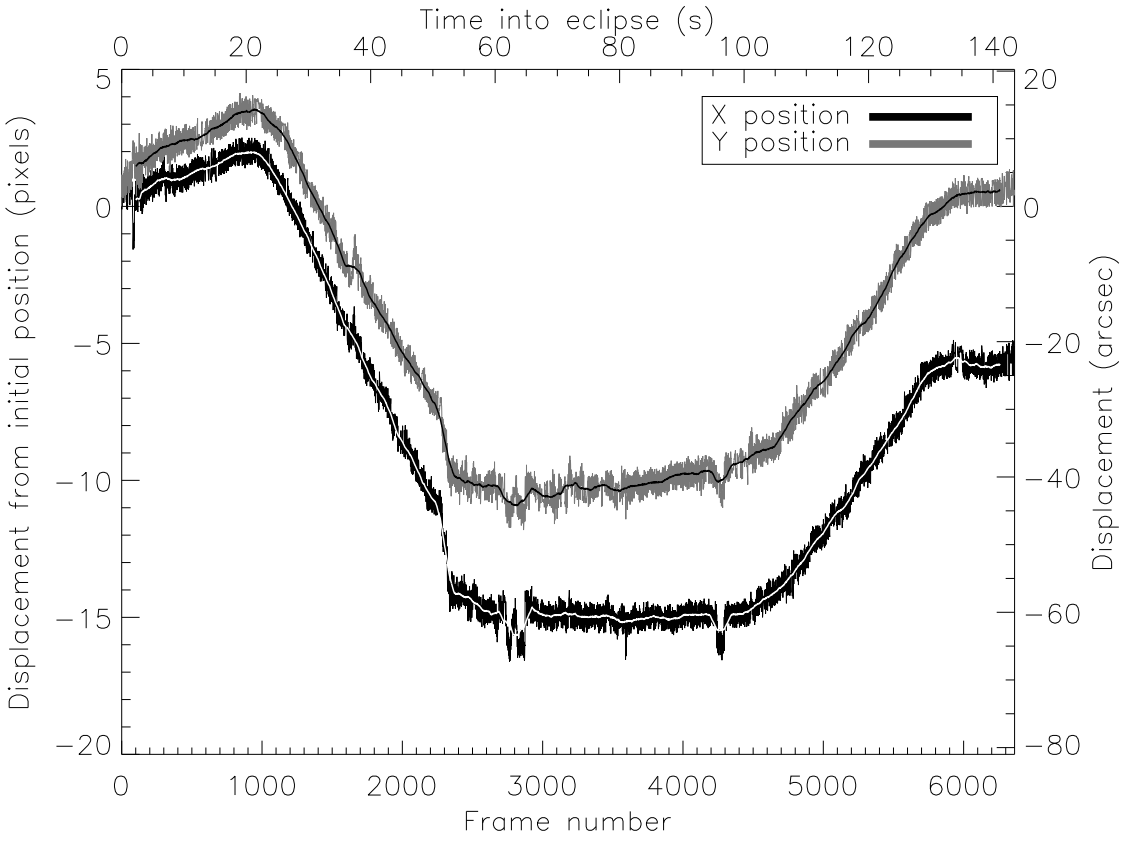

Figure 5.9: Position of the Sun as a function of time during the eclipse, with respect to the SECIS field of view. The position shown is that calculated from the drift of the 'suspended' prominence visible in the white light sequence.

A second method was then used as a check. PR fitted a so-called centre-of-gravity

to the intensity from the suspended prominence visible to the left of the Sun (SECIS reference frame). The position of the prominence can be tracked in images taken by *SoHO/EIT*, and is seen not to move appreciably over the duration of eclipse. It is found that the position of the centre of the prominence and the position of the centre of the Moon diverge at a constant rate – as one would expect, since the Sun and Moon have constant angular speeds across the sky for the duration of eclipse. The speed of their mutual separation is calculated, by this method, to be of $0.37''.s^{-1}$.

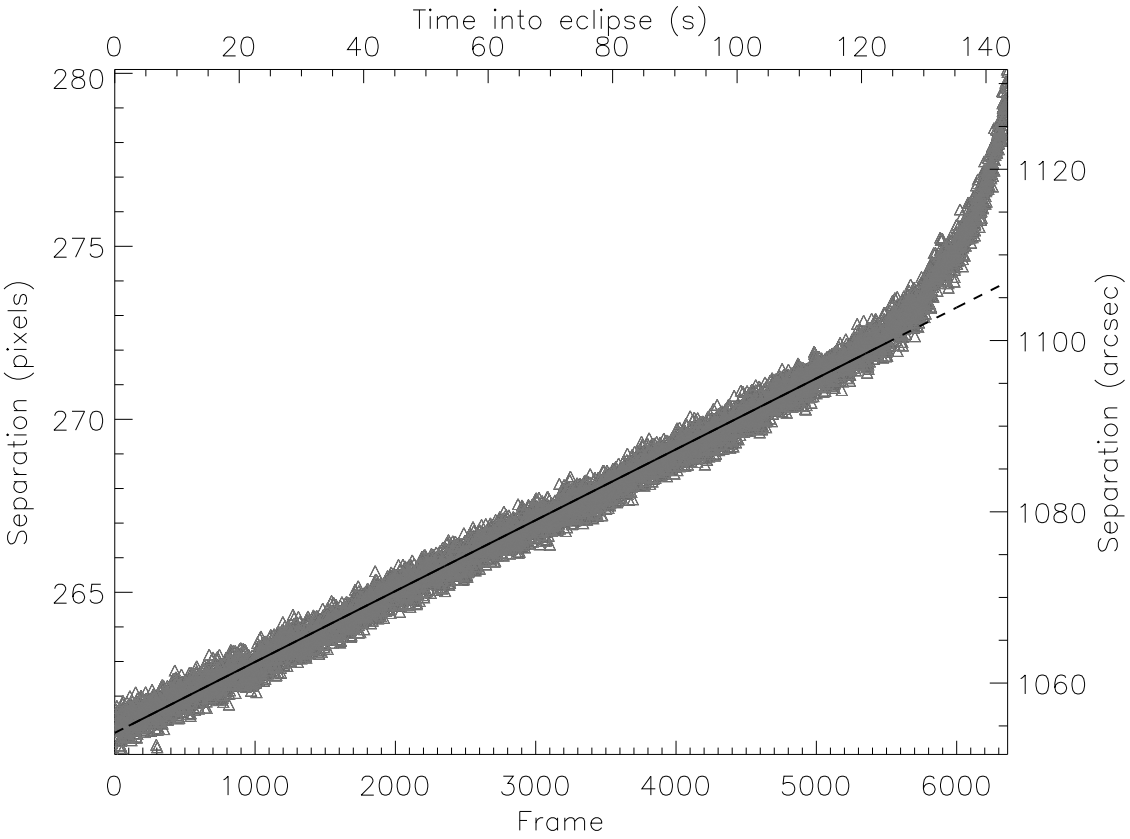

Figure 5.10: Separation of prominence and Moon centre. The non-linear relationship in the last 20 s is due to the reappearance of the chromosphere and scattered photospheric light at the end of totality, causing some level of blooming and impairing the ability of an edge filter to locate the exact position of the edge of the moon.

The compensation of this motion was performed using a 2-dimensional polynomial interpolation routine, with cubic convolution. This method was very helpfully suggested by Tom Berger at Lockheed Martin Solar & Astrophysics Lab (LMSAL), and employs the IDL function `POLY_2D`. This method is employed by the standard *TRACE* software for the alignment of image sequences. The principle is that a bandwidth-

limited ($\omega_0 \leq \omega_{max}$) signal can be best reconstructed by convolving with a sinc function, where:

$$\text{sinc}(x) = \frac{\sin(\pi x)}{\pi x} \tag{5.3}$$

The name 'cubic' comes from the fact that the sinc function is approximated by a cubic polynomial in x and y. This is used to reconstruct a smooth, best-fit function to the pixel values in the x and y directions, which should approximate the pixel values given by $f(x,y)$. This function is then used to find the signal $g(x,y)$ (Equation 5.6) in each pixel when it is shifted by a non-integer number of pixels. The transformation matrix which is used allows both translation and deformation of the input image. In this case, however, we only want translation of the image. The x' and y' are defined as follows:

$$x' = a(x,y) = \sum_{i=0}^{N}\sum_{j=0}^{N} P_{i,j}x^j y^i \tag{5.4}$$

$$y' = b(x,y) = \sum_{i=0}^{N}\sum_{j=0}^{N} Q_{i,j}x^j y^i \tag{5.5}$$

$$g(x,y) = f(x',y') = f\{\, a(x,y),\, b(x,y)\,\} \tag{5.6}$$

The functions $a(x,y)$ and $b(x,y)$ are polynomials in x and y of degree N, whose coefficients are given by P and Q, where:

$$P = \begin{pmatrix} P_{0,0} & P_{1,0} \\ P_{1,0} & P_{1,1} \end{pmatrix} = \begin{pmatrix} x_{disp} & 0 \\ 1 & 0 \end{pmatrix} \tag{5.7}$$

$$Q = \begin{pmatrix} Q_{0,0} & Q_{1,0} \\ Q_{1,0} & Q_{1,1} \end{pmatrix} = \begin{pmatrix} y_{disp} & 1 \\ 0 & 0 \end{pmatrix} \tag{5.8}$$

Therefore, $x' = x_{disp} + x$ and similarly $y' = y_{disp} + y$, which is what is needed for linear translations of the input image to the output image. Non-zero entries in any of $P_{1,0}$, $P_{1,1}$, $Q_{1,0}$ or $Q_{1,1}$ would cause deformation of the input images, rather than simple translation. It should be noted that x' and y' express the new pixel's position as a function of

the old pixel position (x,y), so that the displacements calculated from the positions of the prominence and Moon must be multiplied by -1 before being used in this method.

5.3.4 Reduction

All of the analysis of the SECIS data from the 1999 eclipse has been performed in RSI's IDL™ programming environment, often using the *SolarSoft* libraries which are written and maintained by various astronomers and programmers in the solar physics community. The majority of these routines are written for specific missions/instruments, such as *TRACE* or *SoHO*/CDS, and many then become more generalised to suit similar problems for other instruments. Details of the *SolarSoft* distribution can be found in Freeland & Handy (1998) and at

`http://www.lmsal.com/solarsoft/`

as well as at several mirror sites on the World Wide Web.

5.3.5 Method of detection

5.3.5.1 Wavelet analysis

Virtually all of the analysis of time series data was performed using wavelet analysis (Mallat 1998; Torrence & Compo 1998). This method is based on elements in the time-frequency domain known as *wavelets*. In the analysis of oscillatory motion, a base wavelet ψ with both phase and amplitude (real and imaginary) parts is desirable. For our purposes, the wavelet used is the Morlet wavelet, and is the product of a Gaussian curve with a sinusoidal function:

$$\psi(\eta) = \pi^{-1/4} \exp(i\omega_0\eta) \exp(\frac{-\eta^2}{2}) \tag{5.9}$$

where $\eta = t/s$ is the dimensionless time parameter, t is the time, s the scale of the wavelet (i.e. its duration), $\omega_0 = s\omega$ is the dimensionless frequency parameter, ω is the frequency of the wavelet's sinusoidal component, and $\pi^{-1/4}$ is a normalisation term (Torrence & Compo 1998). By scaling the wavelet in duration so that the periodicity of the sinusoidal part matches a given frequency, the wavelet can then be convolved with a time series x_n, centred at a given time t, to find the contribution of that frequency to the x_n as a function of time. Applying this to a number of *scales* s (*i.e.* frequencies), the wavelet transform W_n is defined as

$$W_n(s) = \sum_{n'=0}^{N-1} x_{n'} \psi^* \left[\frac{(n'-n)\delta t}{s} \right] \tag{5.10}$$

where δt is the time step between the x_n, and is a 2-dimensional, complex image in time/scale space.

The wavelet *power* transform is the square of the absolute value of each point in the 2-D transform, and is a commonly used form in searching for oscillatory power in a time series. Furthermore, this power transform can be summed over its time dimension to form a *global wavelet spectrum*, and is the analogue of the Fourier power spectrum of a time series. Alternatively, sections can be taken through the power transform, at constant time t, to see the instantaneous or *local* wavelet spectrum.

Confidence levels were calculated by Torrence & Compo's (1998) `wavesignif` routine, which uses the assumption of a mean power spectrum, against which deviations can be tested for significance. The mean value of this power spectrum will be equivalent to σ^2 of the time series, where σ is the standard deviation. The time series is further assumed to be normally distributed, consistent with photon noise, and has a χ^2 distribution with one degree of freedom (DOF). Since the total power in the series is given by $\sum |x_n|^2$, the power series $|x_n|^2$ is distributed with 2 DOF. The 99% confidence level is calculated by multiplying the mean power level by the value of χ^2 which corresponds to the 99th percentile of the distribution. Values which exceed this level in the power transform thus have only a 1% chance of being due to noise.

The wavelet transforms were calculated employing IDL routines already used by researchers at QUB to investigate oscillations on much longer timescales in CDS data (*e.g*. Gallagher *et al.* 1999; Banerjee *et al.* 2000). The emphasis in our analysis is on oscillatory behaviour in both the white light and Fe XIV channels.

5.3.5.2 Search tactics

If we define a detection of nanoflaring or microflaring activity as being a sudden rise in intensity greater than a given threshold (*e.g*. 3σ) above the mean intensity level – *e.g*. Porter *et al.* (1995) looking at solar X-ray flux; Robinson *et al.* (1999) looking at YZ CMi's EUV flux – then no evidence was found in the analysed SECIS data of microflaring or nanoflaring activity.

In IDL, the data were read into cube arrays: that is, an array of three dimensions, *e.g*. $504\times504\times200$, if 200 frames were read, where 504 is the number of pixels in the x axis, 504 that in the y axis and 200 in the time, or t axis. For the purposes of display, data are usually shown one image at a time, or averaged over a certain interval in time. On computer displays, where animations are possible, data can be played back as sequences, or 'movies'. Because the SECIS data do not contain wildly-varying images, it is of little use to represent them by multiple sequential images. Time series (or 'lightcurves' – the terms will be used interchangeably) were created by selecting the intensity in a particular pixel, or number of pixels, in each frame and plotting as a function of time.

5.4 Analysis

5.4.1 First inspection of the data

As outlined earlier, initial inspections revealed that the field of view of the instrument was not stable during the eclipse in either camera. However, it also revealed that the signal in the Fe XIV channel was somewhat lower than had been expected, given the filter transmission.

5.4.1.1 The Fe XIV green line channel

Measurements of the Fe XIV filter transmission profile around the desired 5303 Å wavelength were carried out by KJHP and Dr Francisco Diego at UCL. The original order for the filter was delayed due to technical difficulties, and a filter was supplied with an approximately correct central wavelength. In order to achieve the desired central wavelength, the filter supplied had to be tilted so that the incident beam was 1° from the normal to the filter. Figure 5.11 illustrates the transmission profiles calculated by Dr Diego. (It should be stated that these data have been digitally recovered from the plot originally supplied). The diamond scatter plot superimposed on the solid curve shows the measured data points with 1° tilt required for our experiment, while the smooth, solid profile shown is a Gaussian fit to these points. The second, dashed curve is the transmission profile at normal incidence, shown for comparison. The tilt/turn-table in which the filter was mounted, however, was accurately marked in degrees, and the SECIS team are quite certain that the orientation of the filter was correctly set at the observing site. Two important points may now explain the poor signal-to-noise in the Fe XIV channel. First, the vacuum-to-air wavelength correction for the λ5303 Å line was neglected in the pre-experimental stages. This correction is ~ 1.48 Å, and shortens the true wavelength, so that the green line's air wavelength was most likely ~ 5301.5 Å. A dot-dashed line is drawn at this wavelength. The filter transmission is 10.2% at this

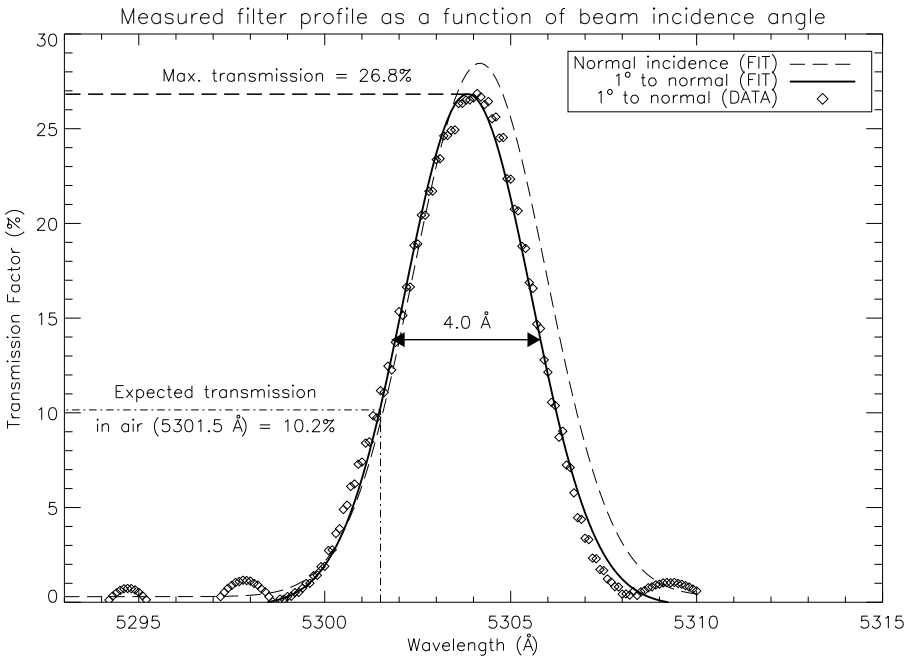

Figure 5.11: Profile of SECIS Fe XIV interference filter, manufactured by Barr Associates. The filter's optimum transmission at 5303 Å is obtained when the angle between the incident beam and the normal to the filter is 1° (solid line). A dashed line is shown for the filter's response at normal incidence to illustrate the effect on transmission of a small deviation in the filter's incidence angle.

wavelength, *cf.* 26.8% at maximum transmission; we therefore already have a reduction by a factor of 0.38 in the transmission at 5303 Å.

Second, there is also the question of the exact wavelength of emission of the coronal green line, explained in §5.1.2. If the wavelength is as much as 1 Å shorter than the expected wavelength of 5303.3 Å, then the transmission of the filter could be further reduced to a few percent of the incident intensity.

5.4.1.2 The white light channel

The initial inspections also revealed that the white light channel images suffered from a decaying defect in camera 2 which disappeared over the course of the first 100 images and did not reappear (Figure 5.12). At the end of the eclipse, some vertical streaks are also seen in the white light images, but this may simply be due to charge leakage from

overexposure. Since the very end of totality is an undesirable time to look for variance in the data – due to the re-emergence of the chromosphere from behind the lunar disc – this is not of primary concern.

Figure 5.5 shows the first image in the white light sequence, and is typical of the white light images recorded. Scanning anti-clockwise from (200″,2050″) in this reference frame, we see first a slight brightening of the diffuse corona before encountering the prominence already discussed. There is a second prominence along the limb about (500″,1350″), and then two active regions with NOAA designations AR 8656 (900″,1100″) & AR 8651 (1100″,900″). The final notable feature is that of a coronal hole visible at (1400″,1100″).

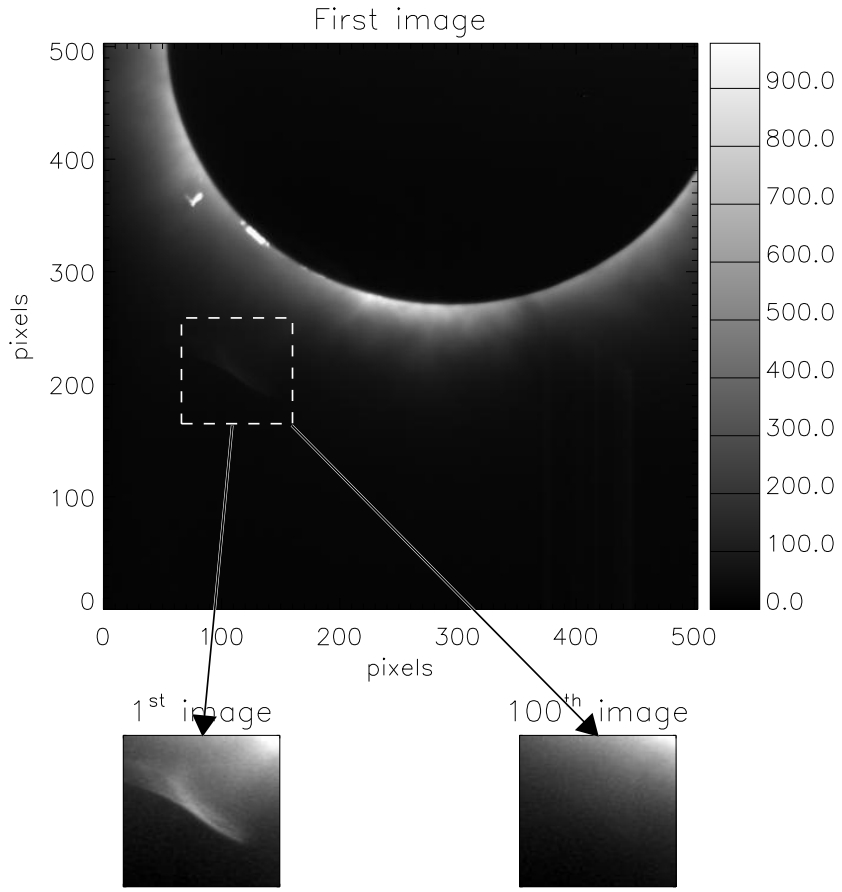

Figure 5.12: Disappearance of a defect initially seen in the SECIS white light (Camera 2) image sequence, but which disappeared over the course of the first 100 images.

Table 5.2: Resonant frequencies, detected with wavelet analysis, in the pointing error functions $X(t)$ and $Y(t)$.

Direction	Resonant Frequencies (Hz)							
$X(t)$	0.36	0.49	0.58	1.1	2.2	14.2	16.4	18.7
$Y(t)$	0.29	0.44	1.1	2.0	13.7	16.9		

5.4.2 Spurious sources

Because of the discovery of the pointing drift from the initial look at the SECIS Bulgaria data, it was decided to investigate the possibility that the pointing functions – hereafter referred to as $X(t)$ and $Y(t)$ – contained resonances at certain frequencies. The reason for this was that the error in the pointing was suspected to have its roots in the motion of the heliostat: it was effectively the only moving component in SECIS. Since mechanical motions often contain resonances, frequency domain analysis was performed on the pointing functions to determine any resonant frequencies which might contaminate the data. Several such frequencies, detected using wavelet analysis, were found to exist between the $X(t)$ and $Y(t)$ functions, and are listed in Table 5.2.

5.4.3 Detection of oscillatory behaviour

The search for high-frequency oscillatory behaviour began by searching for identifiable magnetic structures in the SECIS data. The reasons for this are outlined in Chapter 1, viz. that these structures are waveguides because of the overdensity of material with respect to the ambient coronal plasma. A second consequence of this density is that signal from these structures is the highest, and so detection is more likely than in the more tenuous surroundings.

As already mentioned (§5.4.1), the white light data show evidence of two active regions on the limb of the Sun visible outside the lunar disc. The more prominent

of these is NOAA designation AR 8651 (beyond the limb, but last sighted directly at N26W91 on 1999 Aug 10), particularly in the Fe XIV sequence. More important is that there are several well-defined structures visible in AR 8651 where it is possible to search for wave-guided oscillations of the type thought to be responsible for heating processes. Figure 5.13 shows the visible extent of this active region in the Fe XIV sequence.

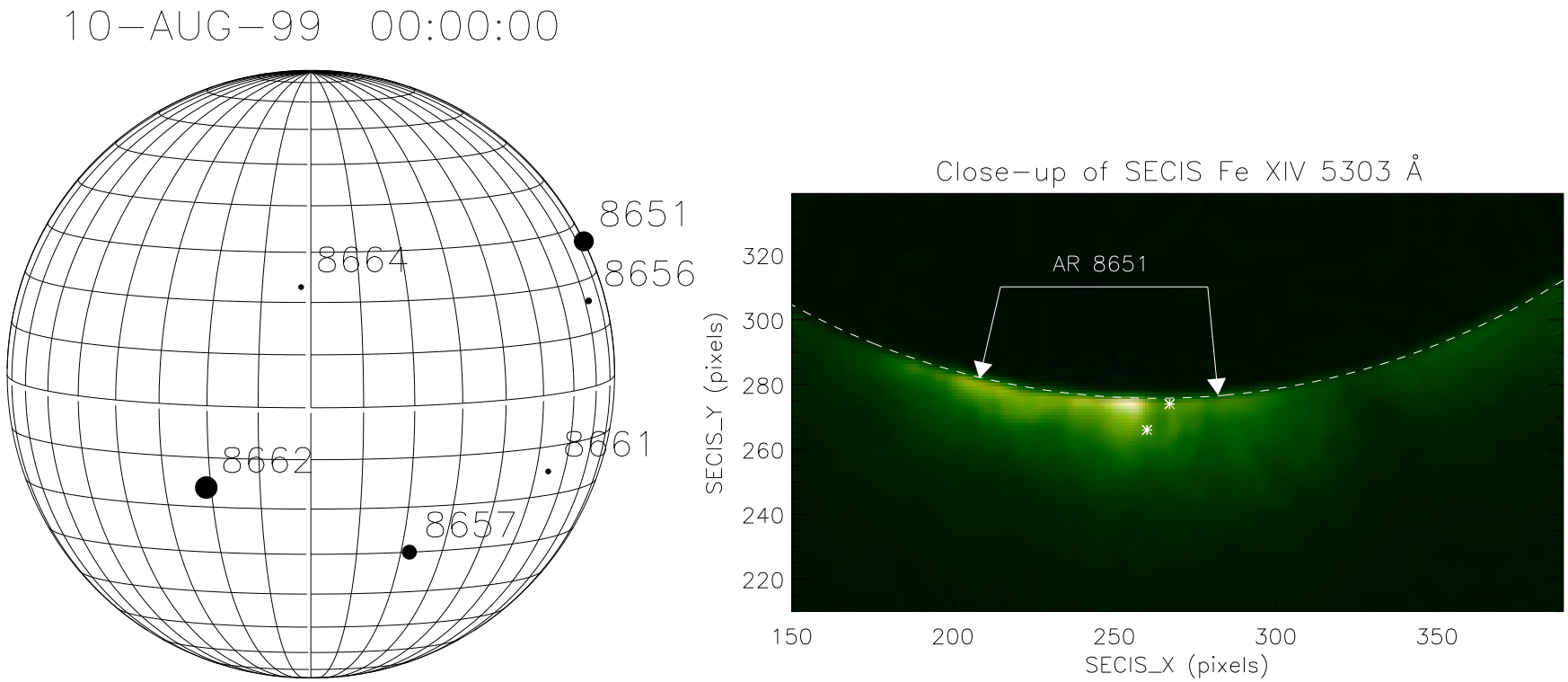

Figure 5.13: Left: active region positions given by the US National Oceanic and Atmospheric Administration. These positions are correct for 00:00 U.T. on 1999 Aug 10, before the west limb passage of NOAA AR 8651, which can be seen as a large circle (representing a large active region area) on the north-west limb. Right: a close-up of SECIS Fe XIV image showing the visible extent of NOAA AR 8651. Asterisks denote the extremities of the structure which is most prominent, and therefore chosen for analysis in this chapter.

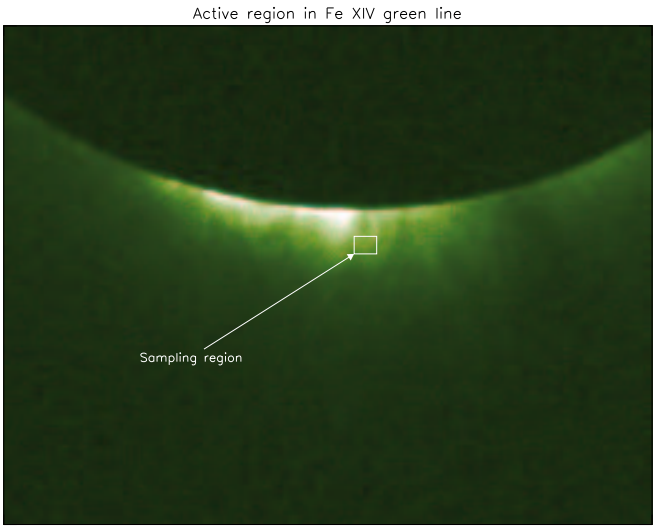

Figure 5.14: Integration box used in creation of Fe XIV and white light SECIS time series. The figure shows only the position of the box in Fe XIV but it is sufficient to describe the location and the principle of the method used.

Arcing between points (267,274) and (260,266) is the most well-defined loop in the Fe XIV sequence, and it is upon this loop that most of our analysis is based. A prime reason for this is the relatively low signal-to-noise in the sequence, compared with that expected, so that structures which are brightest (and easily resolved) are most suitable for our analysis.

Time intervals in the range 3000 – 5000 (67.8 – 113.1 s into eclipse) were chosen for initial analysis because of the relative constancy of the pointing (predominantly smaller scale variations were present, see Figure 5.9). A time series was created by integrating the emission from the loop in a 10×8 pixel^2 box (Figure 5.14), which was sufficient only to cover the loop apex, and none of the neighbouring active region. This was performed in both channels. It was felt that this method would enhance signal-to-noise in the Fe XIV channel. We then compare the wavelet transforms formed from the Fe XIV data with those formed by the white light data; this is distinct from method employed by Williams College teams who divide the Fe XIV intensity by that in the white light channel (Russell 2000, Pasachoff & Landman 1984; Pasachoff & Ladd 1987). Figure 5.15 is a typical arrangement of the plots analysed in this thesis. The figure is divided into three regions, to convey the optimum information with respect

to the wavelet transform and input lightcurve: a) the time series; b) the wavelet *power* transform; and c) the global wavelet transform. The meaning of each of these has already been discussed in §5.3.5.1. The frequency axis is scaled logarithmically from the longest timescale (*i.e.* the lowest frequency) detectable, to the Nyquist frequency, f_N (which in our case is 22.2 Hz).

The resulting wavelet transform (Figure 5.15, main panel) can be described as a cacophony of frequencies. Constant-frequency lines may be drawn along the wavelet transform which correspond to areas of 99% significant power, and in doing this, one finds that these lines match the peaks in the global wavelet spectrum, as expected. These peaks occur (sometimes heavily blended) at the frequencies of 0.5, 0.33, 0.2, 0.08 and 0.05 Hz. The first of these oscillations is most likely a residual resonance of the $X(t)$ and $Y(T)$ pointing functions, and the second can likewise be attributed to $X(t)$. The 0.08 Hz reference can be ignored because its maximum power is held within the cone of influence, while the 0.05 Hz resonance is entirely within the cone of influence and must be discarded. This is something of a shame, since Koutchmy (1984) noted an oscillation at a similar frequency in NSO/Sacramento Peak observations. However, our time series in this case is not sufficiently long to confirm a detection at this frequency. The only remaining resonance worth discussing, therefore, is that at 0.2 Hz. However, this frequency also appeared in the white light series as well, and was considered to be due to sky or instrumental effects.

We can test the validity of wavelet-based detections of oscillatory power by calculating the wavelet power transform for a noisy series, a pure sinusoidal oscillation, a modulated pure sinusoidal function, and a noisy modulated function. Examples of these synthetic data are shown in Figures 5.16 and 5.17. As is apparent, the 99% confidence level used in our analysis is sufficient to prevent spurious, noise-induced detections from being seriously considered, while allowing transient signals, buried in considerable noise (Figure 5.17, right panel) to be detected.

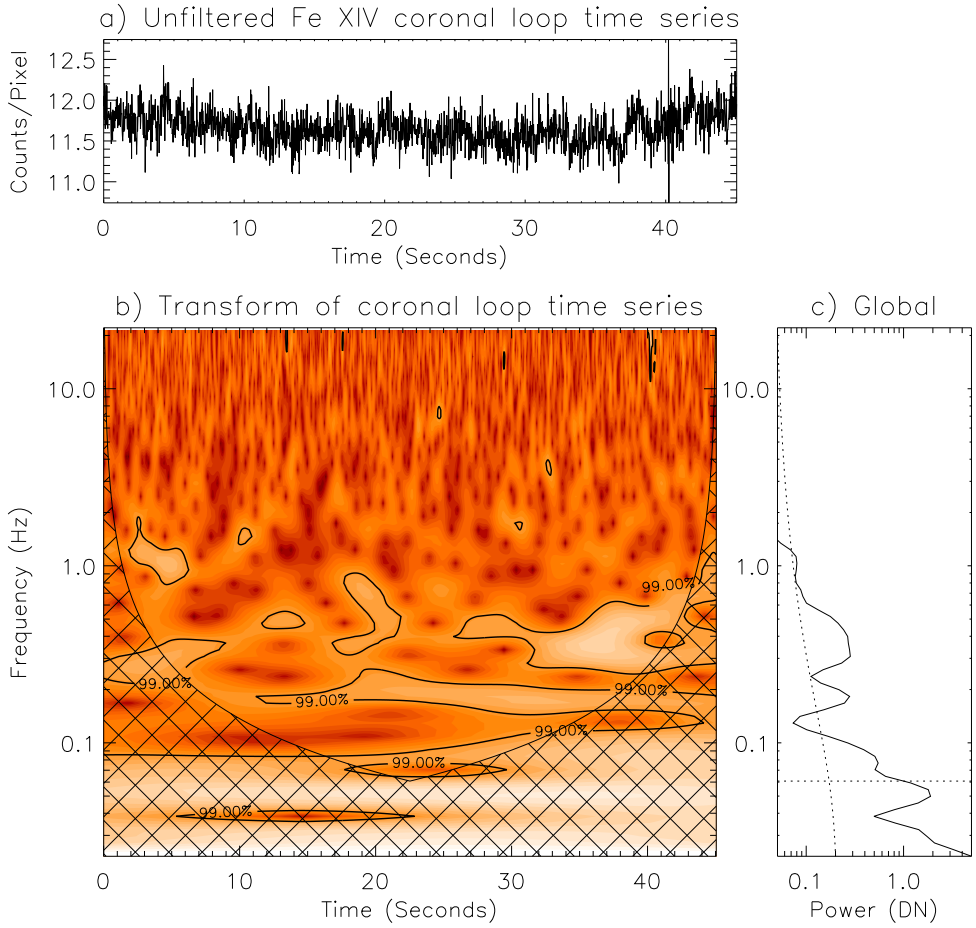

Figure 5.15: a) Time series, b) wavelet power transform and c) global wavelet spectrum of the integration zone defined in Figure 5.14. The combination of detected resonant frequencies in this series can clearly be seen, with peaks in the global wavelet at 0.5, 0.33, 0.2, 0.08 and 0.05 Hz.

As was independently verified by PR, the first 1800 images were eventually found to be those for which the pointing (once corrected) was most stable: accuracy is maintained to within 0.1 pixels. As a result, the first 40 seconds was chosen as the most trustworthy time period during totality from which to make lightcurves. Comparing with the curves of $X(t)$ and $Y(t)$, we see that, although the pointing is not constant on either a small or large scale, the motion on the large scale is not discontinuous, so that it should not, in principle, be any more problematic to remove. A second concern is the rotation of the Sun during eclipse which, although minimal, must still be taken into account so that analysed areas in the image do not rotate away from their original field of view. During 40 seconds, this is not a concern.

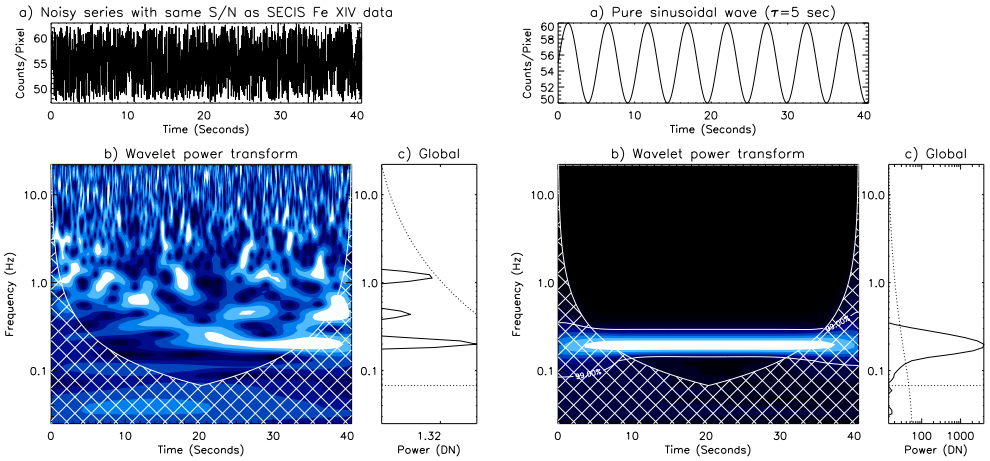

Figure 5.16: Sample control time series used in the investigation of the reliability of wavelet power transforms. Left: a) noisy series with signal-to-noise ratio similar to that of the data created with the `swallowgrid` algorithm (Equation 5.11); b) the Morlet wavelet power transform; c) the global wavelet spectrum. Right: a) a pure sinusoidal wave with τ = 5 s; b) the wavelet power transform; c) the global wavelet spectrum, sharply peaked at 0.2 Hz.

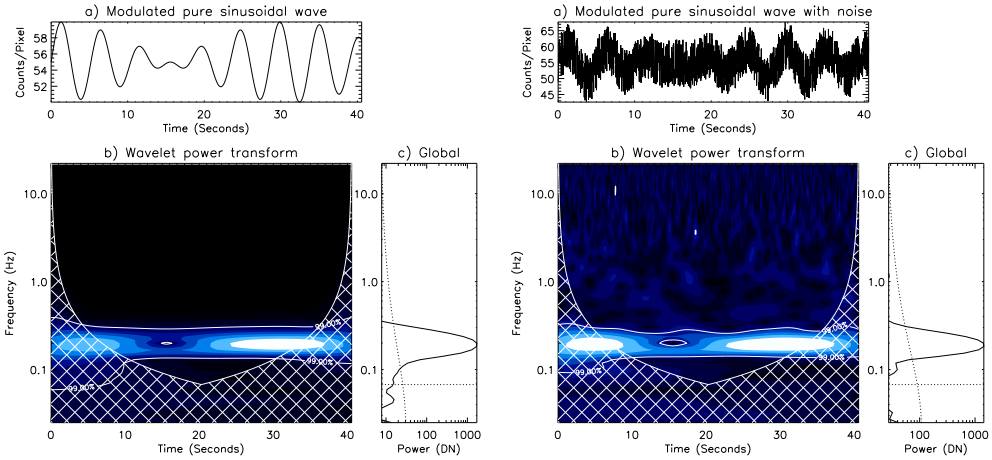

Figure 5.17: As Figure 5.16, but with more realistic synthetic time series showing oscillations which are time-dependent in amplitude (left) and with added noise (right)

An additional problem was that the analysis was too spatially inexact, in that the area being analysed was that around the loop as well as in the area subtended by the loop, in addition to the loop itself, so that signal was in effect being diluted (albeit by regions of much lower intensity). A second problem in our approach was that a search for wave-like behaviour would be hampered by integrating even the intensity from the loop alone. If a standing wave or travelling wave were present, then different parts of the loop would oscillate out of phase with each other, and our initial analysis

method would have ended up analysing a wave with an 'average' dominant phase. It was therefore decided to analyse individual points (*i.e.*pixels) in a 10×10 pixel^2 grid centred about the loop.

Since our efforts concentrate on AR 8651, the region of the SECIS images saved was defined as the rectangular area with X pixels in the range [195, 294] and Y in the range [250,299], *i.e.* a 100×50 pixel^2 area, shown in Figure 5.18. An algorithm known as `swallowgrid` was written to replace the intensity in each pixel, and in each frame, with the sum of the intensity in that pixel and its eight nearest neighbours. The effect of this is to increase signal-to-noise levels, and to reduce the symptoms of CCD interpixel cross-talk, which might otherwise introduce adverse effects into the time series. To illustrate this, imagine that we take an arbitrary 3×3 pixel^2 area of an image, represented by the matrix in Equation 5.11.

$$\begin{bmatrix} V_{x-1,y+1} & V_{x,y+1} & V_{x+1,y+1} \\ V_{x-1,y} & V_{x,y} & V_{x+1,y} \\ V_{x-1,y-1} & V_{x,y-1} & V_{x+1,y-1} \end{bmatrix} \tag{5.11}$$

The `swallowgrid` function operates on the pixel value stored in $V_{x,y}$ and adds the pixel values in the surrounding pixels so that the new signal in this pixel,$V'_{x,y}$ is given by Equation 5.12:

$$V'_{x,y} = \sum_{i=(x-1)}^{(x+1)} \sum_{j=(y-1)}^{(y+1)} V_{i,j} \tag{5.12}$$

The visible effect of this technique is shown by a time-averaged image (averaged over the chosen period of 1800 images) before and after the algorithm has been applied (Figure 5.18). It was felt that the sacrifice of spatial resolution was offset by the increase in signal to noise in the lightcurves, viz. from ~ 13 to ~ 20, with a reduction in the equivalent RMS noise per pixel by a factor of ~ 4. Since we are looking for variations in the intensity from coronal structures, improved signal to noise is certainly necessary. The grid of points used is illustrated in Figures 5.19(a) and 5.19(b), in only the Fe XIV channel. Since the scale of the pixels in white light differs from that of the Fe XIV

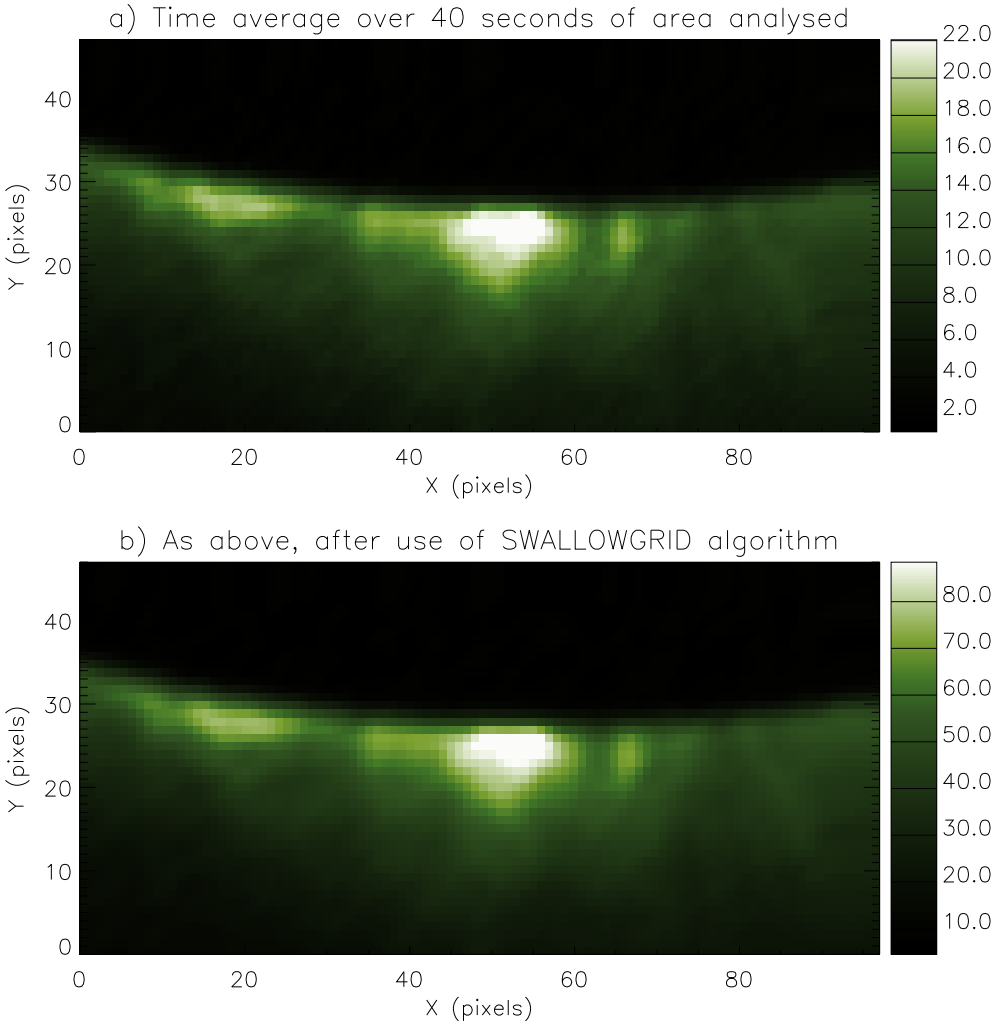

Figure 5.18: a) The zone of primary interest in the Fe XIV sequence, encompassing ARs 8651 and 8656, before and after spatial averaging. b) The same zone after use of the `swallowgrid` algorithm. The effect of the spatial smoothing is discernible, as is the increase in signal level.

channel by less than 1%, alignment of the pixels was not difficult.

5.5 Results & Discussion

5.5.1 Resonant frequency identification

It would be unnecessarily cumbersome to include wavelet analysis plots for all 110 points analysed in our grid. A more useful representation of the data is given in ta-

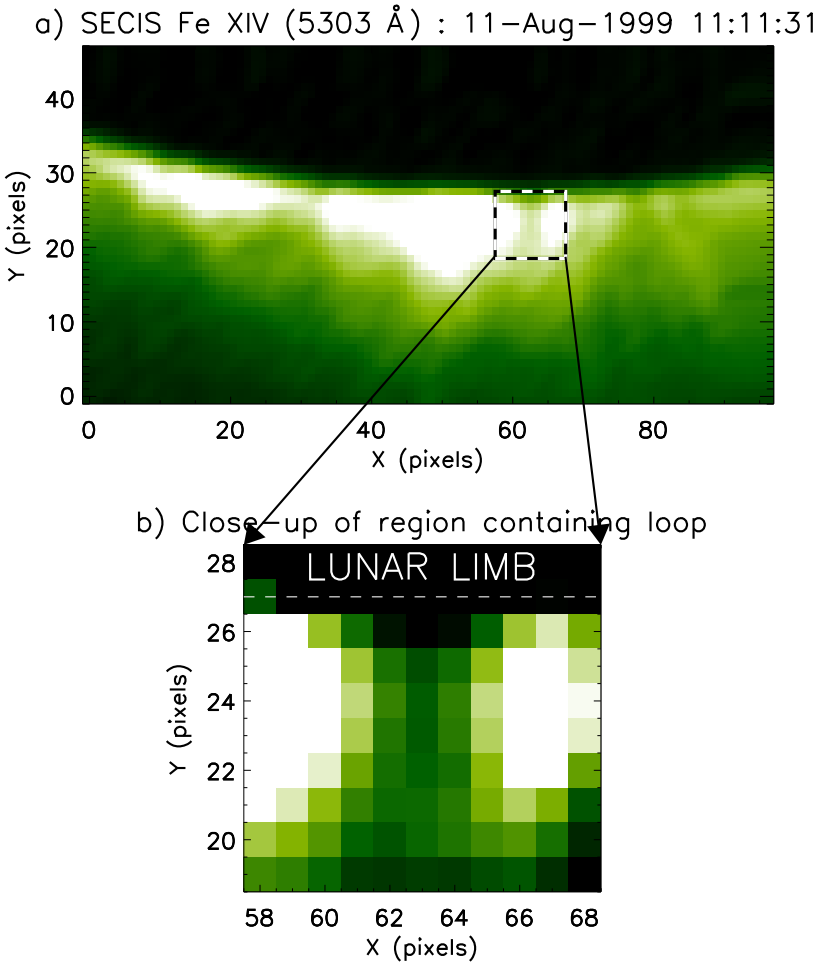

Figure 5.19: a) The position of the grid of pixels, centred on the loop, which were analysed for oscillatory behaviour; b) zooming in on this grid to show the pixel co-ordinates.

ble 5.3: the table gives the frequencies detected at a confidence level of better than 99%. Explicitly, this means that the chance of a spurious detection at any given frequency being caused by stochastic fluctuations in the noise is $\leq 1\%$. This is the only criterion for a detected frequency's inclusion in the table. Dagger superscripts (†) indicate that the data are perhaps suspect since they bleed into the cone of influence where edge effects are expected to become important; double-dagger superscripts (††) indicate that the maximum correlation between the wavelet and time series occurs within the cone of influence, and should therefore be discarded as a detection; thirdly the square brackets indicate that although a resonance was detected at that frequency, it was highly transient, and – as such – may be more to do with a random correlation with noise than

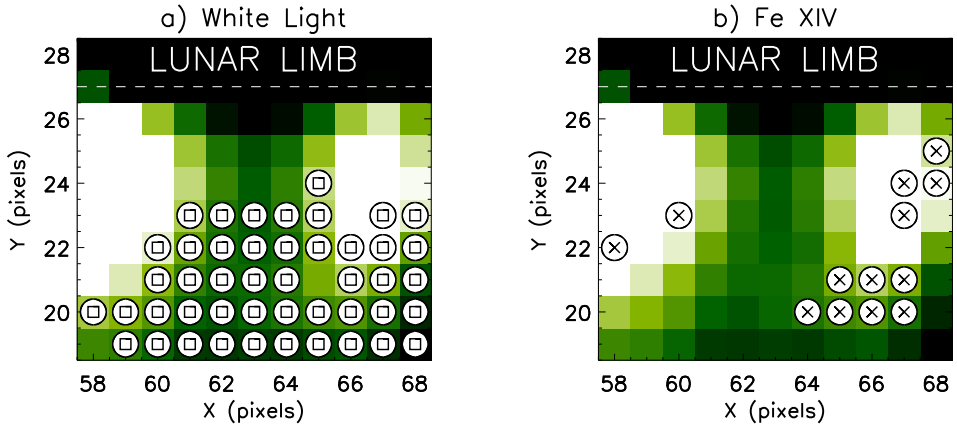

Figure 5.20: a) The locations of all points exhibiting a candidate 0.30 Hz oscillation in the white light series. b) The locations of the 0.16 Hz oscillation in the Fe XIV series. There is no obvious spatial correlation between the 0.30 Hz oscillation and the loop, as it appears rather to occupy a block of pixels.

a true detection. The transient nature of these oscillations is partly a consequence of the shorter scale of the wave packets used by the wavelet transform at higher frequencies. Frequencies which are listed and are *not subject to any of these concerns* are considered as candidates for a real oscillation in the coronal loop vicinity. Examination of Table 5.3 reveals that several points (thirteen in all) exhibit a 0.16 Hz oscillation (*i.e.* 6 second period) which is unique to points on the loop (Figure 5.20a). This frequency is highlighted in bold type. Similarly, there is a frequency of 0.30 Hz which appears to recur in the zone of the loop, as shown in Figure 5.20b. However, this frequency is not claimed as a detection because, firstly, there is no particular spatial correlation with the loop and, secondly, because 0.30 Hz is a resonance of $Y(t)$ (Table 5.2), and cannot be regarded as a trustworthy identification of a resonance. Neither of these is a concern in the case of the 0.16 Hz oscillation. Although some transient oscillations in white light and Fe XIV are associated with loop points, the level of spatial correlation between these points and the loop is not as persuasive as is the case with the 0.16 Hz oscillations in Fe XIV. For this reason the author is reluctant to either confirm or deny the reality of these periodicities as true oscillations of the loop.

Importantly, the duration of the 0.16 Hz oscillation is greater than 20 s, *i.e.* it lasts for at least 3 periods of oscillation. This helps to confirm the reliability of the obser-

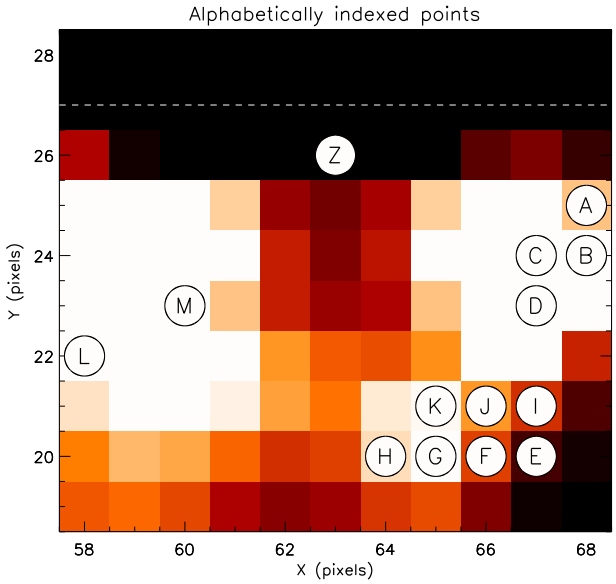

Figure 5.21: Close-up on SECIS Fe XIV images, superimposed with alphabetically indexed points **A** to **M**, which show oscillations in intensity at 0.16 Hz.

vation. To illustrate the nature of the 0.16 Hz detection, each point – marked with an X in Figure 5.20b – which exhibits this periodic intensity fluctuation is denoted by an alphabetical index **A** – **M**, shown in Figure 5.21. Sample wavelet power transforms are then given in Figures 5.22 through 5.25. The additional point **Z** shown in Figure 5.21 is used as a control point to show the wavelet transform for a point in which no unique oscillations were detected.

Also noteworthy is the fact that these oscillations also show up in fast Fourier transform (FFT) analysis. As pointed out (Conway 2001), a detection of oscillatory signal in a wavelet transform may either be a pulse of similar duration to the wavelet packet at that scale (6 seconds in this case), or a genuine oscillation. If it is the latter, then this may be corroborated by a peak in the Fourier power spectrum. An inspection of four such power spectra (Figure 5.26), formed from loop lightcurves, shows this to be the case in our observations, so that we can be sure that we are dealing with a (quasi-)periodic signal.

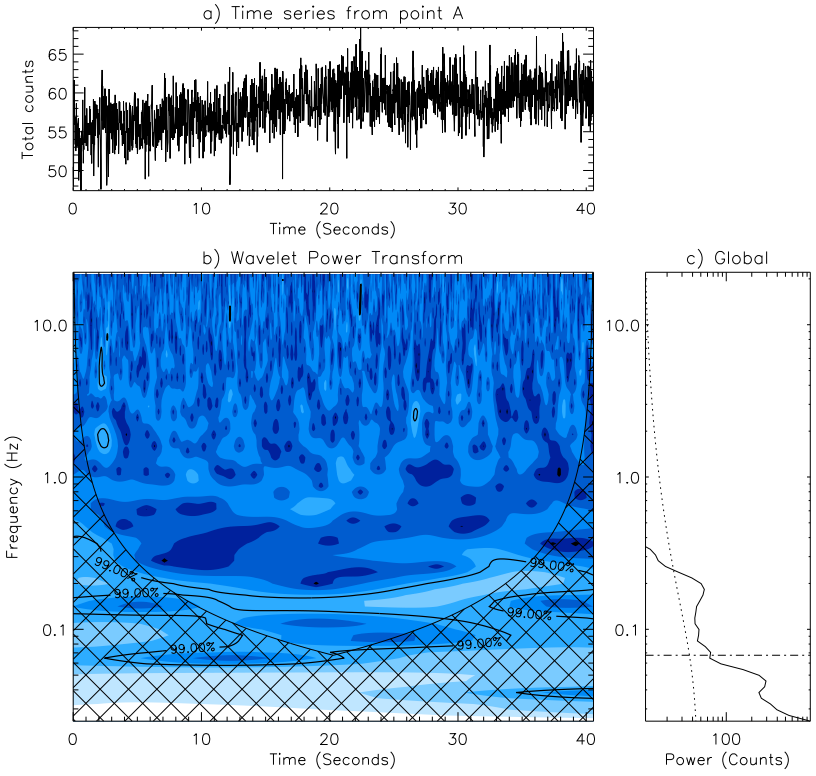

Figure 5.22: Wavelet power transform of the lightcurve centred on point **A**.

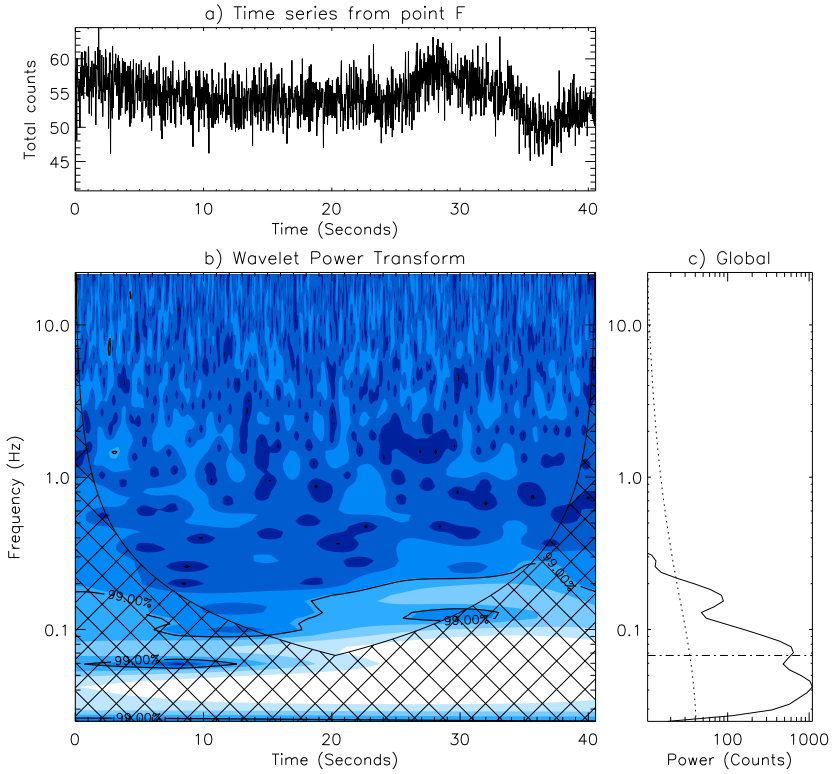

Figure 5.23: As Figure 5.22, but for point **F**.

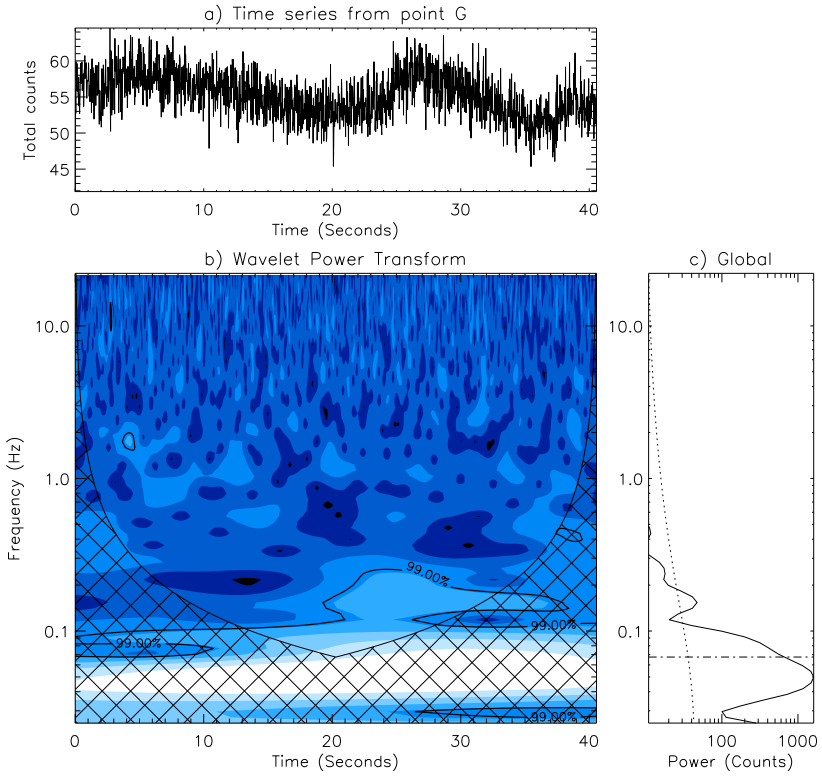

Figure 5.24: As Figure 5.22, but for point **G**.

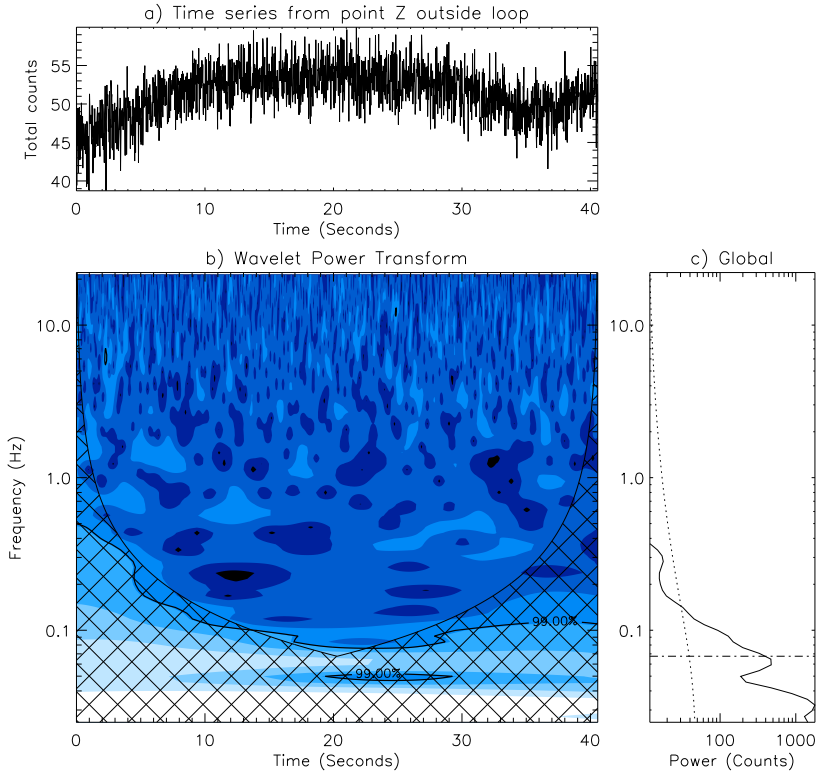

Figure 5.25: As Figure 5.22, but for point **Z**.

Table 5.3: Resonant frequencies detected with wavelet transforms in the SECIS Fe XIV and white light data. † indicates that the oscillation was partially associated in the time/frequency plot with the cone of influence, where edge effects are expected to become important; †† indicates that the maximum power detected at this frequency was inside the cone of influence, and is therefore highly suspect; square brackets around a detected frequency denote a highly transient oscillation.

Co-ordinates		Frequencies detected in Fe XIV (Hz)			Frequencies detected in white light (Hz)			
X	Y							
58	19	0.21†			0.23†			
	20	0.17††			0.077††	0.12††	0.30	
	21	0.16††	0.41††		0.083††	0.20†		
	22	**0.15**	0.22†	0.27†	0.41††			
	23	0.33			0.11††	0.16†		
	24	0.11††			0.19††			
	25	0.11			–			
59	19	[0.25]			0.19††	0.30		
	20	–			0.19	0.31		
	21	[0.42]†			0.21†			
	22	0.093††	[0.27]		0.22†			
	23	0.10	0.23		0.11††	0.18††		
	24	0.12††	[0.22]		–			
	25	0.12††			–			
60	19	[0.26]			0.19††	0.30		
	20	0.21††			0.30	0.20†	0.10††	
	21	–			0.098††	0.23†	0.30	
	22	–			0.096††	0.30		
	23	**0.16**			–			
	24	0.085††	0.19		–			
	25	0.19†			–			
61	19	–			0.21††	0.29††		
	20	0.16††			0.13††	0.30		
	21	0.27†			0.11††	0.28		
	22	–			0.11††	0.17	0.29	[0.68]
	23	0.15††			0.18††	0.29		
	24	0.19†			–			
	25	0.18	[0.50]		–			
62	19	0.12††			0.087††	0.30	[0.66]	
	20	0.11			0.30			
	21	0.11			0.085††	0.30		
	22	–			0.28	[0.34]		
	23	0.13†	0.48		0.22††	0.29		
	24	0.16††			–			
	25	–			–			
63	19	0.13†	0.30††		0.081††	0.20††	0.29	[1.0]
	20	–			0.12†	0.22††	0.30	
	21	–			0.20††	0.30		
	22	–			0.079††	0.18††	0.30	[1.1]
	23	0.18	0.79††		0.079††	0.29		

continued...

Co-ordinates X	Y	Frequencies detected in Fe XIV (Hz)			Frequencies detected in white light (Hz)				
	24	0.11††			–				
	25	–			–				
64	19	0.10†			0.077††	0.11††	0.16††	0.30	[1.0]
	20	**0.16**			0.15††	0.30			
	21	0.13†			0.15†	0.30			
	22	–			0.13††	0.20	0.30		
	23	0.079††			0.16†	0.21††	0.30		
	24	0.085†			–				
	25	0.14††			–				
65	19	0.18††			0.11††	0.29	[1.1]		
	20	**0.15**			0.20††	0.31	[0.68]	[1.1]	
	21	**0.15**			0.22†	0.12††			
	22	0.075††	0.13†		0.27	[1.1]			
	23	0.085††			0.29	[0.63]			
	24	0.085††			0.29†	0.12††	[0.50]		
	25	–			–				
66	19	0.15††			0.11††	0.30	[1.0]		
	20	**0.16**			0.085††	0.30	[1.2]		
	21	0.12†	**0.17**		0.29	[0.63]	[1.0]		
	22	0.28†	[0.35]		0.16††	0.30	[0.68]		
	23	0.085	0.26	0.35	0.19††	0.20	[0.66]		
	24	0.11†			–				
	25	0.11			–				
67	19	0.16††	[0.35]		0.31	[0.61]			
	20	**0.16**			0.30	[0.63]	[1.3]		
	21	**0.15**			0.30	0.43†	[1.1]		
	22	0.18†	[0.38]		0.17††	0.30	[0.65]		
	23	0.11†	**0.16**	[0.38]	0.19†	0.30	[0.62]		
	24	**0.17**			0.12††	0.22††			
	25	–			–				
68	19	–			0.31				
	20	0.16††			0.30				
	21	0.18††			0.22††	0.30	[1.4]		
	22	0.13			0.11††	0.19††	0.30		
	23	0.12††	[0.38]		0.11††	0.20†	0.31		
	24	**0.16**			0.12††				
	25	**0.15**			–				

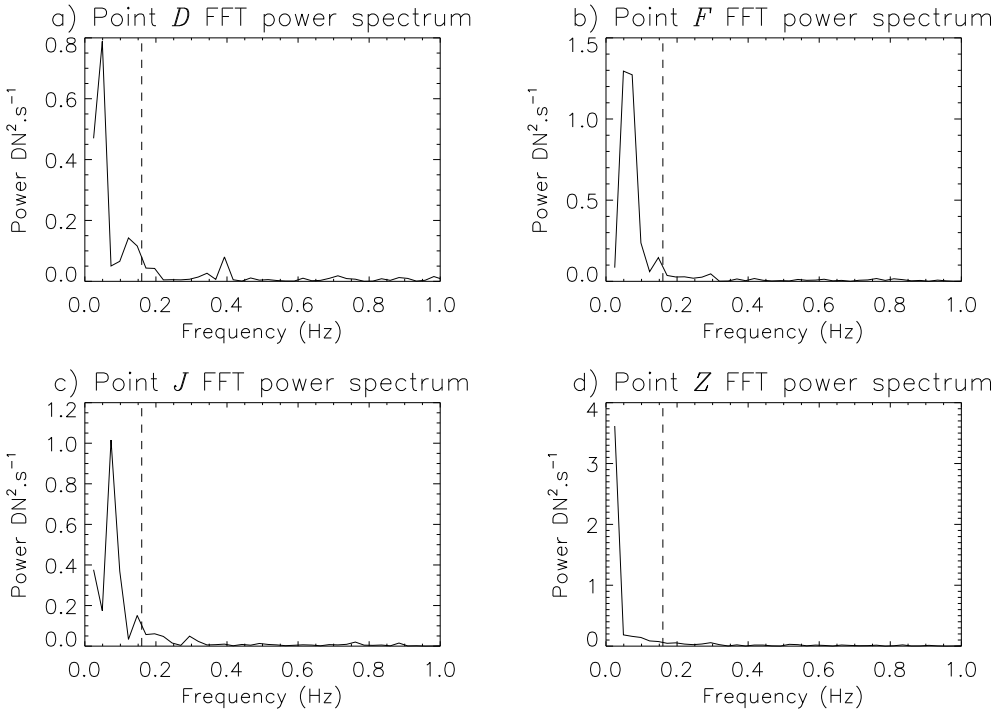

Figure 5.26: a) – c) Fourier power spectra, between the minimum frequency and 1 Hz, of three points where the loop oscillation is detected with SECIS; d) and a fourth point (**Z**) where the oscillation was not detected. The dashed vertical line in each plot is drawn at a frequency of 0.16 Hz, and there is some variation about this value. Point **Z** shows no resonances at any frequencies, as expected.

5.6 Discussion

The identification of an oscillation with a frequency unique to a coronal structure is in keeping with the idea of Alfvén resonance in a coronal structure (or an ideal structure, at least), where the conditions in the loop – N_e, T_e, etc. – are uniform from one footpoint to the other. Qualitatively, observations in keeping with our own have been made by Ireland, De Moortel & Walsh (2000), and DeForest & Gurman (1998) in both closed and open magnetic structures. De Moortel *et al.* (2000) found evidence of oscillations in the period range 180–420 s in a loop structure observed with the *TRACE* satellite in the Fe IX/X λ171 Å band, also using wavelet analysis as their frequency-domain search tool. DeForest & Gurman (1998) found evidence of oscillations on a longer timescale, with periods in the range 600–900 s, in plumes at the solar poles. They analyse the intensity as a function of time at points along the plumes, and make use

of running difference images to find periodic brightenings, with amplitudes of around 15% of the total intensity. These observations were obtained with EIT, again in the λ171 Å passband, and thus looking at the 1 MK corona.

The results which we obtain in the chosen coronal loop with the Fe XIV channel ($T \sim$2 MK) indicate an oscillatory variation in intensity with period 6 s, and peak-to-peak variation of ∼5.5%. These observations are comparable in frequency to those made by Pasachoff & Landman (1984) and Pasachoff & Ladd (1987) who report on experiments during the 1980-Feb-16 and 1983-Jun-15 eclipses in which 2.5″ and 5″ diameter portions of the green-line corona were observed by fibre-optic probes, and found evidence for enhanced power in the 0.5–2.0 Hz frequency range, similar to the the 0.16 Hz oscillation peak reported here. In the same eclipse as that discussed here, they also find evidence of power enhancements in the 0.75–1.00 Hz range, although in NOAA 8656, to the south of the active region we examine. Even closer in frequency are the enhancements in power detected by Singh *et al.* (1997) during the 1995-Oct-24 total eclipse in India. Looking at a very broad band of the solar spectrum (FWHM ∼500 Å), they find oscillations with periods in the range 5.3 s to 56.5 s.

Since these waves cause modulations in intensity, this opens up three possible explanations: I) the density of the emitting plasma is being modulated (as in an acoustic wave); II) the wavelength of the emitted light is Doppler-shifted along the filter profile; or III) the local temperature is modulating about the peak formation temperature of Fe XIV at 2 MK. The radiative cooling time is given by

$$\tau_{\rm rad} = \frac{3kT_eV}{n_e\Lambda(T_e)} \tag{5.13}$$

where V is the volume of plasma under consideration (cm^3 for the loop in our case) $\Lambda(T_e)$ is the empirical radiative loss function (Rosner *et al.* 1978). As we shall see in the next chapter, this time is much longer than the timescale of our fluctuations (6 s), so temperature modulations are not considered. If the changes are solely due to density variations, then a (slow) magneto-acoustic wave, which causes such modulations, could

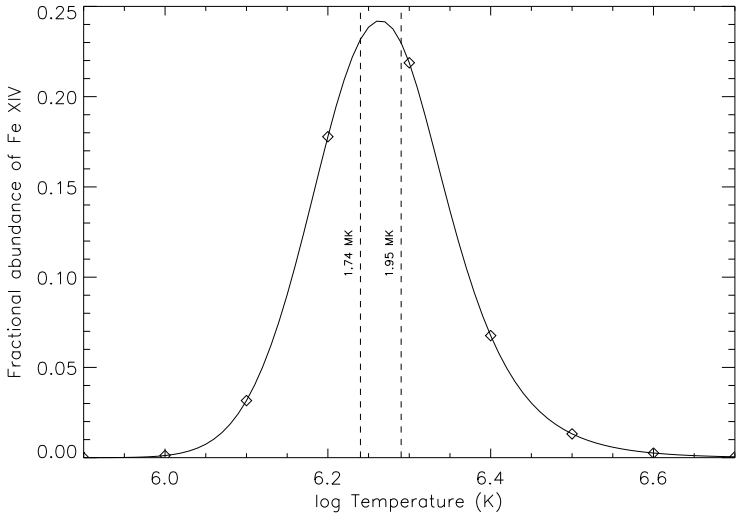

Figure 5.27: Fractional abundance of Fe XIV/Fe as a function of temperature. Data are taken from Arnaud & Raymond (1992) abundances.

well account for the observed changes in intensity. Alternatively, a macroscopic line-of-sight motion of the tube may induce Doppler shifts. Because of the scale of the loop and the short timescale of the oscillations, it is unlikely that we are dealing with a fundamental Alfvén resonance of the loop – equivalent to waves on a tied string. This is not simply because observations with instruments such as *TRACE* have shown that loops are in fact highly inhomogeneous, composed of multitudes of thread-like structures, but also because of the more basic concern that the resonant periods $n\tau$ are limited by

$$n\tau = \frac{2L}{v_{\rm A}}. \tag{5.14}$$

Assuming that the Alfvén velocity is of the order of 1000 km s^{-1}, then our period is substantially shorter than even the 20th harmonic; nor are any other resonances of the (ideal) fundamental period noted.

It is also germane to consider the effects of atmospheric disturbance. Dermendzhiev *et al.* (1992) carried out LIDAR investigations of the atmosphere's transparency in the vicinity of the Fe XIV 5303 Å line using a cadence of 15 s. They found that, near this wavelength, oscillations with frequencies greater than 17 mHz were unlikely to be affected by seeing variations. It is interesting, finally, to note that oscillations with

similar periods have already been detected in hard X-rays and microwaves associated with flare bursts. Kane *et al.* (1983) and Zaĭtsev and Stepanov (1989) observe an 8 second periodicity in closely correlated decaying hard X-ray and 17 GHz radio bursts during the impulsive phase of a flare on 1980 June 7. This may be interpreted as oscillations in the local field due to reconnection during the flare. Similar observations are also reported by M^{c}Kenzie & Mullan (1997).

Porter *et al.* (1994b) suggest that slow-mode waves with frequencies greater than 0.01 Hz can provide adequate coronal heating, while in the case of fast mode waves the required frequencies are in excess of 1 Hz. The frequency of the oscillation detected in Fe XIV falls within the frequency range in which slow-mode waves may cause coronal heating under typical active region conditions.

5.7 Conclusions

To summarise, we find evidence of an oscillation in a non-flaring coronal loop with frequency 0.16 Hz and lasting for $\sim$3 periods above the 99% confidence level. Although detections such as those of Pasachoff & Landman (1984) and Cowsik *et al.* (1997) find enhanced power in similar frequency ranges, our observations represent an isolation of a unique frequency within a solar coronal loop. These observations present strong evidence for short-period oscillations in the corona which, according to recent theory (Porter *et al.* 1994a,b), are required if wave-based heating is to be a viable mechanism for the coronal heating process.

In the following chapter, we analyse the physical conditions in NOAA AR 8651, in particular in the loop analysed here, endeavouring to find out whether this particular oscillation might be responsible for dumping significant energy to its surroundings – perhaps even balancing the locally radiated emission.

Chapter 6

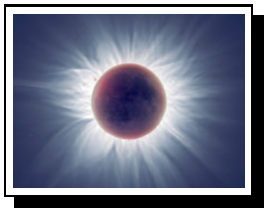

SECIS II: Further Analysis of a Loop Oscillation

This chapter will deal with the interpretation of the oscillatory signature – likely to be a magnetoacoustic wave – discussed in the previous chapter. We carry out a detailed investigation of the timing of the wave-like behaviour in various parts of the loop in which it was discovered. The SECIS *observations were supported by SoHO's Coronal Diagnostic Spectrometer (*CDS*). Using emission line diagnostics we attempt to constrain the local parameters of the plasma, in order to conclude whether the wave observed might itself be responsible for heating the local corona – to be 'caught in the act'.*

6.1 Introduction

In the previous chapter, we discussed the search for short-period oscillations in the solar corona, by analysing the time-dependence of the emission in the coronal green line of Fe XIV during a total solar eclipse. We also reported the detection of such an oscillation, unique to a particular coronal loop structure. In §5.1, we mentioned the disadvantages of using satellite-based data to perform this search. Having said this, we now turn to such data as a means of complementing our ground-based observations. By 1999 August 11, *SoHO* had been recovered after the accident in 1998, during which it had lost contact with its terrestrial control stations. The SECIS team requested support data for the eclipse, from the still-intact CDS instrument. As part of this support, CDS performed an off-limb scan – a doughnut-shaped series of 16 rasters around the Sun to capture the emission of the solar corona in a series of wavelength bands. This scan, made by CDS' Normal Incidence Spectrograph (NIS), was part of the `STRE4W/72` sequence which has wide spectral coverage in the extreme ultraviolet, and is therefore useful for emission line ratio diagnostics, using atomic data from either the QUB $\mathfrak{R}$-Matrix calculations (*e.g.* Mohan, Hibbert & Kingston 1994) or the CHIANTI database (Dere et al.), also accessed through IDL. The CDS wavelength range provides a wealth of spectral lines which can be used as temperature and density diagnostics.

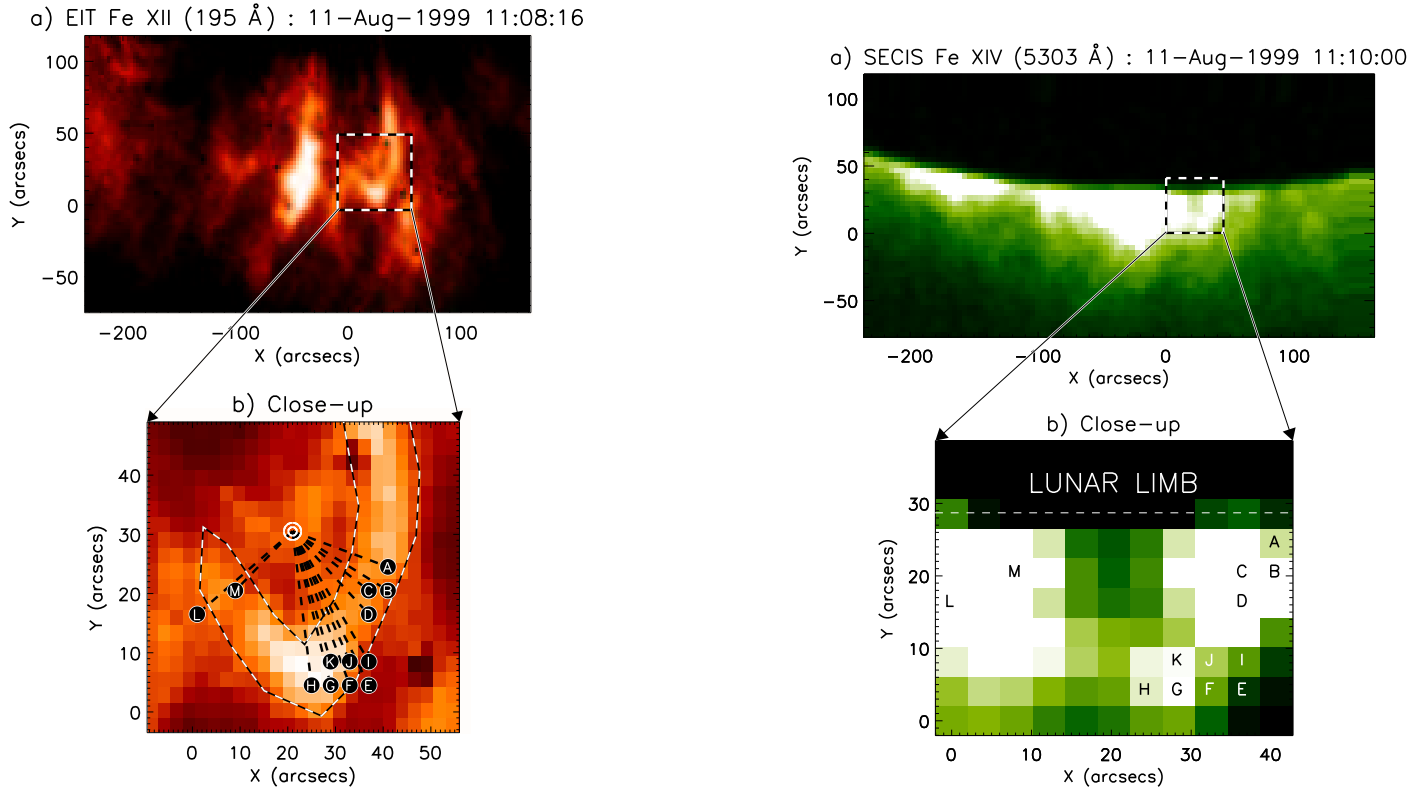

Figure 6.1: Left: a) Prominent loops in active region NOAA AR 8651, as observed in *SoHO*/EIT Fe XII (195 Å). The EIT field of view has been rotated 123° clockwise in order to directly compare it with SECIS images, and the solar limb is approximately 20 arcsec above the top of the given field-of-view. The origin given is the origin of the grid of points, around the selected loop, which were examined for periodicity (Figure 5.21b); b) Close-up on the chosen loop, showing the indexed points at which SECIS detected the 0.16-Hz oscillation. Radials from an approximate centre-of-curvature for the loop apex (indicated by a double white circle) are shown. The angles made by these radials to the horizontal are used to express an *angular* position for each index along the apex. Right: a) A SECIS time-averaged Fe XIV 5303 Å image. The image is an average over 50 consecutive frames (1.1 sec) from the beginning of the sequence, and has been contrast enhanced to better demonstrate the presence of the active region loop chosen for analysis; b) Region of image around the active region loop. The image has been contrast-enhanced.

6.2 Observations of the wave

6.2.1 Wave velocity

It was decided to use the CDS support data because of a discovery in the timing of the wave's intensity maximum at various points along the loop. Figure 6.1 shows a comparison between the EIT Fe XII λ195 Å image – used to determine coronal structure positions and the exact orientation of SECIS – and a time-averaged SECIS Fe XIV λ5303 Å image. Superimposed upon each of these images are the positions of the alphabetical indices at which the 0.16 Hz oscillation was found (§5.4.3). A detailed investigation of the lightcurves of individual points along the loop strongly indicates that the maxima and minima of this oscillation are a function of both position and time. Plotting the intensity at each point as a function of time, as in Figure 6.2, the maximum of the wave's intensity is seen to move along the apex of the loop in an anti-clockwise direction from point **L** (the furthest point clockwise) to point **A**. As discussed in the Chapter 5, we make the assumption that fluctuations in the emitted Fe XIV intensity are caused by density variations, characteristic of an acoustic or (more likely) magneto-acoustic (or 'magnetosonic') wave (Benz, 1993). In order to assess the nature of this wave, and determine its 'mode', it is necessary both to gauge its speed, and to estimate the local magnetic field strength, electron temperature and density in both the loop and the ambient plasma. Our aim is to determine whether such a wave meets the energy and damping criteria required for significant heating of the coronal loop.

In a low-β plasma ($\beta \ll 1$), of which the corona is an example, a wave travelling at a velocity of the order of the local sound speed c_s (typically $\sim$200 km s^{-1}) can usually be classified as a slow-mode magneto-acoustic wave. Similarly, a wave travelling at a speed tending to the local Alfvén velocity v_A (typically $\sim$ 2000 km s^{-1}), will normally be a fast-mode wave.

The fact that the observed wave appears to be moving with time hints that it is

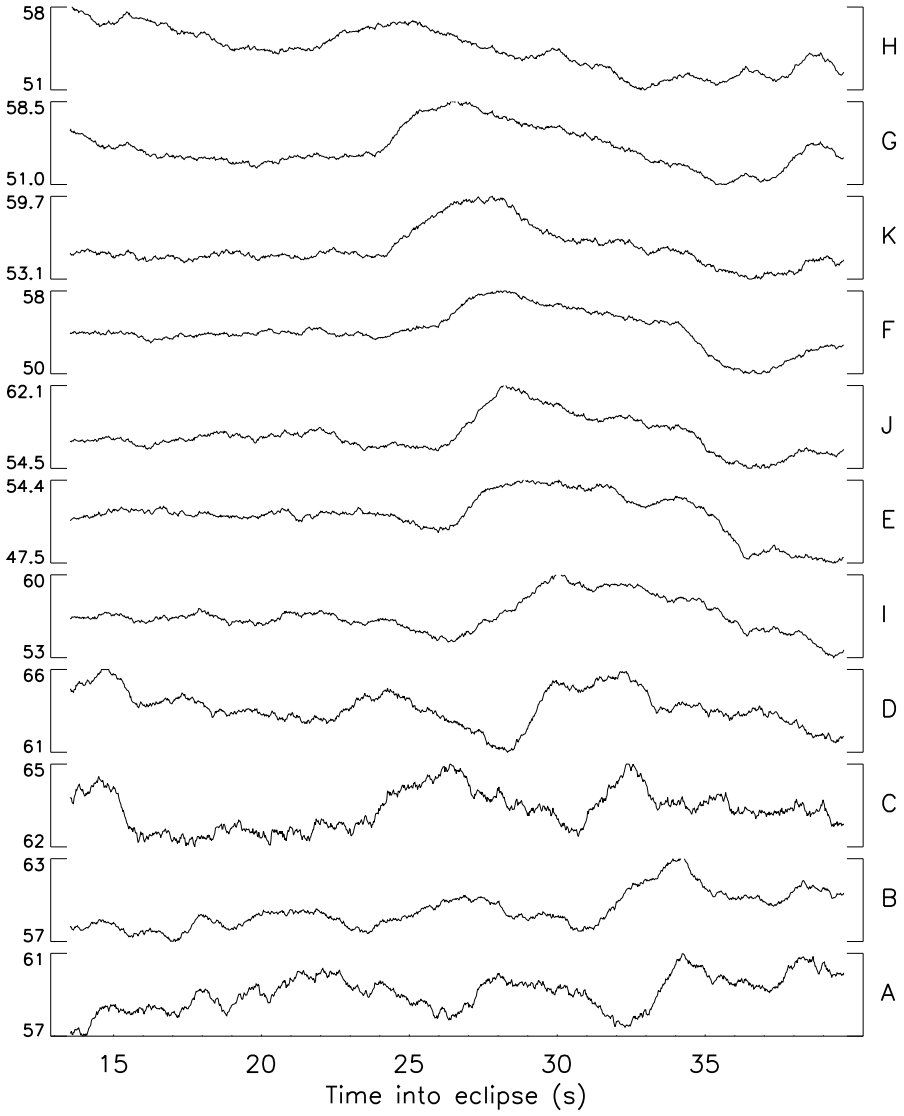

Figure 6.2: Plot of the intensity, in the SECIS Fe XIV channel, at each alphabetical index point (as per figure 6.1) as a function of time after the beginning of the eclipse. Each lightcurve has been smoothed with a running boxcar average of width 1 second. The vertical range on each lightcurve denotes the intensity range of the lightcurve, in counts per exposure. The lightcurves are plotted sequentially according to increasing distance from point **L** along the loop apex. This demonstrates the motion of the peak intensity, whose progress is more quantitatively charted in Figure 6.3.

possible to deduce its group velocity – the speed at which the wave actually transports energy; we use the following procedure to do this. The outline of the loop is determined from EIT Fe XII λ195 Å images and shown in the left panel of Figure 6.1. Plotted over the dotted loop outline are the oscillation's position indices. Lastly, radials (dashed lines) are drawn from each index to an approximate centre-of-curvature (white circles).

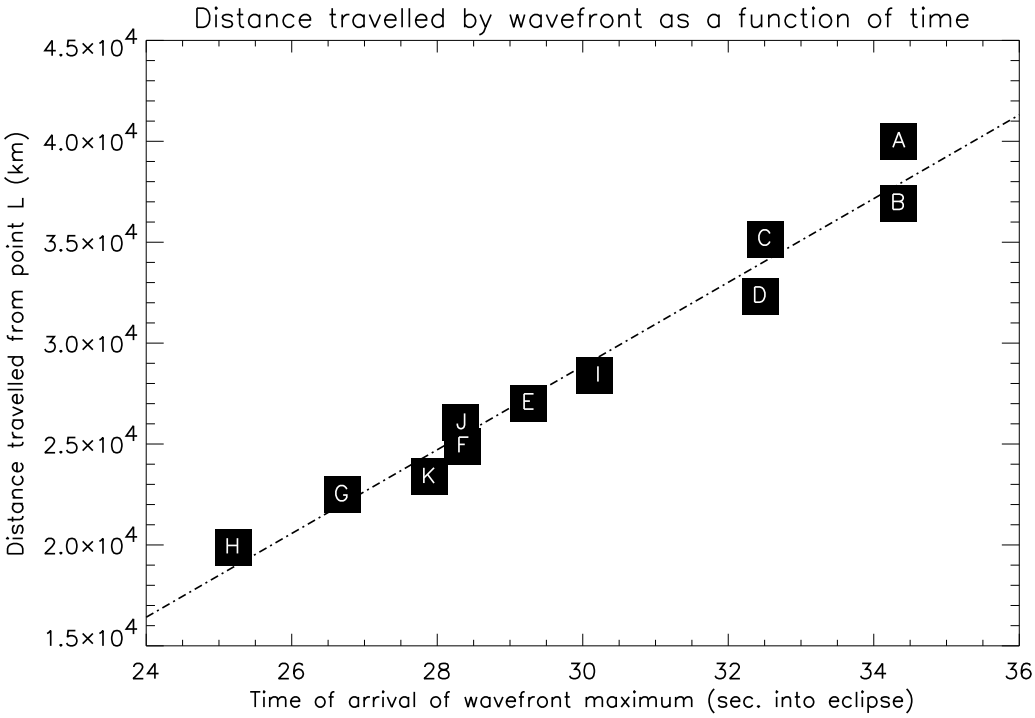

Figure 6.3: Plot of distance travelled by wave maximum along loop from point **L** as a function of time after the beginning of totality. The line of best fit through these points is the effective speed of the wave through the loop apex.

The angle made by each line to the radial drawn by point **L** can be taken and assigned to each index as its *angular* position, θ.

Although the wavelet power transforms picked up the presence of the 0.16 Hz oscillation in all of the indexed points, the maxima of the wave are much more clearly seen in points **A** to **K** than in points **L** and **M**, so we will use the former points to deduce the wave's speed. Since $l = r\theta$, an average radius from the centre-of-curvature is necessary to deduce each point's distance along the loop from point **L**. Additionally, as we are concentrating on points **A** to **K**, we take the average length of only these points' radials, which gives a value of 1.8×10^4 km (25 arcsec). Using this radius of curvature, we find each point's distance along the loop from **L**. The time of arrival of the wave's maximum intensity, $t_{\max}$ is defined as the time – during the interval 20 s $< t <$ 40 s – when the maximum intensity is reached. Each point's distance along the loop is plotted against $t_{\max}$ in Figure 6.3. This produces a straight line whose gradient gives the group velocity of the wave, $v_g = 1900$ km s^{-1}.

The derived value for the velocity is very similar to typical values for the coronal Alfvén velocity v_A. This is a strong indication that the wave is likely to be a fast-mode MHD wave. Pure Alfvén waves will not cause either the temperature or density variations needed to modulate the coronal green line intensity. However, a simple supposition that this is the local fast-mode speed is inappropriate when we have at our disposal a means for diagnosing the local plasma.

6.2.2 Wave phase

Figure 6.4 shows the phase of the wave at the various indices along the loop. It must be said that, like the Fourier power spectra in Figure 5.26, these phases are averaged over the 40 s of the input time series. As such, they represent a snapshot of the wave along the loop. We use the real and imaginary components of the discrete Fourier transforms $\mathcal{F}(\omega)$ of the alphabetically indexed lightcurves to calculate the time averaged phase $\overline{\Phi(\omega)}$ according to

$$\tan\overline{\Phi(\omega)} = \frac{\Im[\mathcal{F}(\omega)]}{\Re[\mathcal{F}(\omega)]} \tag{6.1}$$

where $\Re[\mathcal{F}(\omega)]$ and $\Im[\mathcal{F}(\omega)]$ are the real and imaginary parts of $\mathcal{F}(\omega)$, respectively; the phase angle is calculated between -180° and 180° using the signs (-ve or +ve) of $\Im[\mathcal{F}(\omega)]$ and $\Re[\mathcal{F}(\omega)]$. Since the period of phase (*i.e.* phase velocity wavelength, λ_{ph}) along the horizontal axis in Figure 6.4 is equal to the wavelength calculated above from the group velocity v_g, then we can say that the phase and group velocities of the wave are equal, to a very good approximation.

6.2.3 Local plasma diagnostics

As stated in Chapter 5, the loop we examine is partially obscured by a prominence and neighbouring loops, to the extent that only the northern leg of the loop is observable to us. To examine the local plasma conditions, we use two CDS/*NIS* rasters which

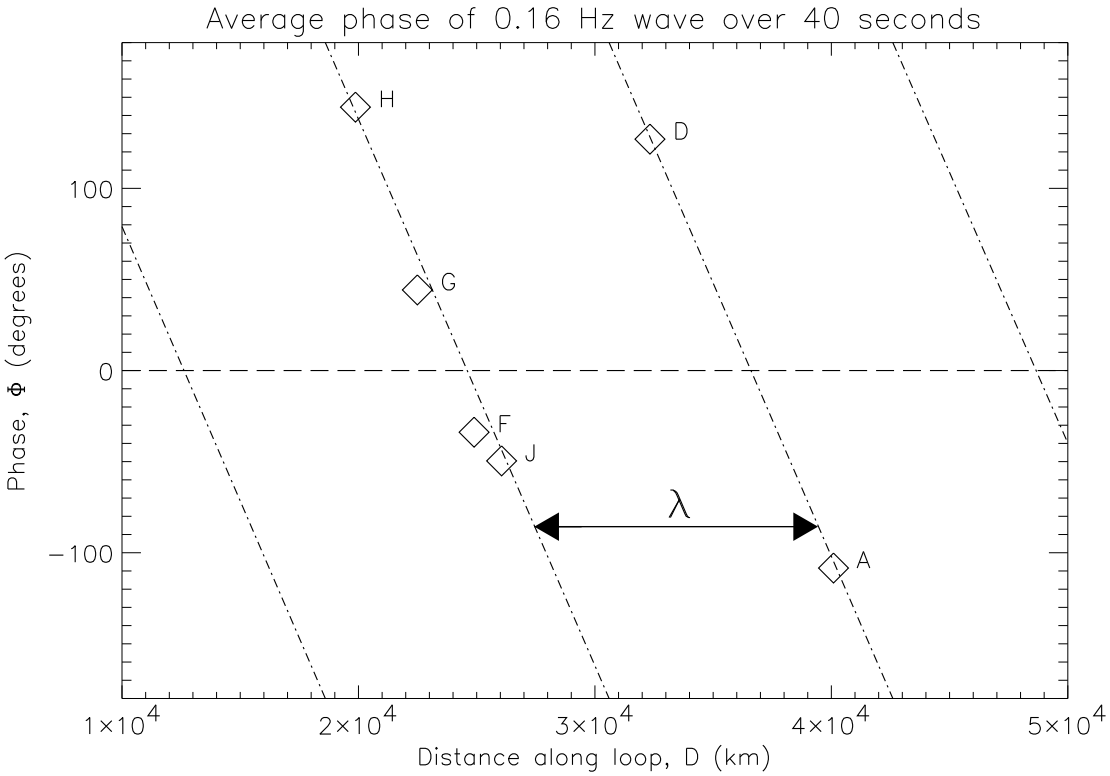

Figure 6.4: Plot of the wave phase (in degrees), time-averaged over the 40 s of observation, according to Equation 6.1. Since $-180^\circ = \overline{\Phi} = 180^\circ$, phase has a 'wrap-around' effect at these values, and the dash-dot lines plotted along the points can be thought of as a single line. The important point to be noted is that the period of this wrap-around is 1.2×10^4 km, which is exactly the wavelength calculated for the observed 6-second wave. Additionally, the phase decreases with distance along the loop $\left(\frac{\mathrm{d}\overline{\Phi}}{\mathrm{d}D} < 0\right)$, which is consistent with wave propagation in the positive *D* direction.

overlap spatially in the region of the loop (Figure 6.5). The 'lower' raster is centred on heliographic co-ordinates (900″, 500″) and was taken at ∼17:00 U.T. with filename *s17196r00*; the 'upper' raster, taken at ∼18:00 U.T., was centred on (N800″, W650″), with filename *s17197r00*. We use the temperature-sensitive, but density-insensitive, line ratio of Fe XIV (334.2 Å) / Fe XIII (348.2 Å) (Brosius *et al.* 1994) to determine a temperature within the loop. This method relies on the use of empirically derived parameters α, β and γ, giving:

$$\log T = \alpha + \beta R^{\gamma} \tag{6.2}$$

$$R = \frac{F_{334}}{F_{353}} \tag{6.3}$$

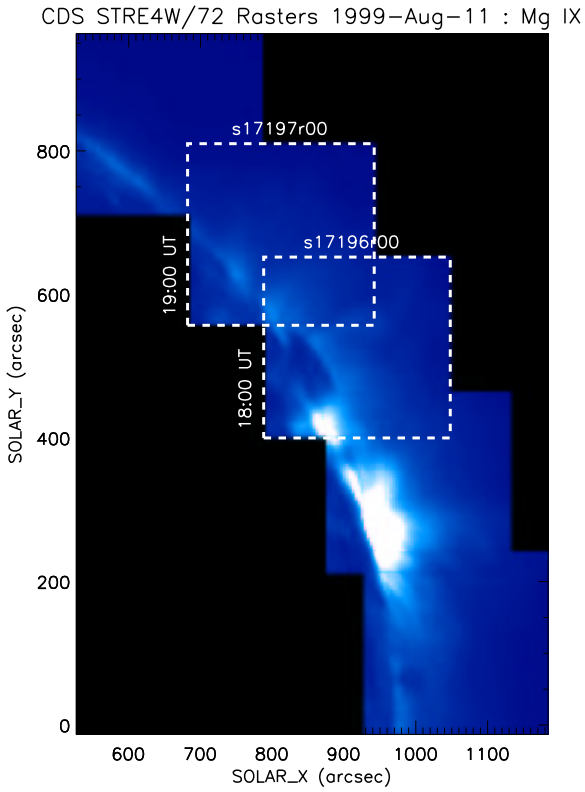

Figure 6.5: Mosaic of two STRE4/72 CDS rasters taken in the vicinity of SECIS' field of view on 1999 August 11. The 'lower' (more southerly) raster is the earlier of the two, and was taken between 17:16 and 18:31 U.T. The 'upper' raster was made between 18:32 and 19:47 U.T.. Approximate times are shown to the left of each raster.

where F_{334} and F_{353} are the line fluxes from the 334 Å and 353 Å lines respectively, $\alpha = 5.571$, $\beta = 0.688$ and $\gamma = 0.161$. With this relation we derive a loop temperature of $T_e = 2.5 \times 10^6$ K, with no appreciable variation along its observable length. We also deduce the temperature along a comparable (heliocentric) radial distance outside the loop, but within the same active region. The temperature along this radial is found to be almost identical. We have also used EIT data to infer the temperature of the plasma. Using a bimodal thermal distribution, after the filter ratio technique of Zhang, White & Kundu (1999), we have constructed full-disk temperature maps of the Sun at 12:20 U.T. By taking a profile along the loop – relatively unchanged since the time of eclipse – we have again found a temperature of $T \sim 2 \times 10^6$ K both inside and outside the loop. The temperatures derived by both of these methods are shown in Figure 6.7. It can be seen in this figure that the EIT-deduced temperatures appear to corroborate the

Table 6.1: Spectral windows used in the CDS `STRE4W/72` sequence

Window No.	Target Ion	Target Wavelength (Å)	Spectral Range (Å)	Detector
0	Si XII	520.44	518.128 – 522.786	NIS2
1	Fe XIV	333.53	332.151 – 334.955	NIS1
2	Ca X	558.15	555.797 – 560.470	NIS2
3	Si IX	341.55	340.146 – 342.955	NIS1
4	Si IX	344.29	342.884 – 345.694	NIS1
5	Si X	347.03	345.624 – 348.436	NIS1
6	Si XI	580.95	578.598 – 583.281	NIS2
7	Si IX	349.77	348.365 – 351.178	NIS1
8	He I	585.40	583.046 – 587.731	NIS2
9	Fe XIV	352.52	351.108 – 353.923	NIS1
10	Fe XI	355.26	353.852 – 356.669	NIS1
11	Si X	358.01	356.598 – 359.416	NIS1
12	Fe XVI	360.76	359.346 – 362.165	NIS1
13	Mg IX	367.95	366.539 – 369.362	NIS1
14	Mg X	624.80	622.454 – 627.155	NIS2

result derived from the NIS data. To infer the local density, we use the density-sensitive line ratio of Fe XIV 334.2 Å / 353.8 Å (Figure 6.6) in the CHIANTI database (Dere *et al.* 1997), which samples the same plasma temperature as the green line. Using this method, we find an electron density of $N_e = 2 \times 10^9$ cm^{-3} within the loop, and an external electron density of $N_{e\mathrm{ext}} = 8 \times 10^8$ cm^{-3}. Lastly, we have constructed an emission measure distribution for the loop under consideration based on the following set of the strong emission lines listed in Table 6.2, which are formed over the $10^{5.8}$ – $10^{6.4}$ K temperature range. We then multiply the emission measure distribution with the radiative loss function of an optically thin plasma (Rosner et al. 1978) and derive radiative losses of $E_{\mathrm{rad}} \approx 10^5$ erg cm^{-2} s^{-1} in this temperature range.

Given the time difference between the SECIS and NIS observations, it is important to remember that the derived plasma values can only be used as an indication for the actual conditions during the eclipse (11:10 U.T.). However, we believe that, given the diversity of active regions and the prevalence of 'typical coronal values' in the literature, our approach provides an accurate way for estimating the local conditions which will

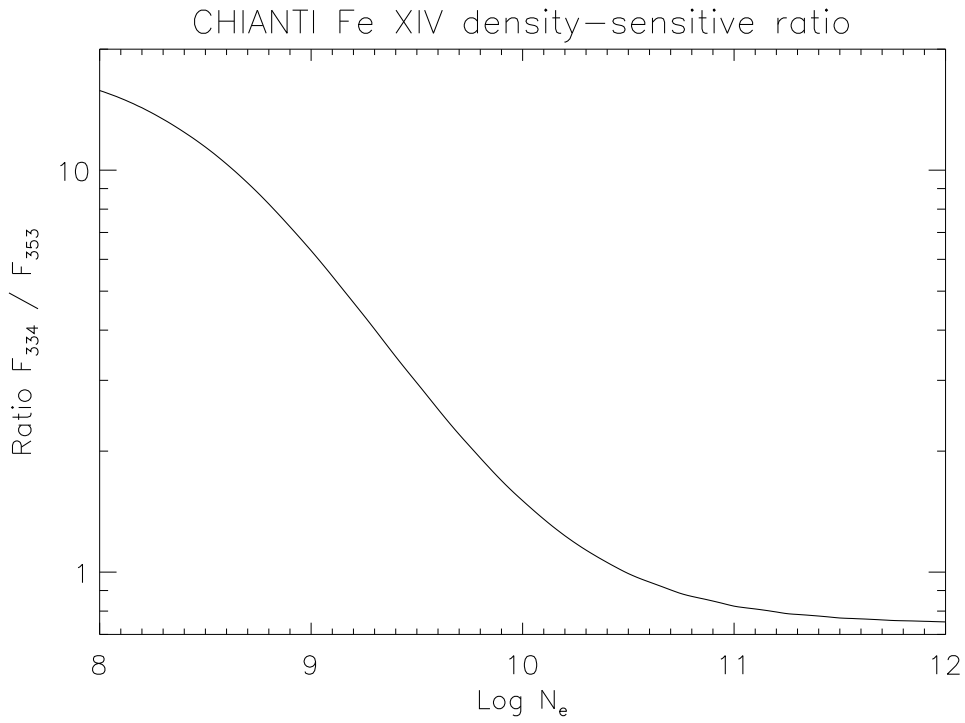

Figure 6.6: Temperature-dependent ratio of emission in the 334.17 Å and 353.83 Å line of Fe XIV.

Table 6.2: Lines used in the loop emission measure distribution. F_U indicates the flux measured in that line in the upper NIS raster and F_L, that in the lower raster.

Ion	λ_{theo} (Å)	$\log(T_e)$ (K)	F_U (10^{20} erg.s^{-1})	F_L (10^{20} erg.s^{-1})	Transition
Ca X	557.77	5.8	2.57	2.43	$3s^2S_{\frac{1}{2}} - 3p^2P_{\frac{3}{2}}$
Mg IX	368.07	6.0	31.0	27.0	$2s^2\,{}^1S_0 - 2s2p^1P_1$
Si X	347.40	6.1	2.95	2.86	$2p\,{}^2P_{\frac{1}{2}} - 2s2p^2\,{}^2D_{\frac{3}{2}}$
Fe XIV	353.83	6.2	5.74	6.12	$3s^23p\,{}^2P_{\frac{3}{2}} - 3s3p^2\,{}^2D_{\frac{5}{2}}$
Fe XVI	360.76	6.4	56.4	45.4	$3s^2S_{\frac{1}{2}} - 3p^2P_{\frac{1}{2}}$

in turn be used to identify the physical processes within the loop.

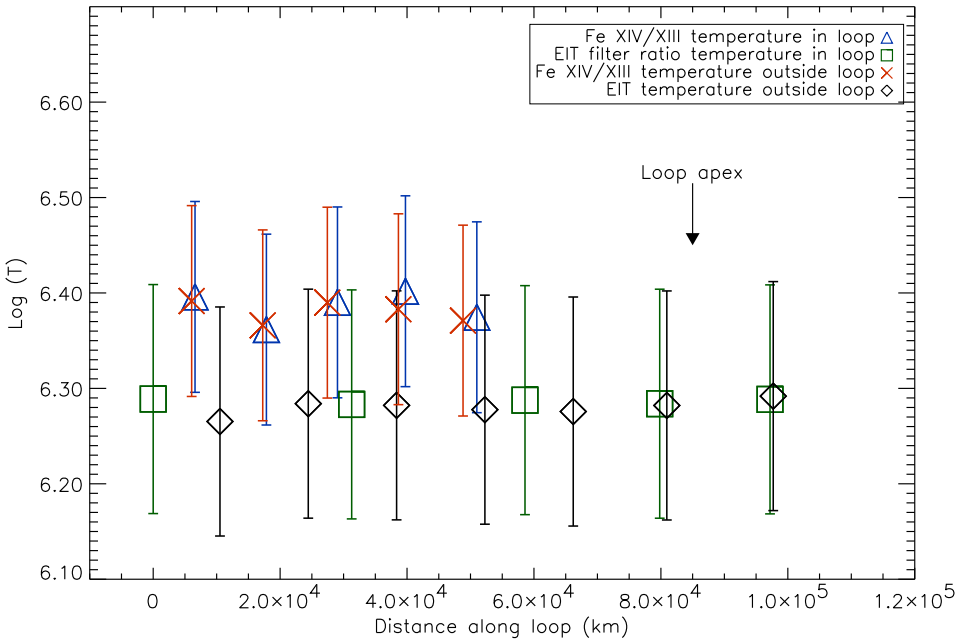

Figure 6.7: Temperature of the loop determined from CDS and EIT data taken on 1999 August 11. The squares represent the temperature along the loop, and diamonds the temperature outside the loop, as calculated from EIT filter ratios, one hour after eclipse. The triangles denote temperatures within the loop derived from CDS measurements of the Fe XIV/Fe XIII ratio, while crosses represent the temperature calculated outside the loop along a parallel path. A small systematic difference in the values of temperature between the two methods is due to the different ions and techniques involved.

6.3 Dissipation of wave energy

6.3.1 Criteria for damping

Before we examine the criteria for damping in detail, we need to clarify some of the assumptions that we use. We assume that the loop is of fixed radius (3×10^8 cm), of constant temperature (2×10^6 K) and density (2×10^9 cm^{-3}), i.e., we ignore any density scale height. Additionally, we neglect the effects of loop curvature at the apex (Smith, Roberts & Oliver 1997), and assume that the conditions in the loop and its neighbourhood have not changed in the few hours between the *SoHO* and SECIS observations. Finally, we assume that the wave in the loop is a fast-mode wave, since it travels at a velocity well in excess of the local sound speed, $c_s \sim$200 km s^{-1}.

Laing & Edwin (1995a,b) set out a number of conditions for effective damping

of waves in coronal loop geometries, which will be examined in the context of our observations. They first assume a loop radius in the range $10^8 < a < 10^9$ cm. Since MHD treatment of a plasma relies on it being a fluid, rather than individual particles, they suppose that the wave is supported by a collisionally dominated plasma, with timescales of change being slower than the collision time, i.e.,

$$\tau > \left(\frac{4.7 T^{\frac{3}{2}}}{N_e} \right) \approx 6.5 \text{ s} \tag{6.4}$$

where τ is the period of the wave in seconds. Since the observed loop has a radius of $\sim 3 \times 10^8$ cm, and the wave has a period ~ 6 s, we will apply their findings to our observations. A critical parameter that we have to consider is the length of the loop, which we take to be $l_{\rm loop} = 2\ l_{\rm leg} \simeq 2.5 \times 10^{10}$ cm, where $l_{\rm leg}$ is the observed length of the northern, visible leg i.e., the loop half-length. The wave observed in Figure 6.2 has a velocity of $\sim 2 \times 10^3$ km s^{-1} and a period of 6 seconds, while the sound speed for a plasma with $T = 2 \times 10^6$ K and $N_e = 2 \times 10^9$ cm^{-3} is $\sim 2 \times 10^2$ km s^{-1}. The fluctuations of the local plasma density imply that the wave has acoustic properties and we therefore suggest that this is a fast-mode wave travelling at a speed near the local Alfvén speed, $v_{\rm A}$. We use the relation given by Habbal, Leer & Holzer (1979) and Wang (2000) for the fast-mode wave velocity, $v_{\rm f}$:

$$v_{\rm f}^2 = \frac{1}{2} \left[v_{\rm A}^2 + c_s^2 + \sqrt{(v_{\rm A}^2 + c_s^2)^2 - 4 v_{\rm A}^2 c_s^2 \cos^2\theta} \right] \tag{6.5}$$

where θ is the angle between the wave's k-vector and the magnetic field direction, B_0, and $v_{\rm A}$ is given by

$$v_{\rm A} = \sqrt{\frac{B^2}{4\pi\rho}} \tag{6.6}$$

and ρ is the mass density, equivalent to the product of the proton mass m_p, and electron density N_e for a pure hydrogen plasma. When $v_{\rm A}^2 \gg c_s^2$, as in our case, the above relation reduces to

$$v_{\rm f}^2 \approx v_{\rm A}^2 \tag{6.7}$$

so that the group velocity v_g is given by

$$v_g \approx \frac{\omega}{k} \approx v_A \tag{6.8}$$

where ω is the angular frequency of the wave and k is its wavenumber. We use equations 6.5 and 6.6 to infer a magnetic field strength of ~ 40 G. This value compares very well to coronal magnetic field measurements made by Lin, Penn & Tomczyk (2000). The observed velocity – the speed of the transport of energy – is the group velocity in this fast mode, $v_g \approx v_f$. We then derive the wavenumber, $k \approx 5.1 \times 10^{-9}$ cm^{-1}, and a wavelength of $\lambda \approx 1.2 \times 10^9$ cm. The first condition of Laing & Edwin (1995b) for damping is that the distance travelled by the wave must be $> \lambda/(4\pi)$ for a weakly dissipative plasma. Since our wave travels a distance $> 2 \times 10^9$ cm along the loop apex, it satisfies the above condition.

In the small damping approximation, (viz. $\delta\omega = v_g \delta k$), the dissipation length of the wave is given by

$$L = \frac{v_g}{\Im(\omega)} = \frac{2v_g}{\nu} \tag{6.9}$$

where ν is the damping rate in s^{-1} (Porter *et al.* 1994a). Note that although Laing & Edwin (1995a) give the dissipation lengths – L_k and L_s for the asymmetric (kink) and symmetric (sausage) magnetoacoustic modes, respectively – in terms of J and K Bessel functions, they report good agreement with Porter *et al.* (1994a). The damping rates for ion viscosity and for electron thermal conduction are given, respectively, in s^{-1} (using $T = 10^{6.3}$ K, $N_e = 10^{9.3}$ cm^{-3}, $\omega \simeq 1$ rad) by:

$$\begin{aligned} \nu_{\rm vis}^{\rm fast}(\omega) &\cong \frac{T_0^{5/2}\omega^2 \sin^2\theta}{10^{15.4} B_0^2} \\ &\simeq 1.4 \times 10^{-3} \sin^2\theta \end{aligned} \tag{6.10}$$

and

$$\nu_{\rm cond}^{\rm fast}(\omega) \cong \frac{T_0^{7/2} n_0 \omega^2 \cos^2\theta \sin^2\theta}{10^{28} B_0^4} \tag{6.11}$$

$$\simeq 8.8 \times 10^{-4} \sin^2\theta \cos^2\theta$$

The maximum electron conductivity damping rate will occur for $\cos\theta = \sin\theta$, when $\theta = \pi/4$. This gives $\nu_{\rm vis}^{\rm fast}(\omega) = 7 \times 10^{-4}$ s^{-1}, and $\nu_{\rm cond}^{\rm fast}(\omega) = 2 \times 10^{-4}$ s^{-1} (i.e., $\nu_{\rm cond}^{\rm fast} \simeq 3\nu_{\rm vis}^{\rm fast}$). We therefore end up with a value for the dissipation length:

$$L_{\rm cond}^{\rm fast} \simeq 5 \times 10^{11}\,{\rm cm} \tag{6.12}$$

which is well beyond the length of the loop. It therefore appears that the observed wave does not substantially heat the loop as it passes through it. Even if we include both dissipation mechanisms,

$$L_{\rm total}^{\rm fast} = \frac{2 \times 2 \times 10^8}{9 \times 10^{-4}} \simeq 4 \times 10^{11}\,{\rm cm} \tag{6.13}$$

and so we still have $l_{\rm loop} \ll L_{\rm total}^{\rm fast}$. This value is well in excess of the 4×10^9 cm cited by Laing & Edwin (1995a) as a maximum length for effective dissipation.

6.4 Wave energy density

6.4.1 Transverse waves

We now look at the variation in intensity caused by the wave. This intensity variation represents 5.5% of the total signal, peak-to peak; *i.e.* the amplitude δI of the variation is half of this, so $\delta I/I = 2.75 \times 10^{-2}$.

Theoretical arguments (Hasan & Kalkofen 1999) point to fast-mode oscillations in the corona travelling as transverse oscillations. Since we are observing a loop which appears to be in a plane perpendicular to the line of sight, transverse oscillations of a flux tube, with a line-of-sight component, will be detectable as Doppler shifts in the emitted wavelength of the coronal green line. Additionally, because the filter has the measured

Gaussian shape given in Figure 5.11, the motion of the green line profile towards and away from the filter's central wavelength will cause variations in the intensity detected by SECIS' detectors.

Bearing in mind considerations of the line transmission raised in §5.4.1.1, the line-of-sight velocity u amplitude of this transverse wave can be estimated. The increase in intensity due to this wave is measured to be 5.5%, peak-to-peak, which gives an amplitude $\frac{\Delta I}{I} = 0.0275$. First, a Gaussian filter profile is given by the function

$$\Psi(\lambda) = \frac{A}{w} \exp - \left(\frac{\lambda_F - \lambda}{w} \right)^2, \tag{6.14}$$

where w is the $1/e$ half-width of the profile, $\frac{A}{w}$ is the peak value of Ψ, and λ_F is the central wavelength of the profile. The intensity I of a line after passing through the filter will be $I\Psi(\lambda)$. Using the basic calculus identity

$$\Delta y = \frac{dy}{dx}\Delta x \quad \Rightarrow \quad \frac{\Delta I}{I} = \frac{1}{I}\frac{dI}{d\lambda}\Delta\lambda \tag{6.15}$$

the increase in flux of $\frac{\Delta I}{I}$ is caused by the shift in wavelength $\Delta\lambda$, such that

$$\frac{\Delta\lambda}{\lambda} = \frac{w^2}{2\lambda(\lambda_F - \lambda)}\frac{\Delta I}{I} = \frac{u}{c} \tag{6.16}$$

where c is the speed of light in a vacuum. Estimating the velocity u now becomes a function of the wavelength of the emitted light λ and the central wavelength λ_F of the filter, both of which are uncertain, as well as the filter width w. The energy flux density of a wave along the tube, $E_{\rm fd}$, is then given by

$$E_{\rm fd} = \frac{1}{2}\rho_0 u^2 v_{\rm g} \tag{6.17}$$

(see Laing & Edwin 1995b) where ρ_0 is the mass density of the plasma in the tube.

To illustrate the effect of the variability of λ and λ_F, the parameter space is explored in Figure 6.8.

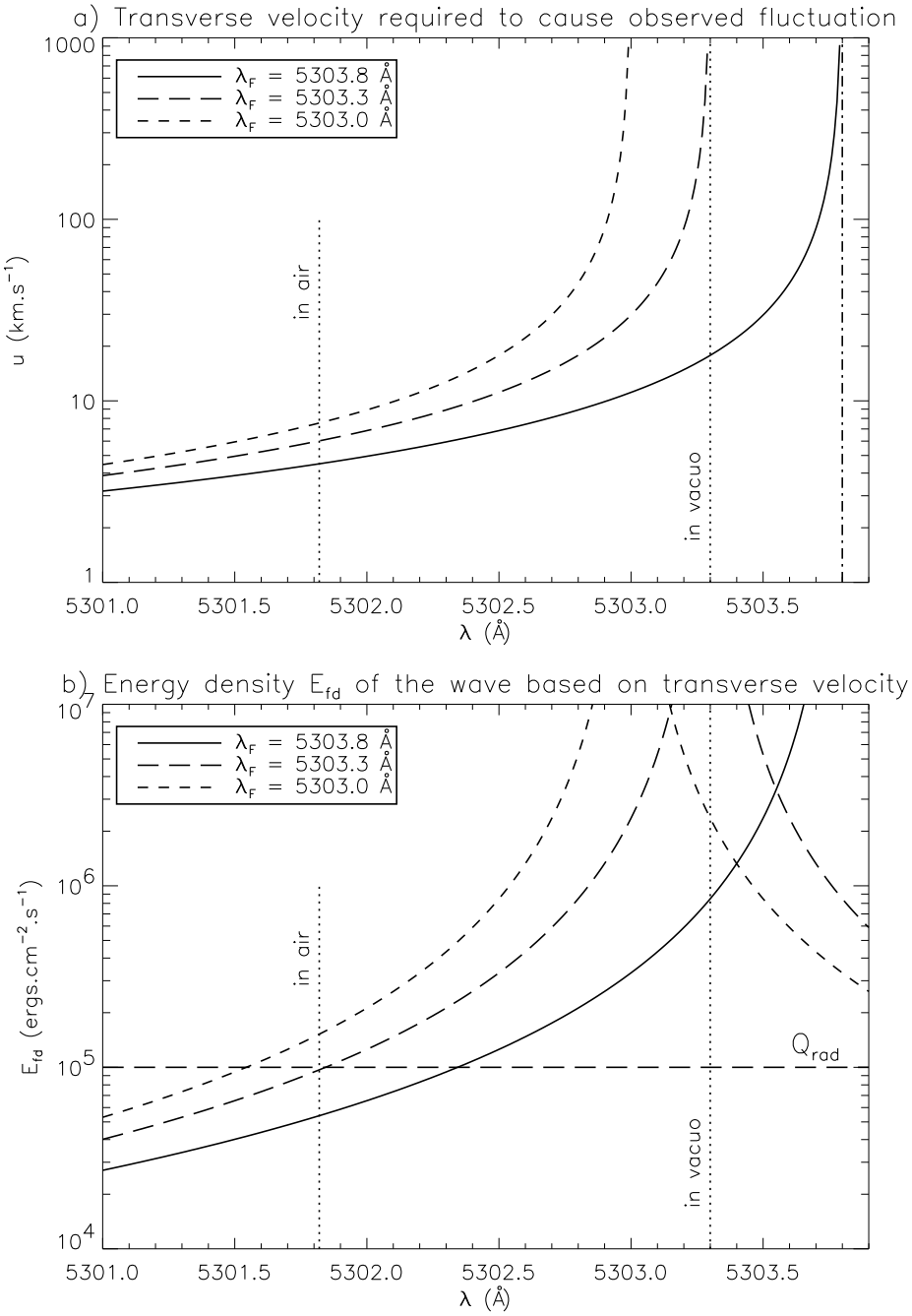

Figure 6.8: a) Plot of the velocity amplitude of a transverse wave required to match the observations. The curved lines are solutions for different positions of the filter central wavelength, λ_F, which is not known absolutely. The vertical dotted lines indicate the probable wavelength of the Fe XIV green line *in vacuo*, and with the -1.48 Å vacuum-to-air correction (§5.1.2). b) Corresponding flux density of the wave for each solution in a). $Q_{\rm rad}$ indicates the level of radiative losses from the loop as calculated from the emission measure (§6.2.3): for the wave to be able to balance the radiative losses, $E_{\rm fd}$ must lie above this value. However, values in a) and b) are for a transverse motion assumed to be entirely along the line of sight – they represent lower limits to u (a) and $E_{\rm fd}$ (b).

Three solutions for the transverse velocity amplitude u are shown in Figure 6.8. The solid line represents the solutions if the filter was angled at 1° from normal incidence, as is most likely the case. However, varying the angle of the filter to the beam adjusts its central wavelength λ_F, thereby adjusting the required value of u. Turning the filter beyond 1° has the effect of reducing λ_F, and hence increasing both u and the energy flux density of the wave, E_{fd}.

These solutions assume, though, that the u is directed only along the line of sight. For an oscillation at an angle θ to the line of sight, u becomes $\frac{u}{\cos\theta}$ and E_{fd}, $\frac{E_{\mathrm{fd}}}{\cos^2\theta}$. The solutions in Figure 6.8 thus represent lower limits to the energy of our supposed transverse wave.

6.4.2 Longitudinal waves

Alternatively, we may look at the interpretation of the wave as a longitudinal sausage-mode wave. In this case, the cross-sectional area of the flux tube is a function of distance and time, and is related to the changing magnetic field strength, by Roberts (1983), as

$$\frac{1}{B_0}\frac{\partial B}{\partial t} = -\frac{1}{A_0}\frac{\partial A}{\partial t} \tag{6.18}$$

where B_0 is the equilibrium field strength, and A the corresponding cross-sectional area of the flux tube, illustrated in Figure 6.9.

However, there are two difficulties with this interpretation. The first is that the wave is largely compressional, so that u is in fact describing the oscillation amplitude of particles in the flux tube in a longitudinal direction. The second is that the velocity of such a wave, again given in Roberts (1983), is the *tube speed* c_T, such that:

$$c_T^2 = \frac{c_s^2 v_A^2}{c_s^2 + v_A^2}. \tag{6.19}$$

The problem is that where $v_A \gg c_s$, the tube speed is controlled by c_s, to which it tends

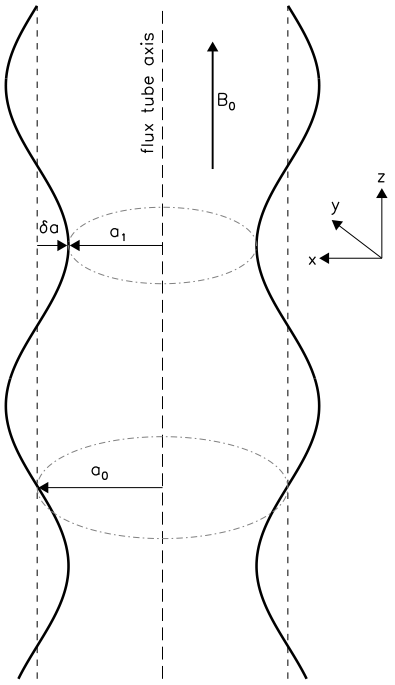

Figure 6.9: Side projection of an idealised flux tube supporting a sausage mode slow magnetoacoustic wave at an arbitrary time, t_1, along the local magnetic field $\mathbf{B}_0$. The radius a_0 represents the mean (or unperturbed) radius of the flux tube and δa represents a propagating perturbation in the radius. Hence, $a_1 = a_0 - \delta a$, with $\delta a = f(x,y,z,t)$.

from *below*. This is more easily identified with a longitudinal slow-mode sausage wave, which cannot easily be reconciled with our observations. In the interests of comparison, we will also examine the alternative scenario, wherein the 6-second oscillation is in fact connected with a slow-mode wave. Slow-mode waves in a magnetic plasma are much more similar to pure sound waves than are fast-mode waves, and the particles are confined to oscillations with a large component of velocity along the local magnetic field direction. We follow the argument below to infer the RMS velocity of the particle oscillations:

Let any given particle have instantaneous, time-dependent displacement, s_i, with amplitude s:

$$s_i = s\cos(kz - \omega t) \tag{6.20}$$

It follows that the local change in pressure Δp_i varies sinusoidally with amplitude Δp

according to

$$\Delta p_i = \Delta p \sin(kz - \omega t) \tag{6.21}$$

where

$$\Delta p = c_s^2 \rho k s. \tag{6.22}$$

Since the particle velocity u_i is simply $\frac{ds_i}{dt}$, then

$$u_i = \frac{ds_i}{dt} = u \sin(kz - \omega t) \tag{6.23}$$

where $u = \omega s$ and it is given that

$$c_s^2 = \frac{\gamma p}{\rho} \approx \frac{\gamma \Delta p}{\Delta \rho} \tag{6.24}$$

for small-amplitude changes in density, $\Delta\rho$. Rearranging the terms, we find

$$\Delta \rho = \frac{\gamma \Delta p}{c_s^2} \tag{6.25}$$

$$\Rightarrow \Delta N_e = \frac{\gamma \Delta p}{c_s^2 m_p} \tag{6.26}$$

$$\Delta N_e = \frac{\gamma c_s^2 \rho k s}{c_s^2 m_p} = \gamma k N_e s$$

where ΔN_e is the amplitude of the variation in N_e associated with the pressure variation (amplitude Δp), so that

$$s = \frac{\Delta N_e}{N_e} \frac{1}{\gamma k}. \tag{6.27}$$

Since the amplitude of velocity oscillations is $v = \omega s$, and $v_g \approx \frac{\omega}{k}$, then

$$u \approx \frac{\Delta N_e}{N_e} \frac{v_g}{\gamma} \tag{6.28}$$

and, in the case of our wave being slow-mode,

$$u_{\text{rad}} \approx \frac{2.8 \times 10^{-2} \times 2 \times 10^7}{\frac{5}{3}}$$

$$= 3.3 \times 10^5 \text{ cm s}^{-1}$$

for radiatively excited Fe XIV emission and

$$u_{\text{coll}} \approx \frac{1.4 \times 10^{-2} \times 2 \times 10^7}{\frac{5}{3}}$$
$$= 1.7 \times 10^5 \text{ cm s}^{-1}$$

in the case of emission dominated by collisional excitation.

The energy flux density of the supposed slow-mode wave can then be calculated from Equation 6.17 to be $E_{\text{fd}}^{\text{rad}} = 3.5 \times 10^3$ erg cm^{-2} s^{-1} or $E_{\text{fd}}^{\text{coll}} = 9.6 \times 10^2$ erg cm^{-2} s^{-1}. To complete our comparison between the two modes, however, it is necessary to compute the probable damping lengths of the wave. The damping rates are again given by Porter (1994a) as

$$\nu_{\text{vis}}^{\text{slow}} \simeq 10^{-0.54} T_0^{\frac{3}{2}} n_0^{-1} \omega^2 \tag{6.29}$$

and

$$\nu_{\text{cond}}^{\text{slow}} \simeq 10^{0.44} T_0^{\frac{3}{2}} n_0^{-1} \omega^2. \tag{6.30}$$

revealing that the viscous ion damping rate in slow-mode waves is systematically smaller than the corresponding damping rate due to electron thermal conduction. Using Equation 6.9, this yields damping lengths of

$$L_{\text{vis}}^{\text{slow}} = 8.1 \times 10^7 \text{ cm} \tag{6.31}$$

and

$$L_{\text{cond}}^{\text{slow}} = 8.4 \times 10^6 \text{ cm} \tag{6.32}$$

respectively, compared with the loop half-length $l_{\text{leg}} = 1.3 \times 10^{10}$ cm. It can be seen that such slow-mode waves would indeed damp very quickly, but would not possess the required energy to balance the radiative losses from the loop (§6.2.3), as a fast-mode wave would. In fact, the wave would dissipate by electron thermal conduction in a

distance $< \lambda/4\pi$, breaking the first constraint of Laing & Edwin (1995a), so that the small damping approximation would break down. In any event, it appears that – in the slow-mode case – all the wave's energy would effectively be lost to the loop in a distance much less than the observed length of the loop apex.

6.5 Results & Discussion

Roberts *et al.* (1984) discuss the properties and evolution of fast and slow magnetoacoustic waves, both standing and impulsively generated. In this context, consider Figure 5.22 which shows the wavelet transform of a time series formed from the intensity at point **A** in Figure 5.21. It can be seen that during the first half of this 40-second time series, the 0.16-Hz frequency oscillation is not detected. Roberts *et al.* (1984) detail the evolution of an impulsively generated fast wave as: 1) an initial periodic phase, beginning at a time $\propto \frac{1}{v_{\rm Ae}}$ after the initial impulse (where $v_{\rm Ae}$ is the external Alfvén velocity $= B^2/(4\pi m_p N_{e\rm ext})$), characterised by an increase in amplitude and an accompanying gradual increase in frequency; 2) a quasi-periodic phase, at a time $\propto \frac{1}{v_{\rm A}}$, showing a marked increase in amplitude; and 3) a periodic decay phase with a rapid decrease in amplitude. This result is mirrored in the models of Berghmans *et al.* (1996), who analyse the progression of an impulsively driven wave along a loop.

Since the wave we observe is characterised by a travelling wavefront and a trailing wake (of negative amplitude), it is of interest to compare the findings of Roberts *et al.* (1984) with our observations. The onset of the detected 6-s periodicity occurs at a time $\sim$20 s after the beginning of eclipse ($t = 0$). Given the time series of our observations, this presents us with two possible interpretations. It may be the case that the wave is observed in its periodic phase, with the information being carried along the loop at $v_{\rm Ae}$. In this instance, the onset of a detectable oscillatory component may be due to the gradual increase in amplitude to the level where it is detected above the noise. The corresponding increase in frequency, due to the arrival of progressively faster frequency

information, arises because of the dispersion relation of the fast-mode wave. Wavelet transforms enjoy only limited frequency resolution, however, and a small increase in frequency may have gone undetected in our data.

Alternatively, the emergence of signal from below the noise level may be due to the onset of the quasi-periodic phase with its associated leap in amplitude. The difficulty in assigning the observed periodicity to either of these scenarios lies in both the limited signal-to-noise of the available SECIS data, and the length of the time series, since the observed periodicity continues until – and perhaps beyond – the end of the time series. Furthermore, both the periodic and quasi-periodic phases of the impulsively generated wave are partially characterised by an increase in amplitude. The power in the 0.16-Hz band (Figures 5.22 to 5.24) is observed to increase over the duration of the time series, but it is unclear as to whether this is entirely a monotonic increase (periodic phase) or part of a rise-and-fall (quasi-periodic phase). If we are truly observing the periodic phase of the wave, then the observed group velocity is likely to be closer to $v_{\rm Ae}$ than $v_{\rm A}$. In this case, the local magnetic field is more likely to be ~ 25 G, again a reasonable value for the coronal field.

As a final point of interest in this comparison, Berghmans *et al.* (1996) also find that contributions from behind the initial wavefront can leak to the loop's more tenuous exterior, and overtake the leading wavefront due to the higher external Alfvén velocity, $v_{\rm Ae}$, returning to the loop to contribute a negative-amplitude (dark) disturbance ahead of the wave within the loop. If we examine more closely the intensity of the wave in Figure 6.2, we see that there indeed appears to be such a darkening ahead of the leading bright edge in the fast-mode wave.

The apparent failure of this wave to match the criteria necessary for damping along, and thereby depositing energy in, the loop which we have examined here may provide further evidence for the recent conclusions by Aschwanden (2001). In this review, he expounds the inability of many wave mechanism models to predict the isothermality, substantial overdensity and upflows of (chromospheric) material observed in coro-

nal loops with the *TRACE*, *Yohkoh* and *SoHO* missions. Uniform heating indicates preferentially high temperatures at the loop apex, and no viable magnetic compression mechanism can account for the observed overdensity in loops, with respect to their environments, often of greater than a degree of magnitude. Rather, it seems that the models which most accurately explain the observations are those based on heating of chromospheric material near the loop footpoints. The observations we present here, however, do add to the wealth of data which evidences the existence of wave phenomena in the corona. It is simply that our observations do not show a wave 'caught in the act' of heating.

6.6 Conclusions

The most likely explanation for the wave observed during the 1999 August 11 total solar eclipse is that it is a fast-mode magnetoacoustic wave which has been triggered by an impulse, such as a reconnection of magnetic threads within a coronal loop. This loop is characterised by an enhancement of density ($\rho_0/\rho_{\rm ext} \approx 2.5$) in the local magnetic field of $\sim$ 25–40 G. It is not really possible to say whether the wave conforms to the periodic or quasi-periodic phases of an impulsively generated fast-mode wave, because of low signal-to-noise in the Fe XIV channel with which we observed the wave. This is further compounded by the fact that the associated oscillation is only detected in the second half of our time series, which is limited to the first 40 s of the 1999 total solar eclipse. The wave does appear to fit aspects of the model of Berghmans *et al.* (1996) with respect to impulsively generated fast-mode waves, in particular the appearance of a darkening before the wave's leading maximum. Although the wave's energy density is one order of magnitude higher than the radiative losses and the distance travelled is greater than $\lambda/(4\pi)$, the damping length is well in excess of the value required for effective dissipation. We therefore conclude that the wave does not dissipate any significant energy in the loop.

Chapter 7

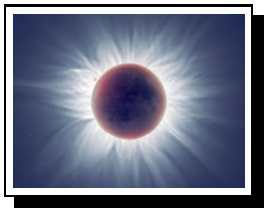

Concluding Remarks & Future Work

7.1 Thesis summary

This thesis has presented results from the analysis of both dynamic events (oscillations and flares) and quiescent atmospheres. The findings are summarised below in order of appearance.

7.1.1 Opacity in late-type stellar atmospheres

The Si IV and C IV opacity-sensitive resonance line ratios are examined in *HST*/GHRS and data of Capella and YZ CMi. In optically thin conditions, the intensity ratio of the two multiplets is expected to be 2:1. Significant deviations from this ratio from the optically thin value are identified. In two cases, these deviations coincide with flares. The observed line ratios to derive escape probabilities and optical depths. The optical depths combined with independent measurements of the electron density are used to calculate path lengths. In the case of the RS CVn binary Capella, we estimate path lengths of approximately 75 km.

7.1.2 Multi-wavelength solar flare observations

We report on observations of a large eruptive event associated with a flare that occurred on 1998 September 27, made with the Richard B. Dunn Solar Telescope (DST) at Sacramento Peak Observatory (several passbands including Hα red wings), in soft and hard X–rays (*GOES* and BATSE), and in several ultraviolet passbands (including Fe IX/X λ171 Å, Fe XII λ195 Å, and C IV λ1550 Å) of the *Transition Region and Coronal Explorer* (*TRACE*). The flare initiation is signalled by a hard X-ray burst and a gradual increase in emission in other wavelengths. The flux then passes through two peaks before attaining a main peak, after which there is a monotonic decline. The emission returns to pre-flare levels after about 35 minutes, by which time a set of bright post-

flare loops begin to form. Part of the Hα emission intrudes into the penumbra of a large sunspot, generally a characteristic of very powerful flares, but the flare importance in *GOES* soft X-rays is in fact relatively modest (C5.2). Much of the energy appears to be in the form of mass motions which are observed in optical and ultraviolet bands, travelling out via several magnetic flux tubes from the main flare site (about 60° from Sun centre) to beyond the limb.

7.1.3 The Solar Eclipse Corona Imaging System

The Solar Eclipse Corona Imaging System (SECIS) was used to record high-cadence observations of the solar corona during the total solar eclipse of 11th August 1999. During the 2 min 23.5 s of totality, 6364 images were recorded simultaneously in each of two channels: a white light channel, and the Fe XIV λ5303 Å 'green line' channel (T $\sim$ 2MK). This work reports the latest results from the SECIS experiment, including the discovery of a 6-second intensity oscillation in an active region coronal loop.

In a follow-up chapter, we show that this oscillation is associated with a fast mode wave that travels through the loop apex with a velocity of $\sim$2000 km s^{-1}. We use near-simultaneous *SoHO* observations to calculate the parameters of the loop and its surroundings such as density, temperature and their spatial variation. Radiative losses of the loop are calculated in the temperature range $10^{5.8}$ – $10^{6.4}$ K, and compared with the wave energy density. The flux carried by the wave is found to exceed the radiative losses by an order of magnitude. However, although the wave travels a distance greater than $\lambda/4\pi$ and therefore meets a necessary criterion for the small damping approximation, the dissipation length is, in fact, well in excess of the loop length. The temporal evolution of the intensity is in agreement with the model of an impulsively generated, fast-mode wave.

7.2 Future directions

7.2.1 Opacity

Opacity has been shown in this thesis to be a potentially powerful diagnostic in examining the geometry of unresolved stellar sources. It also has an important consequence in terms of emission measure distributions. If the flux of an emission line is reduced by opacity, it will have a derogatory effect on any emission measure distribution in which it is included. Given a suitable optically-sensitive line ratio for the emitting ion, however, one can remove the attenuation in this line and so correctly model the EM distribution. Using *Chandra* spectra, Phillips *et al.* (2001) have shown that this effect is not seen in the Fe XVII λ15.01 Å line in the corona of Capella, even though it is present in the transition region.

An additional effect of opacity is to broaden the profile of emission lines. Accurate estimates of the opacity will allow the removal of this broadening from observed lines, and lead to much more accurate estimates of non-thermal broadening, such as microturbulence.

A further possibility for the extension of this work lies in the recently available data from the *Far Ultraviolet Spectroscopic Explorer* (*FUSE*) satellite mission. The line ratios presented in this thesis are for fluxes integrated across the whole line profiled. The resolution of *FUSE*, though, is higher than that of GHRS, and with further observations, one may be able to ascertain whether the line ratio varies substantially across the line profiles. This may reveal further information about the dynamics of different parts of the transition region and corona.

7.2.2 *Flare observations*

The multi-wavelength flare observations presented in this thesis show a somewhat unusual flare which, although not particularly luminous, appears to release large amounts of kinetic energy in the form of a spray event. The relatively high cadence of these observations will, in the very near future, be superseded by that of the nascent *HESSI* mission in hard X-ray imaging. There also exists the possibility for complementary ground-based observations using the high-cadence, dual-channel SECIS system to show the evolution of mass motions, using Doppler-shift images sequences, or fast imaging of polarisations of the Fe I λ6302.4 Å line.

7.2.3 *The* SECIS *project*

As the bulk of the presented work focuses on the SECIS instrument and its applications, it is worth dwelling on the future of this instrument.

Pasachoff (2002) also report on the 1999 eclipse, using a similar, lower-cadence system, but find no evidence of distinct intensity oscillations in the neighbouring active region NOAA AR 8651. Since their observations achieve higher spatial resolution, this may well highlight the transient nature of MHD coronal oscillations, and emphasises the need for complementary Fourier and wavelet analysis of coronal lightcurves. Additionally, the parallel analysis of *SoHO* data in Chapter 6 points the way to much more detailed studies of the dynamics of such waves in coronal active regions, particularly when used in tandem with eclipse or even coronagraph observations. A particular target in the continuation of this project would be catching a magnetoacoustic wave 'red-handed' – finding that the periodicity and damping length were short enough to compensate for the radiative and conductive losses from the loop, and seeing the wave dissipate accordingly.

Gallagher (1999) presented the history of the project until the 1999 total solar

eclipse, observations of which are already analysed here. However, eclipse event data show that no accessible totality events of sufficient duration will occur until March 2006. The short-term future of the instrument is therefore most likely in ground-based observations, for which preparations are underway. In the meantime, data from the June 2001 total eclipse in Zambia are now becoming available. The main advantages in the 2001 data lie in their improved stability and signal-to-noise.

It should not be forgotten that SECIS was also conceived of as a search tool for nanoflares and microflares, not simply oscillations. The high cadence of the instrument may also be applied to quiet Sun observations, preferably with the assistance of adaptive optics to eliminate seeing variations as much as is possible. As pointed out in the recent literature, higher-cadence observations may help to remove the apparent deficit between the predicted numbers of very low energy reconnection events on the Sun and those actually observed.

Finally, the long-term extension of the project seems a logical extension of the original SECIS goal, viz. the elimination of the effects of the sky in the search for short-timescale variations in coronal emission. There exists the possibility of a space-based descendant of SECIS, which would image the corona without the atmospheric effects of sky brightness, narrow-band visibility and turbulent distortion. Such a satellite mission would be well-placed to observe in allowed (and therefore much brighter) coronal and transition region emission lines, and would remove the crippling limit of only a few minutes' observing time every few years. If high-frequency oscillations are indeed transient events, as this work would seem to suggest, then regular space-based observations appear to be the logical conclusion to SECIS.

References

Antiochos, S.K., 1988, *ApJ*, 502, L181

Arnaud, M., Raymond, J., 1992, *ApJ*, 398, 394

Arnaud, M., Rothenflug, R., 1985, *A&AS*, 60, 425

Aschwanden, M.J., Hudson, H., Kosugi, T., Schwartz, R.A., 1996a, *ApJ*, 464, 985

Aschwanden, M.J., Wills, M.J., Hudson, H., Kosugi, T., Schwartz, R.A., 1996b, *ApJ*, 468, 398

Aschwanden, M.J., Fletcher, L., Schrijver, C.J., Alexander, D., 1999a, *ApJ*, 520, 880

Aschwanden, M.J., Newmark, J.S., Delaboudinière, J.-P., Neupert, W., Klimchuk, J.A., Gary, G.A., Portier-Fozzani, F., Zucker, A., 1999b, *ApJ*, 525, 842

Aschwanden, M.J., 2001, *ApJ*, 560, 1035

Athay, R., 1972, *Radiation Transport in Spectral Lines*, D. Reidel Publishing Company, Dordrecht

Avrett, E.H., Loeser, R., 1992, in *Proc. Seventh Cambridge Workshop, 'Cool Stars, Stellar Systems and the Sun'*, ASP Conf. Ser., 26, 489

Banerjee, D., O'Shea, E., Doyle, J.G., 2000, *A&A*, 355, 1152

Bentley, R.D., 2001, *the TRACE Analysis Guide (TAG)*, Mullard Space Science Laboratory, available at `http://surfwww.mssl.ucl.ac.uk/guides/tag/`

Benz, A.O., 1993, *Plasma Astrophysics*, Kluwer Academic Publishers, Dordrecht

Beghmans, D., De Bruyne P., Goossens, M., 1996, *ApJ*, 472, 398

Bonnacini, D., Cavallini, F., Cepatelli, G., Righini, A., 1989, *A&A*, 217, 368

Brueckner, G.E., Bartoe, J.-D.F.,, 1983, *ApJ*, 272, 329

Brosius, J.W., Davila, J.M., Thomas, R.J., 1998, it ApJ Letters, 497, 113

Brosius, J.W., Davila, J.M., Thomas, R.J., Thompson W.T., 1994, *ApJ*, 425, 343

Canfield, R.C, Reardon, K.P., Leka, K.D., Shibata, K., Yokoyama, T., Shimojo, M., 1996, *ApJ*, 464, 1016

Chiueh, T., 2000, *ApJ*, 539, 933

Conway, A., 2001, private communication

Delaboudinière, J.-P., Artzner, G.E., Brunaud J., Gabriel, A.H., Hochedez, J.F., Millier, F., Song, X.Y., Au, B., Dere, K.P., Howard, R.A., Kreplin, R., Michels, D.J., Moses, J.D., Defise, J.M., Jamar, C., Rochus, P., Chauvineau, J.P., Marioge, J.P., Catura, R.C., Lemen, J.R., Shing, L., Stern, R.A., Gurman, J.B., Neupert, W.M., Maucherat, A., Clette, F., Cugnon, P., van Dessel, E.L., 1995, *Solar Physics*, 162, 291

De Moortel, I., Ireland, J., Walsh, R.W., 2000, *A&A*, 255, L23

Dere, K.P., Landi, E., Mason, H.E., Monsignori-Fossi, B.C., Young, P.R., 1997, *A&AS*, 125, 149

Dere, K.D., Mason, H.E., 1993, *Solar Physics*, 144, 217

Dermendzhiev, V.N., Kolarov, G.V, Mitsev, Ts.A., 1992, *Solar Physics*, 137, 199

Doyle, J.G, M^{c}Whirter, R.W.P., 1980, *Mon. Not. R. Ast. Soc.*, 193, 947

Edlén, B., 1942, *Zeit. Astrophys.*, 22, 47

Feldman, U., 1992, *Physica Scripta*, 46, 202

Fleck, B., Domingo, V., Poland A.I., 1995, *The SoHO Mission*, Kluwer Academic Publishers, Dordrecht

Fletcher, L., de Pontieu, B., 1999, *ApJ Letters*, 520 135

Freeland, S.L., Handy, B.N., 1998, *Solar Physics*, 182, 497

Gaizauskas, V., Mandrini, C.H., Démoulin, P., Luoni, M.L., Rovira, M.G., 1998, *A&A*, 332, 353

Gallagher, P.T., 1999, *Optical and Ultraviolet Observations of the Solar Atmosphere*, Ph.D. Thesis, Queen's University of Belfast

Gallagher, P.T., Phillips, K.J.H., Harra-Murnion, L.K., Baudin, F., Keenan, F.P., 1999, *A&A*, 348, 251

Gallagher, P.T., Williams, D.R., Phillips, K.J.H., Mathioudakis, M., Smartt, R.N., Keenan, F.P.,, 2000, *Solar Physics*, 367, 380

Habbal S.R., Leer E., Holzer T.E., 1979, *Solar Physics*, 64, 287

Hale, G.E., Ellerman, F., Nicholson, S.B., Joy, A.H., 1919, *ApJ*, 49, 153

Handy, B.N., Acton, L.W., Kankelborg, C.C., Wolfson, C.J., Akin, D.J., Bruner, M.E., Caravalho, R., Catura, R.C., Chevalier, R., Duncan, D.W., Edwards, C.G., Feinstein, C.N., Freeland, S.L., Friedlaender, F.M., Hoffmann, C.H., Hurlburt, N.E., Jurcevich, B.K., Katz, N.L., Kelly, G.A., Lemen, J.R., Levay, M., Lindgren,

R.W., Mathur, D.P., Meyer, S.B., Morrison, S.J., Morrison, M.D., Nightingale, R.W., Pope, T.P., Rehse, R.A., Schrijver, C.J., Shine, R.A., Shing, L., Strong, K.T., Tarbell, T.D., Title, A.M., Torgerson, D.D., Golub, L., Bookbinder, J.A., Caldwell, D., Cheimets, P.N., Davis, W.N., Deluca, E.E., McMullen, R.A., Warren, H.P., Amato, D., Fisher, R., Maldonado, H., Parkinson, C., 1999, *Solar Physics*, 187, 229

Handy, B.N., Schrijver, C.J., 2000 *ApJ*, 547, 1100

Harrison, R.A., Rompolt, B., Garczynska, I., 1988, *Solar Physics*, 116, 61

Harrison, R.A., Sawyer, E.C., Carter, M.K., Cruise, A.M., Cutler, R.M., Fludra, A., Hayes, R.W., Kent, B.J., Lang, J., Parker, D.J., Payne, J., Pike, C.D., Peskett, S.C., Richards, A.G., Culhane, J.L., Norman, K., Breeveld, A.A., Breeveld, E.R., Al Janabi, K.F., McCalden, A.J., Parkinson, J.H., Self, D.G., Thomas, P.D., Poland, A.I., Thomas, R.J., Thompson, W.T., Kjeldseth-Moe, O., Brekke, P., Karud, J., Maltby, P., Aschenbach, B., Brauninger, H., Kuhne, M., Hollandt, J., Siegmund, O.H.W., Huber, M.C.E., Gabriel, A.H., Mason, H.E., Bromage, B.J.I., 1995, *Solar Physics*, 162, 233

Harrison, R.A., Bryans, P., Bingham, R., 2001, *A&A*, 379, 324

Hasan, S.S, Kalkofen, W., 1999, *ApJ*, 519, 899

Hirayama, T., 1974, *Solar Physics*, 34, 323

Hollweg, J.V., 1981, *Solar Physics*, 70, 25

Hood, A., Anzer. U., 1987, *Solar Physics*, 111, 333

Houdebine, E.R., Doyle, J.G., 1994, *A&A*, 289, 169

Ireland, J., Walsh, R.W., Harrison, R.A., Priest, E.R., 1999, *A&A*, 347, 355

Jordan, C., 1967, *Solar Physics*, 2, 441

Jordan, C., 1977, in *Progress in Atomic Spectroscopy*, Hanle, W. & Kleinpoppen, H. eds., Plenum Press, New York

Kane, S.R., Kai, K., Kosugi, T., Enome, S., Landecker, P.B., McKenzie, D.L., 1983, *ApJ*, 271, 376

Kastner, S.O., Kastner, R.E., 1990, *J. Quant. Spectrosc. Radiat. Transfer*, 44, 275

Keenan, F.P., Kingston, A.E., 1986, *Mon. Not. R. Ast. Soc.*, 220, 493

Keenan, F.P., Thomas R.J., Neupert, W.M., Conlon, E.S., Burke V.M., 1993 *Solar Physics*, 144, 69

Kleeorin, N., Rogachevskii, I., Ruzmaikin, A., 1995, *A&A*, 297, 159

Kopp, R.A., Poletto, G., 1984, *Solar Physics*, 93, 351

Koutchmy, S., Žugžda, Y.D., Locăns, V., 1983, *A&A*, 120, 185

Laing G.B., Edwin P.M., 1995a, *Solar Physics*, 157, 103

Laing G.B., Edwin P.M., 1995b, *Solar Physics*, 161, 269

Lin H., Penn, M.J., Tomczyk, S., 2000, *ApJ Letters*, 541, 83

Lin, H., Rimmele, T., 1999, *ApJ*, 514, 448

Linsky, J.L., Wood, B.E., Judge, P., Brown, A., Andrulis, C., Ayres, T.R., 1995, *ApJ*, 442, 381

Linsky, J.L., Wood, B.E., Brown, A., Osten, R., 1998, *ApJ*, 492, 767

M^{c}Ateer, R.T.J., Gallagher, P.T., Williams, D.R, Mathioudakis, M., Phillips, K.J.H., Keenan, F.P., 2002, *ApJ Letters*, *in press*

M^{c}Kenzie D., Mullan D., 1997, *Solar Physics*, 176, 127

Mallat, S., 1998, *A Wavelet Tour of Signal Processing*, Academic Press, San Diego

Maniak, S.T., Träbert, E., Curtis, L.J., 1993, *Physics Letter A*, 173, 407

Mariska, J.T., 1992, *The Solar Transition Region*, Cambridge University Press, Cambridge

Mathioudakis, M., Fruscione, A., Drake, J.J., M^{c}Donald, K., Bowyer, S., Malina, R.F., 1995, *A&A*, 300, 775

Mazzotta, P., Mazzitelli, G., Colafrancesco, S., Vittorio, N., 1998, *A&AS*, 133, 403

Moehs, D.P., Church, D.A., 1999, *ApJ Letters*, 516, 111

Mohan, M., Hibbert, A., Kingston, A.E., 1994, *ApJ*, 434, 389

Moore, R.L., Schmieder, B., Hathaway, D.H., Tarbell, T.D., 1997, *Solar Physics*, 176, 153

Munro, R.H., Gosling, J.T., Hildner, E., MacQueen, R.M., Poland, A.I., Ross, C.L., 1979, *Solar Physics*, 61, 201

Nakariakov, V.M., Ofman, L., DeLuca, E.E., Roberts, B., Davila, J.M., 1999, *Science*, 285, 862

Ohyama, M., Shibata, K., 1997, *Publ. Astron. Soc. Japan*, 49, 249

Parker, E.M., 1970, *ApJ*, 162, 665

Parker, E.N., 1975, *ApJ*, 198, 205

Parker, E.N., 1988, *ApJ*, 330, 474

Pasachoff, J.M., Landman, D.A., 1984, *Solar Physics*, 90, 325

Pasachoff, J.M., Ladd, E.F., 1987, *Solar Physics*, 109, 365

Pasachoff, J.M., Babcock, B.A., Russell, K.D., Seaton, D.B., 2002, *Solar Physics*,

in press

Peter, H., 2001, *A&A*, 374, 1108

Phillips, K.J.H., Greer, C.J., Bhatia, A.K., Keenan, F.P., 1996, *ApJ Letters*, 469, L57

Phillips, K.J.H., 2000, *Plasma Phys. Control. Fusion*, 42, 113

Phillips, K.J.H., Read, P., Gallagher, P.T., Keenan, F.P., Rudawy, P., Rompolt, B., Berlicki, A., Buczyłko, A., Diego, F., Barnsley, R., Smartt, R.N., Pasachoff, J.M., Babcock, B.A., 2000, *Solar Physics*, 193, 259.

Phillips, K.J.H., Mathioudakis, M., Huenemoerder, D.P., Williams, D.R., Phillips, M.E., Keenan, F.P., 2001, *Mon. Not. R. Ast. Soc.*, 325, 1500

Phillips, K.J.H., 2002, *private communication*

Pneuman, G.W., 1981, in *Solar Flare Magnetohydrodynamics*, E. Priest, ed., Gordon & Breach, New York

Porter, L.J., Klimchuk, J.A., Sturrock, P.A., 1994a, *ApJ*, 435, 482

Porter, L.J., Klimchuk, J.A., Sturrock, P.A., 1994b, *ApJ*, 435, 502

Porter, J.G., Fontenla, J.M., Simnett, G.M., 1995, *ApJ*, 438, 472

Priest, E.R., 1982, *Solar Magnetohydrodynamics*, D. Reidel, Dordrecht

Priest, E.R., Forbes, T.G., 1990, *Solar Physics*, 126, 319

Priest, E.R., 1991, *Phil. Trans. R. Soc. Lond. A*, 336, 363

Priest, E.R., Schrijver, C.J., 1999, *Solar Physics*, 190, 1

Raymond, J.C., Doyle, J.G., 1981, *ApJ*, 247, 686

Roberts, B., 2000, *Solar Physics*, 193, 139

Robinson, R.D., Carpenter, K.G., Percival, J. W., 1999, *ApJ*, 516, 916

Rosner, R., Tucker, W.H., Vaiana, G.S., 1978, *ApJ*, 220, 643

Rudawy, P., Rompolt, B., Berlicki, A., Buckyłko, L., Phillips, K.J.H., Gallagher, P.T., Williams, D.R., Keenan, F.P., 2001, in Mishev & Phillips, ed., *Proc. International Conf. 'First Results of the 1999 Total Eclipse Observations', Varna, Bulgaria, Sept. 2000* (to be published).

Russell, K.D., 2000, *A Search for High-Frequency Coronal Oscillations at the 1999 Total Solar Eclipse*, B.A. Thesis, Williams College, Massachusetts

Saba, J.L.R., Schmelz, J.T., Bhatia, A.K., Strong, K.T., 1999, *ApJ*, 510, 1064

Schmelz, J.T., Saba, J.L.R., Chauvin, J.C., Strong, K.T., 1997, *ApJ*, 477, 509

Schmieder, B., Shibata, K., van Driel-Gesztelyi, L., Freeland, S., 1995, *Solar Physics*, 156, 245

Schmitt, J.H.M.M., Drake, J.J., Stern, R.A., 1996, *ApJ Letters*, 465, L51

Schrijver, C.J., van den Oord, G.H.J., Mewe, R., 1994, *A&A Letters*, 289, L23

Schrijver, C.J., Mewe, R., van den Oord, G.H.J., Kaastra, J.S., 1995, *A&A*, 302, 438

Schrijver, C.J., van den Oord, G.H.J., Mewe, R., Kaastra, J.S., 1996, in Bowyer, S. & Malina R.F., eds., *Astrophysics in the Extreme Ultraviolet*, Kluwer Academic Publishers, Dordrecht

Schrijver, C.J., Title, A.M., van Ballegooijen, A.A., Hagenaar, H.J., Shine, R.A., 1997, *ApJ*, 487, 424

Schrijver, C.J., Title, A.M., Berger, T.E., Fletcher, L., Hurlburt, N.E., Nightingale, R.W., Shine, R.A., Tarbell, T.D., Wolfson, J., Golub, L., Bookbinder, J.A., Deluca, E.E., McMullen, R.A., Warren, H.P., Kankelborg, C.C., Handy, B.N., de Pontieu, B., 1999, *Solar Physics*, 187, 261

Simon, T., Landsman, W.B., 1997, *ApJ*, 483, 435

Smith, J.M., Roberts, B., Oliver, R., 1997, *A&A*, 327, 377

Spruit, H.C, Roberts, B., 1983, *Nature*, 304, 401

Stein, R.F., Leibacher, J., 1974, *Ann. Rev. Astron. & Astroph.*, 12, 407

Stenborg, G.A., 2000, *Interpretation and Analysis on Various Time Scales of Narrow-Band Coronal Observations Obtained with a New Coronagraph System*, Ph.D. Thesis, Georg-August-Universität Göttingen

Sylwester, B., Faucher, P., Jakiemic, J., Krutov, V.V., M^{c}Whirter, R.W.P., Sylwester, J., Tomczak, M., Volonté, S., Zhitnik, I.A., 1986, *Solar Physics*, 103, 67

Švestka, Z., 1981, in *Solar Flare Magnetohydrodynamics*, E. Priest, ed., Gordon & Breach, New York

Švestka, Z., Uchida, Y., 1991, *The Yohkoh (Solar-A) Mission*, Kluwer Academic Publishers, Dordrecht

Švestka, Z., Cliver, E.W., 1992, in Švestka, Z., Jackson, V. & Machodo, M.E., eds., *Eruptive Solar Flares*, Springer-Verlag, Berlin

Tandberg-Hanssen, E., Martin, S.F., Hansen, R.T., 1980, *Solar Physics*, 65, 357

Temmer, M., Veronig, A., Hanslmeier, A., Otruba, W., Messerotti, M., 2001, *A&A*, 375, 1049

Torrence, C., Compo, G.P., 1998, *Bull. Amer. Meteor. Soc.*, 79, 61

Ulmschneider, P., Zähringer, K., Musielak, Z.E., 1991, *A&A*, 241, 625

van den Oord, G.H.J., Doyle, J.G., Rodono, M., Gary, D.E., Henry, G.W., Byrne, P.B., Linsky, J.L., Haisch, B.M., Pagano, I., Leto, G., 1996, *A&A*, 310, 908

Valníček, B., 1964, Bull. Astron. Inst. Czech., 15, 207

Vernazza, J.E., Avrett, E.H., Loeser, R., 1981, *ApJS*, 45, 635

Vršnak, B., 1990, *Solar Physics*, 129, 295

Wang, Y.-M., 2000, *ApJ Letters*, 543, 89

Wiese, W.L., Smith, M.W., Glennon, B.M., 1966, in *Atomic Transition Probabilities*, National Standard Reference Data Series

Wilson O.C., 1966, *ApJ*, 144, 695

Wood, B.E., Karovska, M., 1998, *ApJ*, 503, 432

Zaĭtsev, V.V., Stepanov, A.V., 1989, *SvAL*, 15, 66

Zhang, J., White, S.M., Kundu, M.R., 1999, *ApJ*, 527, 977